



**HAL**  
open science

## Silicon based terahertz radiation detectors

Dmytro But

► **To cite this version:**

Dmytro But. Silicon based terahertz radiation detectors. Physics [physics]. Université Montpellier II - Sciences et Techniques du Languedoc, 2014. English. NNT : 2014MON20170 . tel-01811025

**HAL Id: tel-01811025**

**<https://theses.hal.science/tel-01811025>**

Submitted on 8 Jun 2018

**HAL** is a multi-disciplinary open access archive for the deposit and dissemination of scientific research documents, whether they are published or not. The documents may come from teaching and research institutions in France or abroad, or from public or private research centers.

L'archive ouverte pluridisciplinaire **HAL**, est destinée au dépôt et à la diffusion de documents scientifiques de niveau recherche, publiés ou non, émanant des établissements d'enseignement et de recherche français ou étrangers, des laboratoires publics ou privés.

# THÈSE

Pour obtenir le grade de  
**Docteur**

Délivré par l'**Université Montpellier II**

Préparée au sein de l'école doctorale I2S\*  
Et de l'unité de recherche Laboratoire Charles Coulomb  
UMR 5221 CNRS-UM2

Spécialité : **Physique**

Présentée par **Dmytro B. BUT**

## Détecteurs de radiation THz à base de silicium

Soutenue le 24 septembre 2014 devant le jury composé de

Prof. Wojciech Knap, L2C Université Montpellier 2, France  
Dr. Jean-François Lampin IEMN Lille, France  
Dr. Jerzy Łusakowski, University of Warsaw, Poland  
Prof. Luca Varani, IES Université Montpellier 2, France

Directeur de thèse  
Rapporteur  
Rapporteur  
Président du jury

Academy of Montpellier

---

UNIVERSITY OF MONTPELLIER 2  
SCIENCES AND TECHNOLOGY OF LANGUEDOC

PhD Thesis

in partial fulfillment to obtain the degree of

DOCTOR OF PHYSICS

DOCTORAL COURSE: Semiconductor Physic

DOCTORAL SCHOOL: Information, Structures and Systems

SILICON BASED TERAHERTZ RADIATION DETECTORS

Prepared by

**Dmytro B. BUT**

under the direction of:

Prof. Wojciech KNAP and Dr. Nina DYAKONOVA

To be defended on September 24, 2014 in front of the following examination panel:

Dr. Jerzy ŁUSAKOWSKI	University of Warsaw, POLAND	Referee
Dr. Jean-François LAMPIN	IEMN Lille, FRANCE	Referee
Prof. Luca VARANI	IES Université Montpellier 2, FRANCE	Examiner
Prof. Wojciech KNAP	L2C Université Montpellier 2, FRANCE	Supervisor

Charles Coulomb Laboratory – UMR 5221 CNRS-University of  
Montpellier 2

---

MONTPELLIER – 2014

## ABSTRACT

This thesis is devoted to study of terahertz detectors based on field-effect transistors fabricated using silicon technology and their comparison to InGaAs/InP ones. The main research effort was devoted to the problem of detectors linearity at high radiation intensities. The photoresponse of field effect transistors to terahertz radiation in a wide range of intensities: from  $0.5 \text{ mW/cm}^2$  up to  $500 \text{ kW/cm}^2$  and for frequencies from  $0.13 \text{ THz}$  to  $3.3 \text{ THz}$  was studied. This work shows that the photoresponse of all studied detectors increases linearly with increasing radiation intensity up to a few  $\text{kW/cm}^2$  range and is followed by the nonlinear and saturation parts for higher radiation intensities. This effect has led to the new model of broadband field-effect transistor detectors. The model is based on the phenomenological knowledge of the transistor static transfer characteristic and explains the photoresponse nonlinearity as related to non-linearity and saturation of the transistor channel current. The developed model explains consistently experimental data both in linear and nonlinear regions of terahertz detection.

---

## RÉSUMÉ

Cette thèse est consacrée à l'étude des détecteurs de radiation THz basés sur des transistors à effet de champ qui ont été fabriqués en utilisant les technologies différentes. La photoréponse de transistors à effet de champ a été étudiée dans une large gamme d'intensités de radiation: de  $0,5 \text{ mW/cm}^2$  à  $500 \text{ kW/cm}^2$ , et pour des fréquences allant de  $0,13 \text{ THz}$  à  $3,3 \text{ THz}$ . Les détecteurs montrent la photoréponse linéaire en fonction de l'intensité du rayonnement dans une large gamme d'intensités, jusqu'à plusieurs  $\text{kW/cm}^2$ . Pour toutes les fréquences nous avons observé que la région linéaire a été suivie par une partie non linéaire et ensuite par une saturation. Cet effet a conduit à un nouveau modèle de détecteurs FET à large bande qui est basé sur la connaissance phénoménologique de caractéristiques statiques de transistor. Le modèle prend en compte le comportement non linéaire du courant dans le canal dans toute une plage de fonctionnement du transistor, ce qui est particulièrement important à des intensités élevées de rayonnement THz. Les données expérimentales ont été interprétées avec succès dans le cadre du modèle développé.

## ACKNOWLEDGEMENT

*At first, I would like to thank my supervisor Prof. Wojciech Knap, for giving me the opportunity to work in his group. He helped me understand the experimental results. Moreover, I would like to thank him for his patience and detailed explanations of any kind of question I had during the last three years. I would also like to thank my co-supervisor Dr. Nina Dyakonova for her help in understanding the experimental results. She helped me improve my presentation skills and helped me while I was writing my thesis. I would also like to thank Prof. Sergey D. Ganichev and Dr. Christophe Drexler for his help in the TerZ lab. They patiently helped me with the THz high-power experiments. He also participated in the experiments. I would also like to thank Dr. Frédéric Teppe, Dr. Dominique Coquillat, Dr. A. El Fatimy and Prof. Michel I. Dyakonov. They were always there to discuss some scientific problems or any personal problems. I would also like to thank Dr. Chiko Otani, who was responsible for WITH project in Senday, and Dr. Hiroaki Minamide and Prof. Taiichi Otsuji for his help during my work in RIKEN lab.*

*I would like to thank our collaborators Prof. Fedir F. Sizov, Dr. Oleksander G. Golenkov and Dr. Mykola Sakhno. Oleksander participated in some of the experiments. Mykola provided theoretical explanations for some of the experimental results. Whenever I had any questions, Prof. Sizov promptly provided me with the explanations. I would like to thank Dr. Alexey Gutin and Dr. Volodimer P. Reva, for providing the samples for this work. Moreover, Alexey participated in some of the experiments. I am thankful to Mr. Pierre Solignac and Mr. P. Buzatu for help with constructing of the experimental stuff for my experimental work. Mr. Jean-Marie Peiris for bonding of samples for measurements and Mr. Dr. Christophe Consejo for his help whenever we needed to do something in the workshop.*

*I acknowledge the financial support provided by the GDR&GDRI THz, the COST Tera-MIR and "WITH" projects for this work. They also provided me with the opportunity to participate and present my work in many international schools and conferences.*

*Finally, I would like to thank my parents, my brother, and my friends, for their support and encouragement.*

*Dmytro But*

# CONTENTS

<b>Acronyms and Glossary</b> .....	iii
<b>Symbols</b> .....	iv
<b>List of Tables</b> .....	vi
<b>List of Figures</b> .....	vii
<b>Chapter 1 Introduction and theory</b> .....	1
1.1 Terahertz Band .....	1
1.2 Terahertz detectors .....	2
1.3 Field Effect Transistors for Terahertz Detection .....	6
1.4 Hydrodynamic theory of terahertz field-effect-transistor detection .....	7
1.5 Summary .....	13
<b>Chapter 2 Samples, experimental setup and experimental techniques</b> .....	14
2.1 Samples .....	14
2.1 Silicon metal-oxide-semiconductor field-effect transistors .....	14
2.1.2 High electron mobility transistors .....	14
2.2 Antenna effect of metallic interconnections .....	18
2.3 Terahertz detection asymmetry .....	24
2.4 Antennas for detectors based on CMOS 0.35 $\mu\text{m}$ process .....	27
2.4.1 Simulation of antenna structure .....	28
2.4.2 Experimental results .....	31
2.5. Measurement of electrical characteristics of transistors at different temperatures and magnetic field .....	33
2.6. Sources of Terahertz Radiation .....	35
2.6.1 Continuous-Wave Monochromatic Terahertz Radiation Sources .....	35
2.6.2 Pulsed Terahertz Sources .....	36
2.7 Optical Components of the Experimental Setup .....	38
<b>Chapter 3 Models of field effect transistor terahertz detection at high     intensities</b> .....	41
3.1 The Phenomenological Compact Model of Field Effect Transistor .....	41
3.2 Broadband Terahertz Detection Model by Lifshits-Sakowicz .....	44

3.3 The Extended Broadband Terahertz Detection Model .....	47
3.4 Models Comparison .....	51
3.5 Summary.....	54
<b>Chapter 4 Nonlinear photoresponse of field effect transistors terahertz detectors at high irradiation intensities .....</b>	<b>55</b>
4.1 Dynamic range of Terahertz Field-Effect Transistor .....	55
4.2 Frequency dependence of the detector sensitivity.....	61
4.3 Summary.....	63
<b>Conclusion and future work.....</b>	<b>64</b>
<b>Appendix A Temperature dependence of terahertz photoresponse.....</b>	<b>65</b>
A.1 Low Temperature Measurements .....	65
A.2 Temperature above 300 K .....	67
A.3 Summary .....	69
<b>Appendix B Utilization of terahertz field effect transistor detectors .....</b>	<b>70</b>
B.1 Imaging Setup .....	70
B.2 Communication setup.....	75
<b>Bibliography .....</b>	<b>79</b>
<b>Publications of the Author .....</b>	<b>88</b>

## Acronyms and Glossary

THz	Terahertz
2D	Two-dimensional space
2DEG	Two-dimensional electron gas
<i>AC</i>	Alternating Current
BWO	Backward wave oscillator
CMOS	Complementary metal–oxide–semiconductor
<i>CW</i>	Continuous wave
<i>DC</i>	Direct Current
DIP	Dual-in-line package
Eq	Equation
FET	Field-effect transistor
Fig	Figure
GaAs	Gallium arsenide
GaN	Gallium nitride
HEMT	High-electron-mobility transistor
IC	Integrated circuit
III-V	Semiconductor compounds of III and V groups
InGaAs	Indium gallium arsenide
MoM	Method of Moments
MOSFET	Metal–oxide–semiconductor field-effect transistor
NEP	Noise-equivalent power
Ref	Reference
RF	Radio frequency
SBD	Schottky barrier diodes
Si	Silicon

## Symbols

$A_{\text{dif}}$	Airy disk diameter
$\mathfrak{S}_{ir}$	Radiation intensity
$a, \beta$	Current fitting coefficients
$C'$	Capacitance per unit area
$G$	Antenna gain coefficient
$\gamma$	Coefficient of frequency dependence
$\eta$	Ideality factor of sub-threshold slope
$i_L$	Current in the detector - readout circuit
$j$	Current density
$k_B$	Boltzmann's constant
$k_{th}$	Temperature coefficient of threshold voltage
$k_{\mu}$	Temperature coefficient of mobility
$L$	Channel length
$L_{\text{eff}}$	Characteristic length of rectification
$m$	Electron effective mass
$P_{\text{ant}}$	Incident radiation power
$q$	Electronic charge
$R_{ch}$	Transistor channel resistance
$R_L$	Load resistance
$R_V$	Sensitivity
$R_{VI}$	Relatively responsivity
$T$	Temperature
$\tau$	Relaxation time
$U_0$	Gate voltage swing
$V_{DS}$	Drain voltage
$V_{GS}$	Gate voltage
$V_{th}$	Threshold voltage
$V_{tr}$	Antenna voltage

$W$	Channel width
$Z_{ant}$	Antenna impedance
$Z_L$	Load impedance
$\Delta U$	Photoresponse
$\Delta U_{sat}$	Saturation photoresponse
$\eta_{ant}$	Antenna fitting parameter
$\eta_L$	Loading divider coefficients
$\lambda$	Wavelength
$\mu_n$	Mobility in the transistor channel
$\sigma$	Conductivity
$\varphi_t$	Thermal voltage
$\omega$	Frequency
$\omega_m$	Modulation frequency

## List of tables

Table 1.1 Parameters of some uncooled THz wave detectors (after [1] with author's additions).....	5
Table 2.1 Layer thickness.....	16
Table 2.2 Main parameters of the Si 0.35 $\mu\text{m}$ CMOS devices. ....	17
Table 2.3 Parameters of 0.13 $\mu\text{m}$ InGaAs HEMT.....	18
Table 2.4 Materials electrical properties.....	27
Table 2.5 Geometrical parameters of antenna for 300 GHz.....	29
Table 3.1 Parameters of sample which shown in Fig. 3.1 and Fig. 3.2 .....	43
Table 4.1 Parameters of samples, which presented in Figures. 4.3 and 4.4....	59

## List of Figures

Fig. 1.1	Radiation detection systems: a) Incoherent detection system; b) Coherent detection system. RF is the low electronic frequencies. ....	3
Fig. 1.2	Qualitative space dependence of electron oscillations excited by THz signal for (a) high frequency, high mobility detector where $\omega\tau_i \gg 1$ and (b) lower frequency, lower mobility detector where $\omega\tau_i \ll 1$ . $L_{eff}$ is the characteristic length of the decay of the plasma wave excited at source side of the channel, $S, D$ - are source and drain of transistor respectively. ....	9
Fig. 1.3	a) $L_{eff}$ as a function of $U_0$ at 1.63 THz; b) $L_{eff}$ as a function of frequency below threshold. Values of mobility used: for InGaAs ( $3500 \text{ cm}^2/\text{V}\cdot\text{s}$ ), GaN ( $1500 \text{ cm}^2/\text{V}\cdot\text{s}$ ), and Si ( $800 \text{ cm}^2/\text{V}\cdot\text{s}$ ) (after [53]) .....	11
Fig. 2.1	Schematic cross section of a MOSFET. ....	16
Fig. 2.2	Micrograph of MOSFETs and bonding pads with wire-connections (after [55]). ....	16
Fig. 2.3	a) Schematic cross section of a High Electron Mobility Transistor; b) Micrograph of two transistors and bonding pads with wire-connections. ....	18
Fig. 2.4	THz FET sample in holder : a) A ceramic DIP holder with a sample; b) a microwave evaluation board with $50 \Omega$ matching lime. ....	19
Fig. 2.5	The NEP frequency dependences in Si n-MOSFET structure ( $W/L = 20/2 \mu\text{m}$ ) at room temperature. Circles are NEP value using measured data and $G = 1$ ; Triangles are NEP values taking into account influence of wire-bonding connections (after [62]). ....	20
Fig. 2.6.	a) The model of transistor with bonding-wire and pad contacts (see Fig. 2.2) b) The result of simulation: the substrate with model and radiation pattern of detector. ....	21
Fig. 2.7.	Simulations of wire-bonding influence onto the antenna gain of FET detector. The gain is directed along the normal to the surface (after [62]). ...	22
Fig. 2.8	Experimental photoresponse angular dependences of MOSFET structure at different radiation frequencies. The bonding-wires contacts disposition is shown in the inset. $\varphi$ is the angle between the wire-contact and the polarization of the radiation $E$ , $\theta$ is the angle between the direction of radiation propagation and the normal to the sample surface (after [66]). ....	22
Fig. 2.9	Resolving ability of the Si CMOS THz detectors, which exceeds the length of the incident wave ( $0.3 \text{ THz} = 1 \text{ mm}$ ). a) Spot width of the incident beam measured with one of the two detectors T1 and T2 shown in b. The distance between detectors T1 and T2 is $500 \mu\text{m}$ . (c) Images of the radiation spot were obtained by detectors T1 and T2. d) Intensity distributions from both detectors were obtained along the Z line (the plate c)(after [67]). ....	23
Fig. 2.10	Micrograph of the THz FET with differently designed antenna. a) detector based on InGaP/InGaAs HEMT with symmetrical bonding pads (after [45]); b) THz detectors based on Si CMOS with integrated antenna. Schematic views of THz FET detectors with antenna (after [20]). ....	25
Fig. 2.11	The intensity distribution of the incident THz radiation at the detector. The two-dimensional scanning by: a) InGaAs HEMT (see Fig. 2.10(a))	

with symmetric metallic pads (antenna); b) Si CMOS with integrated antenna (see Fig 2.10(b)); .....	26
Fig. 2.12 The model cross section of antenna structure (after [70]). .....	27
Fig. 2.13 The antenna geometry (after [70]) .....	28
Fig. 2.14 Gain frequency dependence (after [70]) .....	29
Fig. 2.15 Antenna input impedance (after [70]) .....	30
Fig. 2.16. a) Antenna gain angular dependence at 300 GHz. b) Antenna gain as function of frequency at different angles. (after [70]) .....	30
Fig. 2.17 Photoresponses to linearly polarized 300 GHz radiation as a function of sample rotation angle $\varphi$ for different antenna designs. Triangles are experimental data; dotted line is the ideal polarization dependence. ....	31
Fig. 2.18 Comparison of antenna gain shapes of simulated (see section 2.4.1) and measured data as a function of frequency. ....	32
Fig. 2.19 The part of CMOS slab with the antenna device and metallic fill patterns which was formed by metallic layers of CMOS process. ....	32
Fig.2.20 The schematic illustration of a cryostat. ....	33
Fig.2.21 a) Channel resistance of InGaAs HEMT ( $W = 22 \mu\text{m}$ ) as a function of magnetic field, at constant current $I_{DS} = 1 \mu\text{A}$ and $V_{GS} = -0,1 \text{ V}$ , $T=100 \text{ K}$ ; Dots are experimental data, line is the fitting by Eq. (2.2) б) Left ordinate is the drain-source current as a function of gate voltage. Right ordinate is the mobility as a function of gate voltage. Mobility values were determined by magneto-resistance method. ....	34
Fig. 2.22 a) Schematic drawing of the experimental setup for detector characterization. FG is a functional generator, DSM is a digital source-meter, PC is a computer, FETD is a THz FET detector. b). The 292 GHz source beam profiles at the focal point of focusing tract.....	36
Fig. 2.23 a) Schematic illustration of the experimental setup. HTM is a semitransparent mirror, PM is a parabolic mirror, OSc is an oscilloscope, RD is a reference detector, DSM is a digital source-meter, FETD is a THz FET detector. b) Wavelength distribution of THz gas laser source, thick lines were used in experiments [83] (after Ref.[82]).....	37
Fig. 2.24 Transmissivity of various polymers of different thicknesses at room temperature. Data are presented after [82]. Numbers give sheet thicknesses in mm. ....	39
Fig. 3.1 Drain current as a function of gate bias at drain voltage 50 mV for the MOSFET. b) Output characteristic. Symbols are experimental data; lines are fit according to Eq. (3.6) using parameters of MOSFET presented in Table 3.1 .....	44
Fig. 3.2 a) Drain current as a function of gate bias at drain voltage 50 mV for the HEMT with $W = 24 \mu\text{m}$ . b) Output characteristic. Symbols are experimental data; lines are fit according to Eq. (3.6) using parameters of HEMT presented in Table 3.1 .....	44
Fig. 3.3 The scheme of THz detection by FET with load and parasitic elements. $S$ , $D$ , $G$ are the source, drain and gate terminals of FET THz detector, respectively; $R_L$ is the load resistance of readout circuit, $L$ and $L_{eff}$ are length and effective detection length of transistor channel, respectively, $i_L$	

	is signal current, $V_{tr}$ is the amplitude of the external THz ac voltage, $V_{GS0}$ is the external dc bias voltage on gate. ....	49
Fig. 4.1	Photoresponce $\Delta U$ of HEMT sample ( $W=22 \mu\text{m}$ ) as a function of radiation intensity at frequency 1.07 THz. Dots are the experimental data at gate voltage -0.1 V; the solid line is a fit using theoretical prediction in Ref. [53] (after [83]).	56
Fig. 4.2	The responsivity $R_{VI}$ as function of THz radiation intensity $\mathfrak{I}_{ir}$ , for several GaAs HEMTs with different gate widths ( $W=12, 16, 22, 24, 40 \mu\text{m}$ ) and frequencies. All curves were measured at $V_{GS} = -0.1 \text{ V}$ and $R_L = 50 \Omega$ . Results obtained using continue wave ( <i>cw</i> ) sources (frequencies 0.13 THz, 0.29 THz, 2.54 THz) are on the left of the vertical dotted line. Results for laser pulsed sources with frequencies 0.6 THz, 1.07 THz, 3.3 THz and FEL FEBL at 2.11 THz (stars) are shown on the right side. Only high intensity pulsed lasers permitted to observe the non-linear photoresponses of THz FETs (on the right panel) (after [83]).	58
Fig. 4.3	Left ordinate: photoresponse of HEMT ( $W=22 \mu\text{m}$ ) as a function of gate bias $V_{GS}$ in linear region of photoresponse at 0.29 THz. Triangles are photoresponses to <i>cw</i> THz radiation measured at $R_L$ 1 M $\Omega$ , 1 k $\Omega$ and 50 $\Omega$ . Full circles are photoresponse to pulsed radiation measured across 50 $\Omega$ in linear region of photoresponse at 1.07 THz. Right ordinate: dark drain current as a function of gate bias at drain voltage 50 mV for the HEMT with $W=22 \mu\text{m}$ . Stars are experimental data; dash-dot line is fit according to Eq. (3.6) using parameters of HEMT presented in Table 4.1 (after [83]).	59
Fig. 4.4	a) Photoresponses of HEMT ( $W=40 \mu\text{m}$ ) and MOSFET (parameters are present in Table 4.1) as a function of radiation intensity at frequency 0.6 THz. The gate voltages are $V_{GS} = -0.1 \text{ V}$ for HEMT and $V_{GS} = -1.4 \text{ V}$ for MOSFET. Full circles and triangles are experimental data of HEMT and MOSFET, respectively. Solid lines are fit according to phenomenological Eq. (4.1). Full circles and triangles are fitting data points according to the extended broadband model (section 3.3) using parameters of Table 4.1. b) Output characteristic of HEMT ( $W=40 \mu\text{m}$ ) and MOSFET samples. Dots and triangles are experimental for gate voltage $V_{GS} = -0.1 \text{ V}$ for HEMT and $V_{GS} = -1.4 \text{ V}$ for MOSFET, respectively. Lines are fit according to Eq. (17) using parameters of Table 4.1.	60
Fig. 4.5	Responsivity $R_{VI0}$ as a function of a radiation frequency in the linear region for pulsed detection measurement for HEMT. Ddots are experimental data of FET detectors (sample HEMT) at $\mathfrak{I}_{ir} = 10 \text{ W/cm}^2$ (after Fig. 4.2). Line is fitting of Eq.(4.2) with $\gamma=2$ . (after [83])	62
Fig. A.1	Photoresponse as a function of gate voltage at different temperatures. a) InGaAs HEMT, b) Si-MOSFET.	67
Fig. A.2	Evaluation of the maximal photoresponse value with the temperature for all studied transistors (after [84] with additional curves: Si 0.35 MOSFET and InGaAs HEMT).	67

Fig. A.3 Comparison of HEMT ( $W = 22 \mu\text{m}$ ) photoresponses vs gate bias at different temperatures in linear region at frequency 1.07 THz ( $169 \text{ W/cm}^2$ ): circles and rectangles are experimental data at $T = 293 \text{ K}$ and $T = 340 \text{ K}$ , respectively; solid lines show fitting results using Eq. (4.29) and taking into account the temperature parameters $k_{th}$ , $k_{\mu}$ (see Table 2.3) (after [83]) .....	69
Fig. B.1 Experimental set-up for detector characterization and transmission mode imaging of objects. FET is a THz FET detector, PM is a parabolic mirror, Mr is the mirror, PC is a computer, ITO is the visible transparent mirror. Fp1 and Fp2 are focal points of system .....	72
Fig. B.2 The photo shows a composite synthetic material, the black square marks a scan area.....	73
Fig B.3 a) Two-dimensional images obtained using THz radiation in transmission mode; b) Three-dimensional image, where the Z-axis displays the signal level.....	74
Fig B.4 Picture of a polymer material with the designation of the structural strain. ...	75
Fig B.5 a) Two-dimensional images obtained by using THz radiation in a reflection mode. b) The image shows the total terahertz power at each pixel (the Z-axis) as a function of the two-dimension positions. ....	75
Fig B.6 Comparison of the signal shapes of detectors at radiation frequency of 0.6 THz. White circles are a photoresponse of the THz FET detector and Black circles are a signal of the photon drag detector .....	77
Fig. B.7 THz FET (InGaAs HEMT) photoresponse waveform at 1.5 THz (pulse time < 120 ps). ....	77
Fig B.8 Experimental set-up for eye-pattern analysis. The 0.2 THz electronic source is modulated (amplitude modulation (AM)) by a PRBS pattern generator. PM is the parabolic mirror, Amp is the amplifier (after [117]).....	78
Fig B.9 Wide and high eye openings for three different data-rate frequencies of pseudo-random bit sequence: (a) 10 Mbps. (b) 50 Mbps. (c) 250 Mbps. (after [117]).....	79

## Chapter 1

### INTRODUCTION AND THEORY

This chapter provides the background of terahertz (THz) detection. Section 1.1 presents a review of the unique features of THz radiation and its applications. Section 1.2 describes detectors used in THz range of the spectrum. Section 1.3 reviews the state of research on THz detectors based on field effect transistors. The detection principles by field effect transistors and hydrodynamic model approach are explained in section 1.4

#### 1.1 Terahertz Band

Terahertz frequency band is the region of the electromagnetic spectrum, which extends from 0.1 THz to 10 THz (wavelength from 3 mm to 30  $\mu\text{m}$ , respectively) and occupies an extremely broad range of the electromagnetic spectrum between the infrared and microwave bands [1]. Multiple applications are related to unique/specific properties of THz radiation described below [2, 3]:

- Penetration: The terahertz wave can pass through the different materials with different level of the attenuation.
- Resolution: The resolution of an image increases with a decrease in the wavelength and the resolution in the terahertz band is better than that of the microwave band of the spectrum.
- Spectroscopy: Various solid and gaseous materials exhibit the signature in 0.5–3 THz band and can be used for their identification.
- Safety: Due to the low power levels, terahertz waves produce low ionization effect on the biological tissues.
- Scattering: The scattering is inversely proportional to the wavelength and so, wave dissipation is low in the terahertz band in comparison with the light wave.

- Intensity: The collimation of the wave is easier in the terahertz range of the spectrum as compared to that of the microwave.
- Communication: The significant development in enhancement of the data rate takes place, using the advanced modulation formats like orthogonal frequency division multiplexing, coherent transmission and requirement of multiple-input-multiple-output technique. In comparison with infrared, THz has low attenuation of the signal under certain atmospheric conditions, for example, like fog [4].

However, to efficiently apply these properties and to improve existing applications in THz region, there are several design issues, which need to be addressed carefully. The problems come from a lack of high power sources, efficient detectors, high gain antennas and low-loss interconnects to overcome the path loss when designing the THz devices. Advances in instrumentation and measurement systems have already allowed the use of the THz frequency range in many potential commercial applications.

## 1.2 Terahertz detectors

All radiation detection systems in THz spectral range can be divided into two groups [5]:

- incoherent detection systems (with direct detection sensors), which allow only the signal amplitude detection and which, as a rule, are broadband detection systems (see Fig. 1.1(a));
- coherent detection systems, which allow detecting not only the amplitude of the signal, but also its phase (see Fig. 1.1(b));

Coherent signal detection systems use heterodyne circuit design, since currently for the high radiation frequency range, proper amplifiers do not exist. The detected signals are transferred to much lower electronic frequencies (from 1 GHz to 30 GHz) where they are amplified by low-noise amplifiers. These systems are selective (narrow-band) detection systems[1].

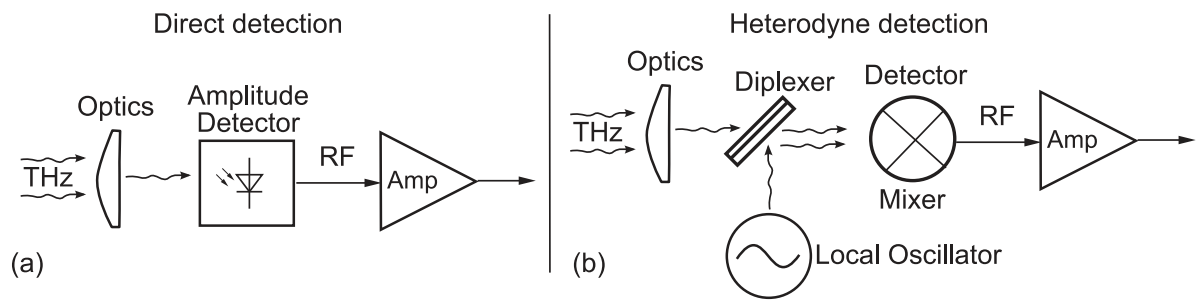


Fig. 1.1 Radiation detection systems: a) Incoherent detection system; b) Coherent detection system. RF is the low electronic frequencies.

As a first approximation, the detectors can be divided into the following groups: thermal detectors, electronic detectors, special photonic detectors (because photon energy of the THz wave is much lower than the band gap energy of typical semiconductors)

Thermal detectors (transducers) of radiation are considered to be those devices that absorb the radiation, increase their temperature, and provide a resultant electrical signal. There are several types of them, defined according to the physical mechanism that converts the temperature change to a resultant electrical signal. Goly cells are room temperature detectors made of a gas-filled chamber that changes its volume according to the incident radiation (the heating process). This type of THz detector offers a high sensitivity over the THz range, but they have the disadvantages of being fragile and having a slow response. Pyroelectric detectors are made of materials that change their dielectric constant as a function of the temperature, which increases with an incident radiation. Besides working at room temperature, the pyroelectric detectors offer the advantages of being small, portable, and less expensive than the Goly cells. On the other hand, they still have a slow response time which restricts possible applications. In the normal bolometer, the crystal lattice absorbs energy and transfers it to the free carriers via collisions. In hot electron bolometer, the incident radiation power is absorbed directly by free carriers, the crystal lattice temperature remaining essentially constant. Note that this mechanism differs from photoconductivity: In hot electron bolometer, the free-electron mobility is changed rather than electron number is

created by incident light, as it is hold for the photoconductivity. However, in both cases the detector resistance is changed [5].

Electronic detectors can usually be applied for direct and heterodyne detection because they have fast response time, in contrast with thermal detectors. Schottky barrier diodes (SBD) are the most used semiconductor devices in coherent (heterodyne) systems operating at frequencies beyond 0.5 THz. The main reason is that the nonlinear current-voltage characteristics depend (to first order) only on majority carrier transport; hence, recombination rates are unimportant for the determination of the high-frequency cut-off. As a result, temperature has only a minor effect on the SBD properties, allowing it to work at room temperature - a relevant feature for applications [6]. The nonlinear properties derive from electrons crossing a single metal/semiconductor interface; therefore, the SBD displays very low-capacitance.[7] The SBD detectors are primarily developed as single pixel detectors since the fabrication process of arrays has significant performance fluctuations of devices [8]. However, recently CMOS implementations have been successfully done including on-chip signal amplification and small arrays [9].

A promising approach is the use of field-effect transistors as THz power detectors with frequencies higher than the typical FET cut-off frequency, achieving THz values in deep-submicron transistors. More details about these detectors are discussed in the next section.

Photonic approach is a method of choice in the far-infrared region. However, the applicability of such bandgap approach to the THz region is strongly limited through the thermal energy of the carrier and usually not applicable at room temperature in THz range. For example, at  $\lambda \approx 300 \mu\text{m}$ , the photon energy  $h\nu \approx 4 \text{ meV}$  is low compared to the thermal energy of 26 meV at room temperature [1]. The cadmium mercury telluride (HgCdTe) material system is commonly used, but its performance rapidly degrades below 20 THz at 77 K operation temperature [10].

Detection in THz region has been recently demonstrated using quantum rings [11, 12] and carbon nano-tube quantum dot transistor [13]. They consist of

multiple semiconductor structures (wells) where the electron is confined in two dimensions, restricting its energy to discrete levels (energy sub-bands). In cooled conditions, electron-hole pairs are created due to the incident radiation, constituting a current that can be detected in the external circuit. Applications of these detectors usually require cooling for decreasing their thermal energy.

A summary of the state of the art THz detectors is presented in Table 1.1, with a comparison of their operation frequency and noise equivalent power. In addition, different types of detectors are described in details in Ref.[1, 5].

Table 1.1 Parameters of some uncooled THz wave detectors (after [1] with author's additions).

Detector type	Modulation frequency	Operation frequency	$NEP$ ,	Ref.
	Hz	GHz	$W/\sqrt{Hz}$	
Golay cell	$\leq 20$	$\leq 30 \times 10^3$	$\sim 10^{-9} - 5 \times 10^{-10}$	Commercial
Piezoelectric	$\leq 10^2$	$\leq 30 \times 10^3$	$\approx (1 \dots 3) \times 10^{-9}$	Commercial
Nb microbolometer	-	$\leq 30 \times 10^3$	$\geq 5 \times 10^{-11}$	[14]
SiN thin-film absorber	$\leq 200$	$\approx (1.6 \dots 4.3) \times 10^3$	$10^{-9}$	[15]
$VO_x$ microbolometer	$\leq 10^2$	$4.3 \times 10^3$	$> 3 \times 10^{-10}$	[16]
Zero bias SBDs	Up to $\sim 10^{10}$	150, 300, 400	$\sim (5 \dots 20) \times 10^{-12}$	[17]
Zero bias SBDs, ErAs/InAlGaAs/InP	-	104	$1.2 \times 10^{-12}$	[18]
Zero bias SBDs, InGaAs/InP	-	$\sim (300 \dots 700)$	$\approx 5 \times 10^{-10}$	[19]
VDI Model: WR2.2ZBD Zero Bias Detector	-	410 (330-500)	$10^{-10}$	Commercial
VDI Model: R1.5ZBD Zero Bias Detector	-	600 (500-750)	$10^{-10}$	Commercial
SBD in 0.13 digital CMOS, $CoSi_2/n-Si$	-	860	$3.2 \times 10^{-11}$	[9]
Si FET	-	295	$\approx 10^{-11}$	[20]
65 nm SiGe CMOS	-	1027	$\approx 6.6 \times 10^{-11}$	[21]
Si FET	$3 \times 10^4$	650	$3 \times 10^{-10}$	[22]
Si n-MOSFET	-	$\sim 320$	$3.2 \times 10^{-10}$	[23]
Si CMOS FET	-	595; $2.91 \times 10^3$	$4.2 \times 10^{-11}$ ; $4.87 \times 10^{-10}$	[24]
MCT hot electron bolometer	$\sim 10^6$	$\sim 75-150$	$\sim (1-3) \times 10^{-10}$	[25]

The noise equivalent power ( $NEP$ ) is one of the figures of merit for detectors and characterizes their sensitivity. It is defined as the radiation power incident on the detector generating an output signal output equal to the rms noise output (signal-to-noise ratio = 1). Intrinsic temperature fluctuation noise of a thermal detector defines its upper  $NEP$  limit as

$$NEP = \sqrt{4k_B T^2 G_{th}}. \quad (1.1)$$

where,  $k_B$  is the Boltzmann's constant,  $T$  is the temperature of the thermistor, and  $G_{th}$  is the thermal conductance between the detector and the heat sink. For the lower  $G_{th}$ , the lower values of  $NEP$  can be achieved. For  $T \approx 50$  mK and low phonon conductance  $G_{th} \approx 10$  fW/K, the values of electrical  $NEP \approx 4 \times 10^{-20}$  W/ $\sqrt{\text{Hz}}$  can be achieved at low background fluctuations conditions [1].

### 1.3 Field Effect Transistors for Terahertz Detection

The theory of THz detection in field-effect transistors (FETs) was developed by Dyakonov-Shur [26]. When THz radiation is coupled between gate and source of the FET the THz  $AC$  voltage modulates simultaneously carrier density and carrier drift velocity. As a result, THz  $AC$  signal is rectified and leads to a  $DC$  photoresponse between source and drain proportional to the received power. For high carrier mobility devices (III-V devices at cryogenic temperatures), the THz field can induce plasma waves that propagate in the channel and resonant plasma modes can be excited leading to the voltage tunable detection. [27, 28] At room temperature, plasma waves are over-damped and THz radiation leads only to a carrier density perturbation that decays exponentially with the distance from the source with the characteristic length  $L_{eff}$  that is typically on the order of a few tens of nanometers [29]. At room temperature, the broadband detection process can be alternatively explained by the model of distributed resistive self-mixing. [22, 30]. Although not treating all plasma related physics rigorously, the resistive mixing model allows a rational detector design [30, 31]. THz FET detectors show high

responsivity (up to a few kV/W), low noise equivalent power (down to 10 pW/ $\sqrt{\text{Hz}}$ ) [20], and fast response time (below 1 ns (Ref. [32]) and 30 ps (Ref.[33])). Additional interesting properties of the FET detector were recently discovered, where the photoresponse exhibits sensitivity to radiation helicity [32, 34] making FETs promising tools for the all-electric detection of the radiation Stokes parameters.

The interest in using silicon CMOS FET's as THz detectors started around 2004 after the first experimental demonstration of sub-THz and THz detection [35]. Soon afterward it was shown that Si-CMOS FET's can reach a noise-equivalent power competitive with the best conventional room temperature THz detectors [36]. Both pioneering works have clearly stated importance of Si-CMOS FETs, which present the advantages of room temperature operation, very fast response times, easy on-chip integration with read-out electronics and high reproducibility leading to straightforward array fabrication. Recent studies demonstrate the main detector characteristics, responsivity and noise equivalent power, within the same range as SBD [9, 20] (see Table 1.1). Recently, focal plane arrays in silicon technology have been designed and used for imaging at frequencies reaching the 1 THz range [22, 24, 30, 37-39]. Heterodyne detection using Si MOSFETs was also shown [40] and seems to be very promising approach for THz imaging applications. The plasma wave approach has also been extended to FET based on InAs nano-wire [41] and graphene materials [42], showing favourable results. Improvement of plasmonic THz detection by using double-grating-gate field-effect transistor structures was also demonstrated [43-46]

#### **1.4 Hydrodynamic theory of terahertz field-effect-transistor detection**

Plasma waves propagating in a FET channel have a linear dispersion law [47-49]

$$\omega = sk . \tag{1.2}$$

$$s = \sqrt{\frac{qU_0}{m}}. \quad (1.3)$$

where,  $\omega$  is a frequency,  $s$  is the plasma wave velocity,  $k$  is the wave vector,  $q$  is the electronic charge,  $m$  is the electron effective mass,  $U_0 = (V_{GS} - V_{th})$  is the gate to channel voltage swing,  $V_{GS}$  is the gate-to channel voltage,  $V_{th}$  is the threshold voltage.

THz radiation impinging on the device induces THz voltages between gate and source and/or drain and gate of the FET, depending on the contact configuration and THz field polarization. The channel nonlinearities lead to the photoresponse in the form of a *DC* voltage between source and drain or *DC* current flowing in the device and an external circuit.

The basic equations describing the plasma waves in a FET [26] are the equation of motion (the Euler equation), continuity equation, and the equation describing the gradual channel approximation [50] which is valid when the characteristic scale of the potential variation in the device channel is much larger than the gate-to-channel barrier thickness

$$\frac{\partial v}{\partial t} + v \frac{\partial U}{\partial x} + \frac{q}{m} \frac{\partial U}{\partial x} + \frac{v}{\tau_i} = 0. \quad (1.4)$$

$$\frac{\partial n}{\partial t} + \frac{\partial(nv)}{\partial x} = 0, \quad (1.5)$$

$$qn = C'U_0. \quad (1.6)$$

where,  $n$  is the carrier concentration in the channel,  $C'$  is the gate capacitance per unit area,  $\partial U/\partial x$  is the longitudinal electric field in the channel,  $v(x, t)$  is the local electron velocity,  $\tau_i$  is the momentum relaxation time. These equations do not take into account the viscosity of the electronic fluid

For an ideal intrinsic FET (with no parasitic elements), for the THz radiation inducing only the gate-to-source voltage and open circuit boundary condition at the

drain, the detector response  $\Delta U$ , which is the constant source-to-drain voltage induced by the incoming THz signal (see Fig. 1.2)[51]:

$$\frac{\Delta U}{U_o} = \frac{1}{4} \left( \frac{U_a}{U_o} \right)^2 f(\omega), \quad (1.7)$$

where,

$$f(\omega) = 1 + \beta - \frac{1 + \beta \cos(2k'_o L)}{\sinh^2(k''_o L) + \cos^2(k'_o L)} \quad (1.8)$$

$$\beta = \frac{2\omega\tau_i}{\sqrt{1 + (\omega\tau_i)^2}}, \quad (1.9)$$

$$k'_o = \frac{\omega}{s} \left( \frac{(1 + \omega^{-2}\tau_i^{-2})^{1/2} + 1}{2} \right)^{1/2}. \quad (1.10)$$

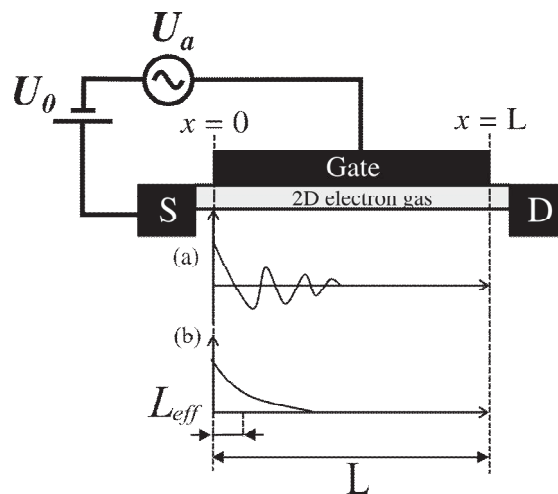


Fig. 1.2 Qualitative space dependence of electron oscillations excited by THz signal for (a) high frequency, high mobility detector where  $\omega\tau_i \gg 1$  and (b) lower frequency, lower mobility detector where  $\omega\tau_i \ll 1$ .  $L_{eff}$  is the characteristic length of the decay of the plasma wave excited at source side of the channel;  $S, D$  - are source and drain of transistor respectively.

This theory was generalized in Ref.[27] by taking into account the sub-threshold response; the Eq. (1.6) was replaced by the generalized equation of the unified charge control model [52]:

$$n = \frac{C\eta k_B T}{q^2} \ln \left[ 1 + \exp \left( \frac{qU_0}{\eta k_B T} \right) \right], \quad (1.11)$$

here,  $\eta$  is the ideality factor of FET.

For large positive values of the gate voltage swing ( $U_0 > \eta k_B T/q$ ) Eq. (1.2) coincides with Eq. (1.6) [50]. In the opposite case of large negative gate voltage swings,  $U_0 < 0$ ,  $|U_0| > \eta k_B T/q$ , the electron concentration predicted by Eq. (11) is exponentially small

$$n = \frac{C\eta k_B T}{q^2} \exp \left( \frac{qU_0}{\eta k_B T} \right) \quad (1.12)$$

Another generalization was adding the gate leakage current density,  $j_0$ , by replacing the continuity Eq. (1.5) with:

$$\frac{\partial n}{\partial t} + \frac{\partial(nv)}{\partial x} = \frac{j_0}{q}, \quad (1.13)$$

$$\Delta U = \frac{qU_a^2}{4ms^2} \left\{ \frac{1}{1 + \kappa \exp \left( -\frac{eU_0}{\eta k_B T} \right)} - \frac{1}{\left( 1 + \kappa \exp \left( -\frac{eU_0}{\eta k_B T} \right) \right)^2 \left[ \sinh^2 Q + \cos^2 Q \right]} \right\} \quad (1.14)$$

where,  $\kappa = \frac{j_0 L^2 q^2}{2C\mu\eta^2 k_B^2 T^2}$  is a low field mobility,

$$s^2 = s_0^2 \left( 1 + \exp \left( -\frac{qU_0}{\eta k_B T} \right) \right) \ln \left( 1 + \exp \left( \frac{qU_0}{\eta k_B T} \right) \right) \quad (1.15)$$

The physical meaning of parameter  $Q$  could be understood by presenting it in the following form:

$$Q = \sqrt{\frac{\omega}{2\tau}} \frac{L}{s} = \frac{L}{\sqrt{2}L_{eff}}, \quad (1.16)$$

here,  $L_{eff}$  is the characteristic length of plasma wave propagation into the channel (see Fig. 1.2)

$$L_{eff} = \sqrt{\frac{\mu_n n}{\omega (dn/dU)|_{U=V_{GS}}}}, \quad (1.17)$$

where,  $\mu_n$  is the mobility in the transistor channel

Eq.(1.17) simplifies above the threshold  $V_{th}$  to

$$L_{eff} = \sqrt{\frac{\mu_n U_o}{\omega}}, \quad (1.18)$$

Figure 1.2 shows the space profile of the plasma waves for  $\omega\tau > 1$ (a) and for  $\omega\tau < 1$  (b) in the case of a long channel, i.e.  $L \gg L_{eff}$ .

Figure 1.3 shows typical values of  $L_{eff}$  as a function of gate voltage and incident frequency for different materials.

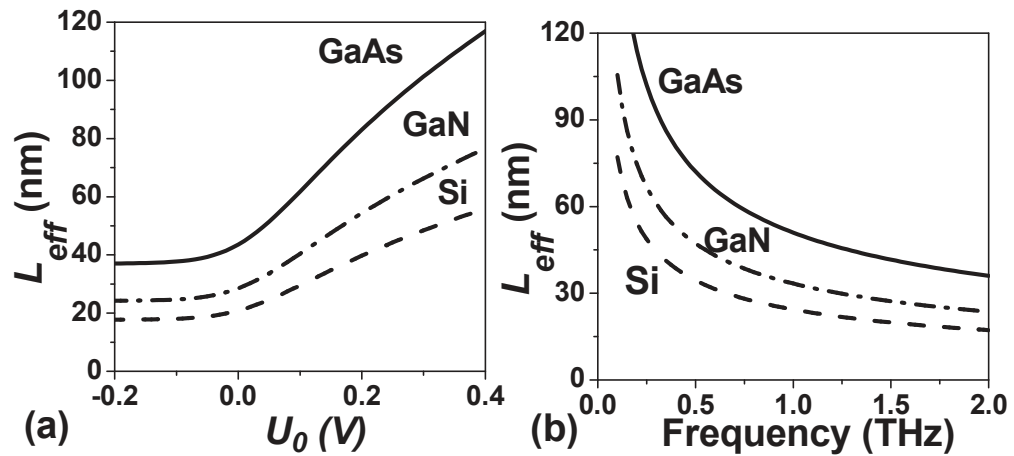


Fig. 1.3 a)  $L_{eff}$  as a function of  $U_0$  at 1.63 THz; b)  $L_{eff}$  as a function of frequency below threshold. Values of mobility used: for GaAs ( $3500 \text{ cm}^2/\text{V}\cdot\text{s}$ ), GaN ( $1500 \text{ cm}^2/\text{V}\cdot\text{s}$ ), and Si ( $800 \text{ cm}^2/\text{V}\cdot\text{s}$ ). (after [53])

For “long samples”, such that ( $L \gg L_{eff}$ ) and a negligible gate current, Eq. (1.14) simplifies to

$$\Delta U = \frac{qU_a^2}{(4\eta k_B T)} \frac{1}{\left(1 + \exp\left(-\frac{qU_0}{\eta k_B T}\right)\right) \ln\left(1 + \exp\left(\frac{eU_0}{\eta k_B T}\right)\right)}, \quad (1.19)$$

Hence, the maximum value of response  $\Delta U$  could be

$$\Delta U_{\max} \approx \frac{qU_a^2}{4\eta k_B T}, \quad (1.20)$$

and well above threshold (for  $qU_0 \gg \eta k_B T$ ),

$$\Delta U_{\max} = \frac{U_a^2}{4U_0}, \quad (1.21)$$

The maximum value depends on the power of the incident radiation and the parameter  $U_0$ . Experimentally, when the radiation modulation is used, the maximum is usually not reached due to detector loading. Thus, experimental task is to determine the boundary conditions of growth photoresponse. Another the important question is the influence of a real transistor characteristic onto a measured photoresponse.

## 1.5 Summary

This chapter has presented the state of the art of THz detectors, as well as the possible practical applications for THz systems. The development of THz FET detectors, which can operate under non-cryogenic conditions and which can be fabricated as multi-pixel imaging sensors have progressed over the last few years. CMOS manufacturing techniques provide cost-efficient solutions for most parts of the electromagnetic spectrum and can provide large arrays of detectors. Specifically, fast detectors for real-time applications, which could be integrated jointly with readout/processing electronics on the same chip. Recent progress of terahertz detectors based on field effect transistors, still leaves open questions

- Defining the boundary conditions of detection,
- Establishing relationships between the characteristics of FETs and THz radiation,
- Defining the terms of their design and manufacturing based on existing semiconductor technologies;

## Chapter 2

# SAMPLES, EXPERIMENTAL SETUP AND EXPERIMENTAL TECHNIQUES

This chapter outlines the methodology used in this research. It includes all the necessary steps used to characterization of THz FET detectors.

Basic information about the samples of transistors and tables of parameters are given in section 2.1. Section 2.2 discusses the influence of metal interconnection to transistor detection. The question about the importance of an antenna-asymmetry for detection is discussed in Section 2.3. Process of the antennas design and testing for detectors based on CMOS 0.35  $\mu\text{m}$  technological process is described in section 2.4. The technique of the low-temperature measurement and a characterization using a magnetic field are presented in section 2.5. Section 2.6 provides information about THz radiation sources used in experimental studies. Section 2.7 describes additional materials that were used in the experiments

### 2.1 Samples

As it was described in the previous chapter, various types of transistors are used for THz radiation detection (see Table 1.1). CMOS technology has always been the favored candidate for high-yield low-cost mass production. The maturity of CMOS technologies in terms of theory, design, manufacturing, characterization, and packaging has been a pivotal bridge from the most recent major technological advancements to our daily life. However, at ultra-high frequencies, CMOS technologies confront their fundamental barriers where performance begins to roll-off drastically.

A High-electron-mobility transistor (HEMT), also known as heterostructure FET (HFET), is a field-effect transistor incorporating a junction between two materials with different band gaps as the channel instead of a doped region. The current flow between two ohmic contacts (source and drain) is modulated by an

electric field created when a voltage is applied to a third—Schottky—contact (gate). The major difference between a HEMT and a MOSFET is the MOSFET's significantly higher band offset at the interface with the 2DEG, which results in a drastic reduction of the gate current in MOSFETs. On the other hand, the interface with oxide is a source of excess carrier scattering. The heterojunction interface can be made almost perfect with negligible defect density and carrier scattering resulting in high effective mobility in III-V HEMT devices as compared with Si-MOSFET devices. However, Ref. [54] have shown that the Si MOSFET shows a competitive cut-off frequency performance comparing to InGaAs HEMTs and GaAs pHEMT's. The Si MOSFET takes advantage of (i) its generic device structure with a very thin oxide barrier between gate and channel and a resulting large ratio of dielectric constant to thickness of gate oxide, and (ii) the high density of states in the Si conduction band (higher than in the III-Vs with high mobility). This compensates for the poor transport properties, in particular the low mobility, of the MOSFET inversion channels. A promising option for future high-frequency FETs circuits is to combine the successful MOSFET concept and high-mobility III-V channels.

One of the goals of this work was to compare detection capability of detectors based on HEMTs and MOSFETs. In this section, we present only basic device parameters and some aspects of both technologies. Measured and simulated *DC* characteristics are discussed in Section 3.1. Different devices are compared in Chapter 4.

### **2.1.1 Silicon metal-oxide-semiconductor field-effect transistors**

MOSFET devices under study were fabricated in a standard industrial 0.35  $\mu\text{m}$  and CMOS process on bulk silicon. Hence, the minimum permissible gate length is 350 nm. Thickness of substrate is 450  $\mu\text{m}$ . Figure 2.1 shows the cross section of the front and back-end of FET in this technology.

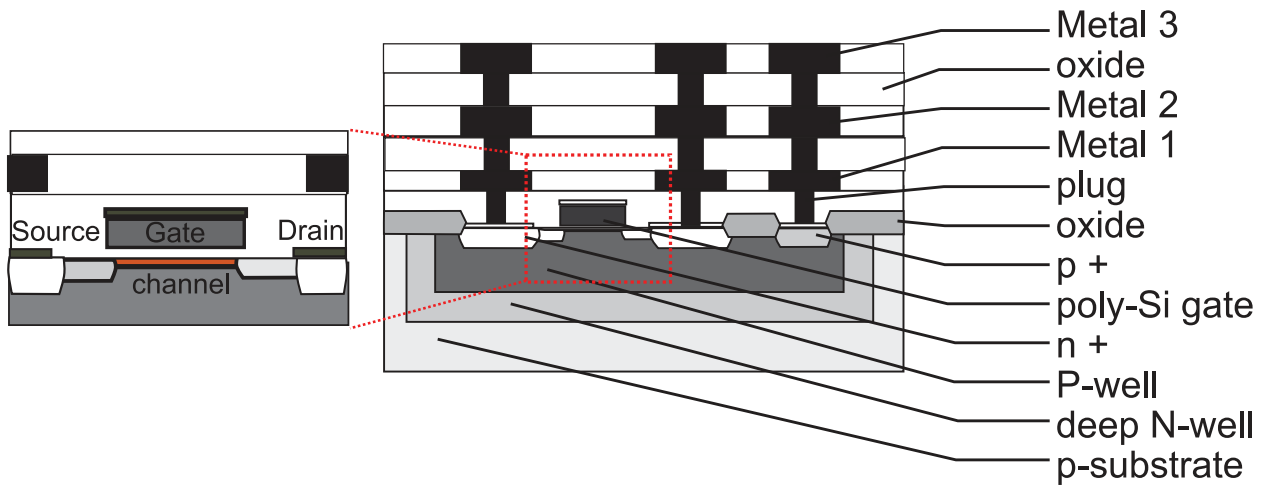


Fig.2.1 Schematic cross section of a MOSFET.

All metallic layers and via's have a height 5  $\mu\text{m}$ . This back-end can be repurposed for monolithic integration of antennas. More information about antennas can be found in Section 2.4.

Table 2.1 Layer thickness.

Layer	[nm]	Materials
Metal 3	860	AlCu
Oxide	950	SiO <sub>2</sub>
Metal 2	440	AlCu
Oxide	950	SiO <sub>2</sub>
Metal 1	400	AlCu
Oxide	1370	SiO <sub>2</sub>

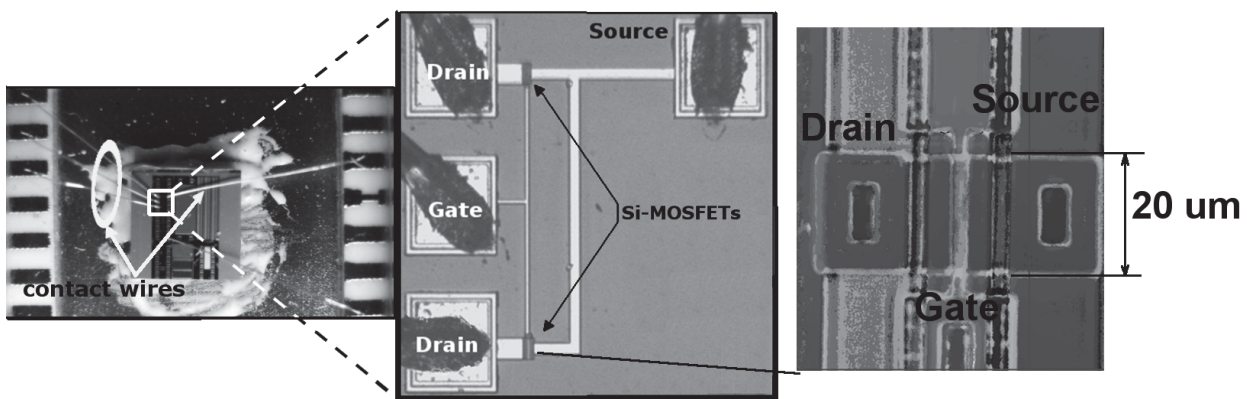


Fig.2.2 Micrograph of MOSFETs and bonding pads with wire-connections (after [55]).

Table 2.2 summarizes general parameters of MOSFETs. Channel transistor dimensions were in the range from 0.35  $\mu\text{m}$  to 20  $\mu\text{m}$ .

Table 2.2 The main parameters of the Si 0.35  $\mu\text{m}$  CMOS devices.

Extrapolated threshold voltage 10/10	$V_{th}$	0.585	V
Extrapolated threshold voltage 10/0.35	$V_{th}$	0.6	V
Gain factor 10/10	$G_m$	170	$\mu\text{A}/\text{V}^2$
Capacitance per unit area	$C'$	3.50	$\text{fF}/\mu\text{m}^2$
Saturation current 0.35 $\mu\text{m}$ at 3.3 V	$I_{sat}$	500	$\mu\text{A}/\mu\text{m}$
Ideality factor	$\eta$	1.75	-
Carrier density of substrate	$n_{sub}$	208	$10^{15}/\text{cm}^3$
Effective mobility	$\mu$	375	$\text{cm}^2/\text{Vs}$
Temperature coefficient of $V_{th}$	$k_{th}$	-1.1	$\text{mV}/^\circ\text{C}$
Temperature coefficient of mobility	$k_\mu$	-1.8	-
Transition frequency		25	GHz

### 2.1.2 High electron mobility transistors

We used AlGaAs/InGaAs p-HEMT devices with 0.13  $\mu\text{m}$  gate length. These devices were designed by RPI Troy Labs and manufactured by TriQuint [56]. This process was targeted for low noise amplifiers, linear power amplifiers, RF switches and power detectors and couples.

The basic structure of the investigated HEMT is shown in Fig. 2.3(a). In addition to the short channel these devices have an "air-bridge". An air-bridge is a bridge of metal running above the surface of the die. The air-bridge technology enables a small parasitic capacitance. Thickness of substrate is 85  $\mu\text{m}$  with front-side metallization [56].

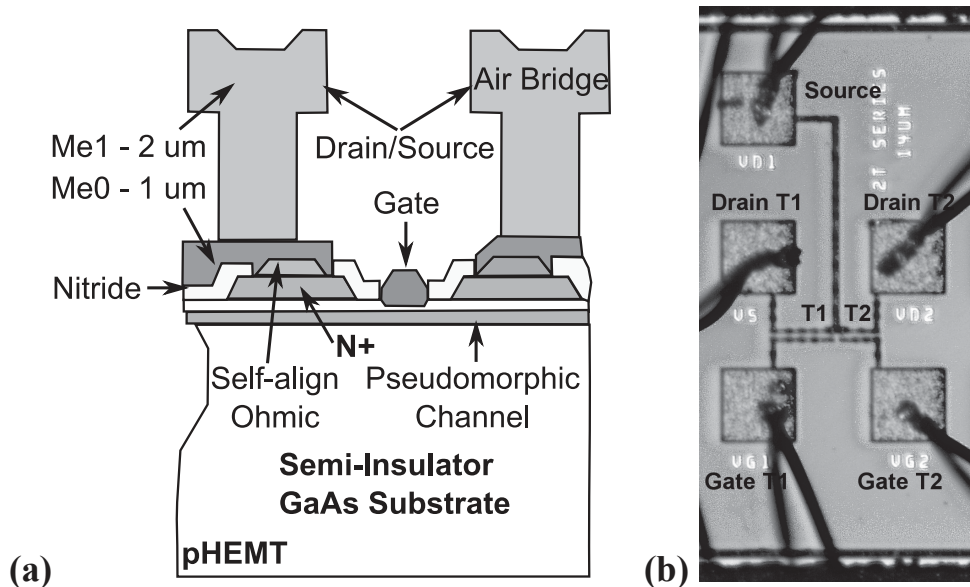


Fig.2.3 a) Schematic cross section of a High Electron Mobility Transistor; b) Micrograph of two transistors and bonding pads with wire-connections.

Table 2.3 Parameters of 0.13  $\mu\text{m}$  InGaAs HEMT

Extrapolated threshold voltage	$V_{th}$	-0,18	V
Gain factor	$G_m$	750	mS/mm
Capacitance per unit area	$C'$	0,56	$\mu\text{F}/\text{cm}^2$
Saturation current	$I_{sat}$	500	mA/mm
Ideality factor	$\eta$	1,3	-
Effective mobility	$\mu$	2900	$\text{cm}^2/\text{Vs}$
Temperature coefficient of $V_{th}$	$k_{th}$	-0.21	mV/ $^\circ\text{C}$
Temperature coefficient of mobility	$k_\mu$	-1.6	-
Transition frequency		110	GHz

## 2.2 Antenna effect of metallic interconnections

The slabs with THz FET detectors are mounted in a ceramic dual-in-line package (DIP) (see Fig. 2.4(a)) or microwave evaluation board (see Fig. 2.4(b)). Samples are bonded to holder by thin golden wires with size up to a few mm. These bonding-wire connections could play a role of non-efficiency antennas (antenna parameters do not match to a detector impedance and an irradiation frequency) for detectors [57].

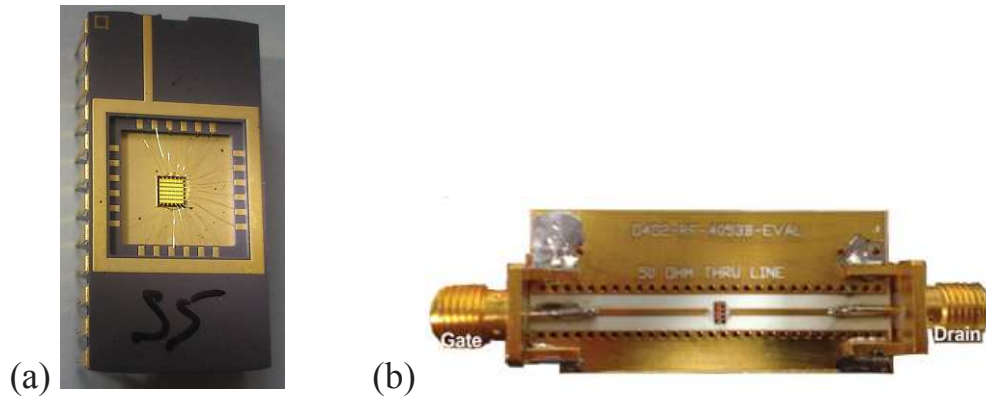


Fig. 2.4 THz FET samples in holders: a) A ceramic DIP holder with a sample; b) a microwave evaluation board with 50  $\Omega$  matching line

The focal region fields are formed by the normally incident linearly polarized plane waves. As an optical analysis indicates, these fields are represented by the well-known Airy disk (or Airy pattern) described mathematically by the amplitude distribution intensity. This description is incomplete, because it is a scalar solution, and it does not take into account polarization effects, however this analogy could be used for estimations.

A typical FET without any contacts pads and bonding-wire connections has total area a few tens of  $\mu\text{m}^2$ . FET area is much less than the diffraction limited Airy disk diameter  $A_{\text{dif}}$  of THz wave at which the most part of incident power is localized.

$$A_{\text{dif}} = 2.44\lambda_0 \frac{f_L}{rD}, \quad (2.1)$$

Here,  $f_L$  is the focal length of the optical system,  $r$  is the index of refraction of the propagation medium (air),  $D$  is the aperture diameter,  $\lambda_0$  is the incident radiation wavelength (in air). For example,  $A_{\text{dif}}$  equals 3.5 mm and 1.1 mm using teflon lens with  $r=1.38$  [58] and  $f_L=100$  mm,  $D=50.9$  mm at 300 GHz and 1 THz, respectively. Diffraction limits the performance of an optical instrument. Theoretically, an ideal imaging system concentrates 84% of the entire light intensity in the Airy disc [59]

To find out the NEP lower limit or the detector sensitivity for some frequency range one should take into account the effective antenna area  $A_\lambda$  (sensitivity

$R_V \sim A_\lambda$ ). In the case of antenna with conduction-dielectric losses,  $A_\lambda$  can be less if compared to maximum effective antenna area that is determined by [60, 61].

$$A_\lambda = \frac{\lambda^2}{4\pi} G, \quad (2.2)$$

where,  $\lambda$  is the wavelength in the propagation medium (air,  $G$  is the gain coefficient depending on the radiation frequency, the angles between normal of detector surface and radiation direction of propagation, the radiation polarization relative to antenna, the dielectric constant of substrate, their thickness and conductivity, the antenna's shape, etc.

For FET structures ( $W/L = 20/3 \mu\text{m}$ ), at room temperature at 76 GHz and an approximation  $G = 1$  the voltage sensitivity  $R_V$  and NEP were estimated as  $R_V \sim 280 \text{ V/W}$  and  $NEP \sim 6 \times 10^{-10} \text{ W}/\sqrt{\text{Hz}}$ , see also Fig. 2.5 upper curve (after [62]). These values of  $R_V$  and  $NEP$  were obtained without any special incorporated antennas (the contact wires serve as antennas). They correspond to parameters of many other uncooled THz/sub-THz detectors [1] (see Table 1.1) but really they are underestimated as no special antennas were applied. Refs [57, 62] evaluate impact of bonding-wires and contacts on the THz FET detector sensitivity.

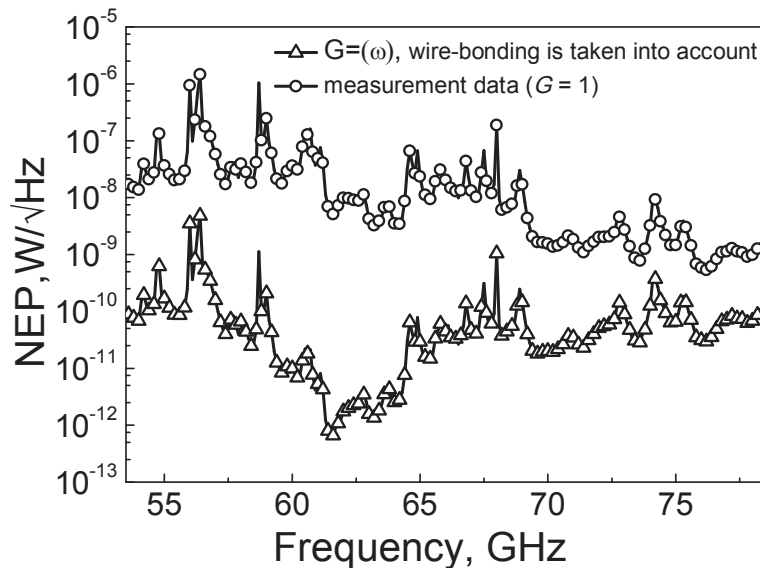


Fig. 2.5 The NEP frequency dependences in Si n-MOSFET structure ( $W/L = 20/2 \mu\text{m}$ ) at room temperature. Circles are values of NEP using measured data and  $G = 1$ ; Triangles are NEP values taking into account influence of wire-bonding connections after FEKO simulation(after [62]).

Interconnection dimensions between elements are close to wavelengths of THz radiation, in this case all conductive elements of detectors can create "quasi" antennas [63-65]. For the simulation of bonding-wire impact, a structure with antenna consisting of three antenna-wires was used (see Figs. 2.2 and 2.6). This antenna structure was included into the transistor's structure: as antennas between the drain and source, between the source and gate, and also between the gate and source. The effect of discrepancies between antennas impedances and the transistor impedance was not studied. In the simulation, we used the method of moments. The substrate was assumed to be infinite and was simulated using the software FEKO 5.5 and Method of Moments (MoM) (see Sec. 2.4.1). For simulation 30  $\mu\text{m}$  Au wires were accepted as ideal conductors and Si substrate was taken as an infinite one.

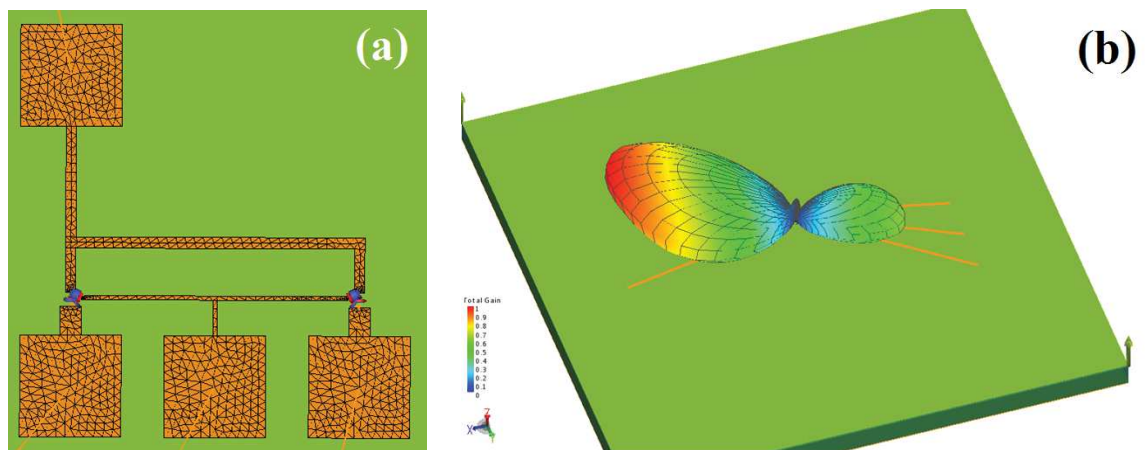


Fig. 2.6. a) The model of transistor with bonding-wire and pad contacts (see Fig. 2.2) b) The result of simulation: the substrate with model and radiation pattern of detector.

The results of simulation of the antenna's gain for two cases, i.e., only the contact pads and a system "of contact pads in combination with wire contacts" are shown in Fig. 2.7. Despite the fact that the area of the metal wire contacts is much smaller than the area of the contact pads, they make an appreciable contribution to the gain and its spectral dependence. Small values of the gain  $G$  at this frequency

range reduce the detector efficiency. This is clearly seen in Fig. 2.5, where the simulation result of  $G$  is taken into account for  $NEP$  calculation.

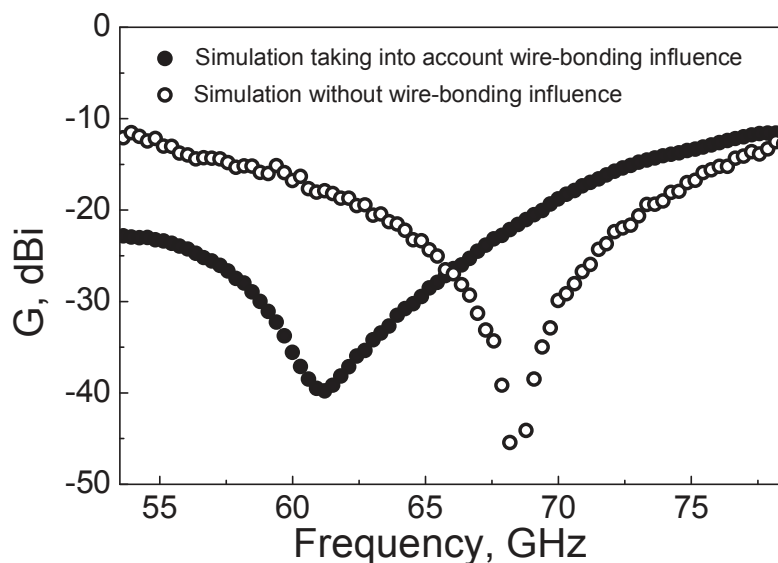


Fig. 2.7. Simulations of wire-bonding influence onto the antenna gain of FET detector. The gain is directed along the normal to the surface (after [62]).

The influence of contacts-wires for FET structures is determinative for the angle signal dependencies in a spectral range of 45–145 GHz when micro-antennas are absent (see Fig. 2.8, for 131 and 143 GHz).

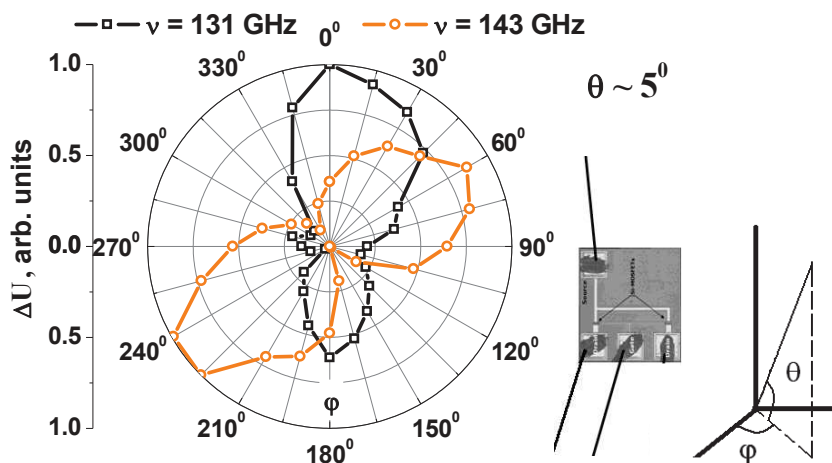


Fig. 2.8 Experimental photoresponse angular dependences of MOSFET structure at different radiation frequencies. The bonding-wires contacts disposition is shown in the inset.  $\varphi$  is the angle between the wire-contact and the polarization of the radiation  $E$ ,  $\theta$  is the angle between the direction of radiation propagation and the normal to the sample surface (after [66]).

As one can see, the long axis orientation of the lobes along the contact-wires depends on the radiation frequency and is not obviously dependent on the radiation electrical vector  $E$ -polarization. This is due to the processes of multiple reflections and attenuation of the radiation in a rather thick silicon substrate. Asymmetry of the lobes in Fig. 2.8 is conditioned by  $\theta \sim 5^\circ$  angle deviation between the direction of radiation propagation and the normal to the sample surface.

Taking into account of the bonding-wires impact could change the estimation of NEP by 2 to 3 orders (see in Fig. 2.5).

THz FET detectors in multiple-sensor arrays on common a substrate with interaction between the elements influence one another. The experimental study of spatial resolution of photoresponse of two THz FET detectors was carried out in Ref. [67]. Detectors had common bias lines, which act as an antenna, as seen in Fig. 2.9(b) (also see Sec. 2.1.1)

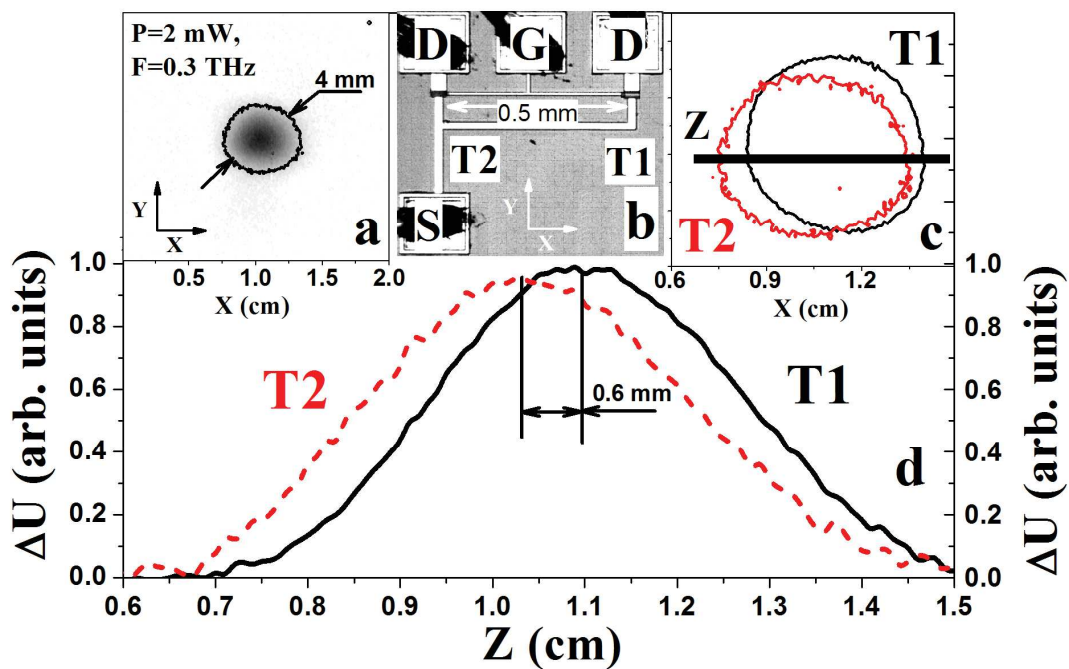


Fig. 2.9 Resolving ability of the Si CMOS THz detectors, which exceeds the length of the incident wave ( $0.3$  THz =  $1$  mm). a) Spot width of the incident beam measured with one of the two detectors T1 and T2 shown in b). The distance between detectors T1 and T2 is  $500$   $\mu\text{m}$ . (c) Images of the radiation spot were obtained by detectors T1 and T2. d) Intensity distributions from both detectors were obtained along the Z line (the plate c)(after [67]).

Figure 2.9 shows the resolving ability of the THz detectors located on a Silicon substrate. The distance of 0.5 mm between the detectors is smaller than the wavelength of the incident radiation, corresponding to 1 mm at 0.3 THz. The transistors T1 and T2 based on 1  $\mu\text{m}$  Silicon CMOS technology and used in the experiment, have channel length to width ratio of  $L/W = 2/20 \mu\text{m}$  and  $L/W = 3/20 \mu\text{m}$ , respectively (see Fig B.9(a)) [66]. FETs have common metal source and gate contacts acting as antennas. The incident beam (see section 2.6.1) is focused onto the detector with a spot diameter of 4 mm (Fig. B.9(a)). The signals from both detectors obtained along the Z-line (see Fig. B.9(c)) are shown in Fig. B.9(d). The distance of 0.6 mm measured between both photoresponse peaks approximately corresponds to the distance between detectors. The small difference is due to instrumental error related to the 0.1 mm step of scanning.

### 2.3 Terahertz detection asymmetry

Figure 2.10(a) shows THz FET detector based on InGaP/InGaAs HEMT. The detector is described in the Ref. [45] and was studied by the author in Ref. [68]. The incident THz radiation (292 GHz) is coupled to the channel via the contact pads playing the role of antennas. These contact pads are symmetric with respect to the transistor channel and comparable with the incident wavelength (2.5 mm). However, the mechanism of broadband detection by gated structures [34, 84] requires an asymmetry in channel between source and drain. The antenna connection between gate and source (or drain) can create this asymmetry. For the FET shown in Figure 2.10(a) the role of antenna feeding the radiation to the channel and creating the channel asymmetry could be played by wires. Figure 2.10(b) shows the photo of detector matrix based on Si-MOSFET fabricated in 0.25  $\mu\text{m}$  CMOS technology and the schematic representation of one detector with antenna providing the channel asymmetry [20, 69]. The low  $NEP$  (10  $\text{pW}/\sqrt{\text{Hz}}$ ) and high responsivity (1.5  $\text{kV}/\text{W}$ ) of this detector allow for use as a reference detector for radiation distribution at 292 GHz.

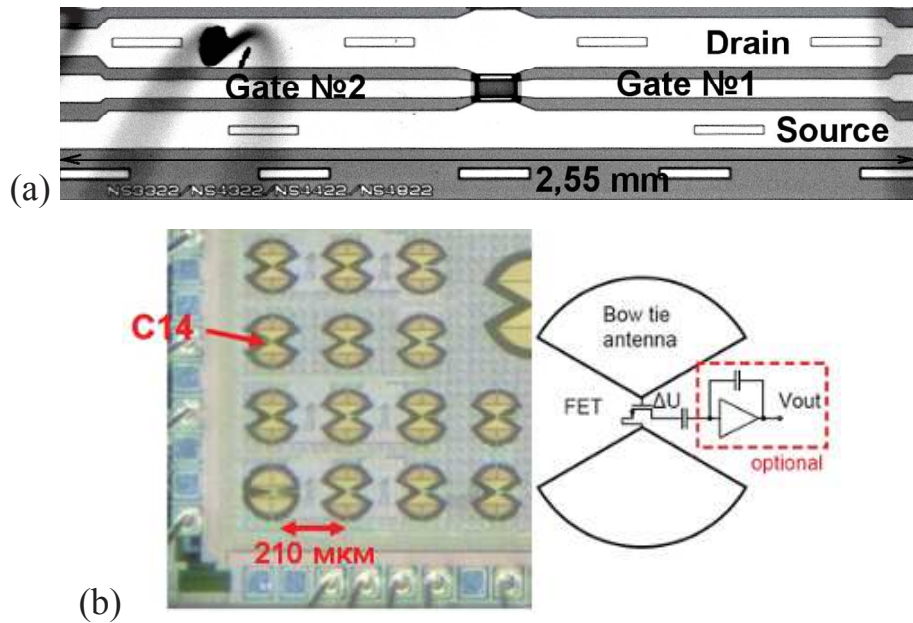


Fig. 2.10 Micrographs of the THz FET's with differently designed antennas. a) detector based on InGaP/InGaAs HEMT with symmetrical bonding pads (after [45]); b) THz detectors based on Si CMOS with integrated antenna. Schematic views of THz FET detectors with antenna (after [20]).

Figure 2.11 shows the distribution of the incident THz radiation which was obtained by using previously described detectors. The source of radiation was a continuous wave (*CW*) source based on Schottky diode at 292 GHz. The technique of experiment is typical for *CW* sources and describe in Sec. 2.6.1. The beam incident onto the has a Gaussian spatial distribution with the total area of 0.57 cm<sup>2</sup> and the total power of 4 mW.

The rectification signals depended on the position of the THz spot with respect to the contact metallic pads. If the spot is centered on the center of detector, then the signals generated at the drain and source sides lead to a compensating *DC* voltage (rectification at the both side are equal) that decreases the responsivity dramatically, as see in Fig. 2.11(a). In the opposite case, if the spot is shifted toward one side of the structure, the rectified signal is at a maximum. Two black and white regions (different sings of the detection signal) are clearly seen on the raster scan image, corresponding to the sign of the measured photoresponse as a function of the position of the spot over the structure. The amplitude and sign of the photoresponse signal as a function of the spot position on the structure are

shown under 2D-scanning image. On the left side, the signal is negative, in the middle of the device the signal turns to zero and changes its sign to become positive on the right side of the detector. The 2D- scanning image of same radiation spot is shown in Fig. 2.11(b). This image was obtained by detector based on Si-MOSFET with “good” antenna asymmetry between source and drain of transistor (see Fig. 2.10(b)) at same condition as for previous detector.

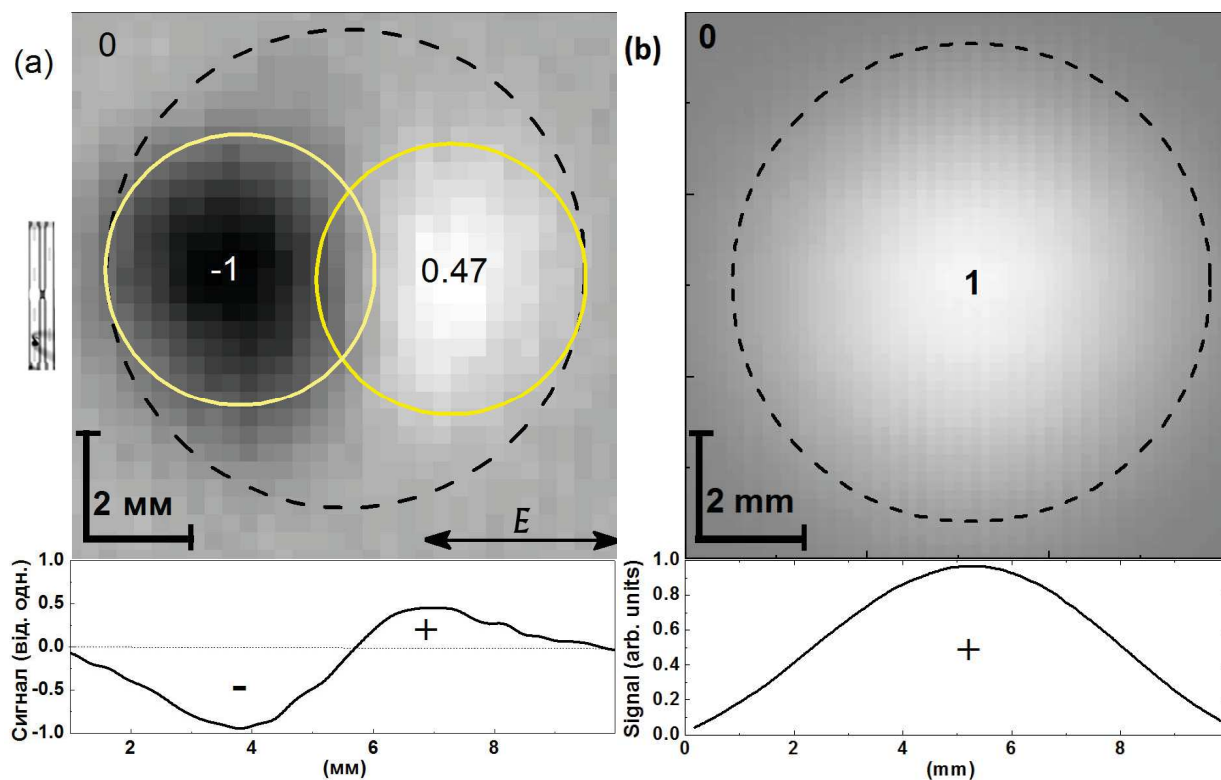


Fig. 2.11 The intensity distribution of the incident THz radiation. The two-dimensional scanning by: a) InGaAs HEMT (see Fig. 2.10(a)) with symmetric metallic pads (antenna); b) Si CMOS with integrated antenna (see Fig 2.10(b));

This example demonstrates the importance of the asymmetry of contacts in THz FET detectors.

## 2.4 Antennas for detectors based on CMOS 0.35 $\mu\text{m}$ process

Practically all IC fabrication processes involve multiple metal layers to reduce chip size. These metallic layers can be used to produce integrated on-chip antennas and to achieve a totally integrated single-chip system with additional read-out electronics. On-chip antenna could be even more cost-effective than a conventional packaging of an external antenna with transceivers considering packaging cost and its compactness at terahertz range. The area consumption of an on-chip antenna with moderate antenna gain can be comparable to a pad size. Appropriate type of antenna is chosen considering the radiation frequency.

### 2.4.1 Simulation of antenna structure

A simulation of antenna structure provides determination of the geometric dimensions of the antenna and optimized parameters in chosen frequency range. Detailed description of the simulation results is presented in the Ref.[70].

Antennas were planned to manufacturing using the first metallic layer in 0.35  $\mu\text{m}$  CMOS process (see section 2.1). Therefore, the cross section of the system has been simplified to the form, which is schematically shown in Fig. 2.12. The structure parameters listed in Table. 2.4.

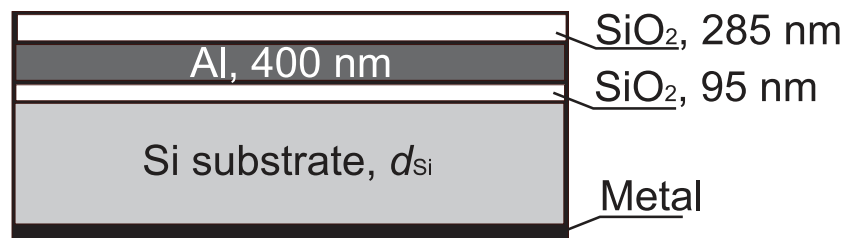


Fig. 2.12 The model cross section of the antenna structure (after [70]).

Table 2.4 The materials electrical properties

Material	$\epsilon$	$\sigma$ , S/m
<i>Si</i>	11.7	5
<i>SiO<sub>2</sub></i>	3.9	0

There are many types of planar antennas: dish and horn antennas, log-periodic, spiral, slot/aperture, etc. and antenna arrays based on some of them. We

chose to use bow tie antennas for our detectors, because of their broadband impedance and radiation characteristics. Furthermore, they are more easily integrated in the metal back end of a CMOS technology than, for instance, slot antennas.

A bowtie antenna consists of two facing each other from their pieces with a suitable gap to form a dipole antenna. This antenna shape was chosen (Fig. 2.13), because of relatively high gain in comparison with other planar printed antennas. The performance of gap bowtie antennas depends on many geometrical parameters, including bowtie size, apex angle, and gap size [60].

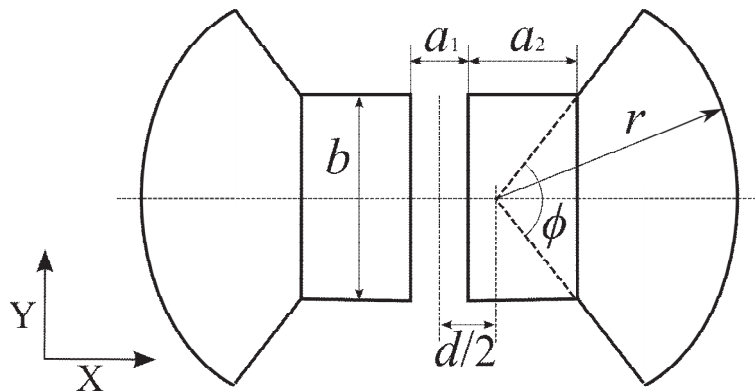


Fig. 2.13 The antenna geometry (after [70])

The planar system cross-section is shown in Fig. 2.12. The middle aluminium layer is an antenna. Passivation layers are located below and above the antenna layer. Silicon dioxide layer is manufactured during the FET production procedure. FET detectors were formed on a silicon substrate. At the backside of the substrate, the metallization layer was deposited.

Pure silicon almost does not have dispersion in the THz range. A large number of free carriers are well described by the Drude model [71]. The antenna material was considered as an ideal conductor. However, in fact, the antenna is made using aluminium. The thickness of the skin layer is about 154 nm at a frequency of 300 GHz.

We used  $a_2$ ,  $r$ ,  $d_{Si}$ ,  $\phi$ , (see Figs. 2.13) as optimization parameters of the antenna. Aluminium has high electric conductance in this frequency range that's

why it can be modeled as an ideal conductor. The antenna geometric parameters listed in Table 2.5.

Table 2.5 Geometrical parameters of the antenna for 300 GHz

$a_1$	$a_2$	$r$	$d$	$d_{Si}$	$\phi$	$b$
$\mu\text{m}$	$\mu\text{m}$	$\mu\text{m}$	$\mu\text{m}$	$\mu\text{m}$	deg	$\mu\text{m}$
10	75.8	164	20	505.5	104	191.45

The antenna was modeled using the transmitting mode as this procedure is simpler and more accurate for calculations. Antenna's behaviour is similar in receiving and transmitting modes. Optimization of antenna parameters was provided by the MOM software FEKO 5.5 [72]. The triangle edge of generating meshes was equal to  $15 \mu\text{m}$ . In the simulation, the electrical symmetry with respect to the plane of the  $X$  and the magnetic symmetry with respect to plane  $Y$  were used.

The result of simulation gain factor is shown in Fig. 2.14.

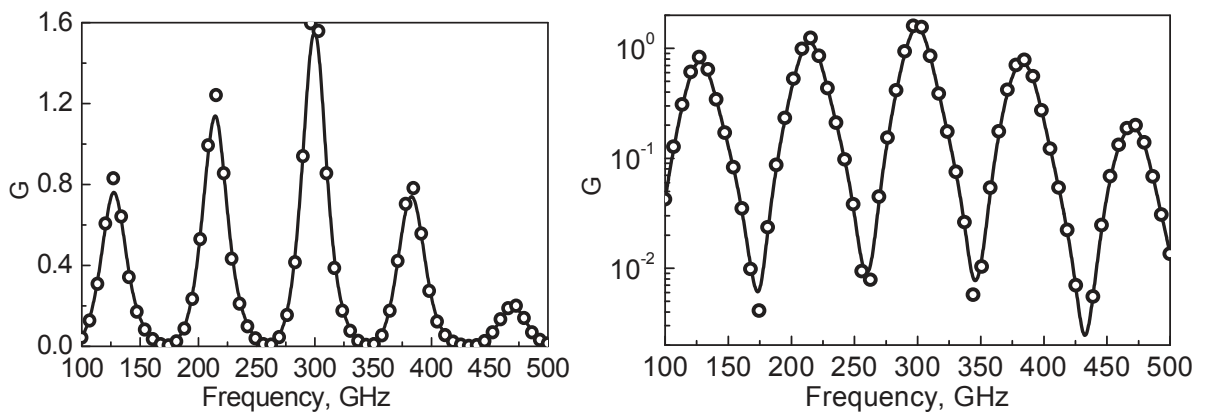


Fig. 2.14 Gain frequency dependence. (after [70])

The simulation shows that antenna gain factor is 1.6 at a frequency of 300 GHz (see Fig. 2.14). Large number of peaks are explained by the interference between incident and reflected waves from the metallic layer. It should be noted that all simulations are performed considering that the polarization of the incident wave is along the structure.

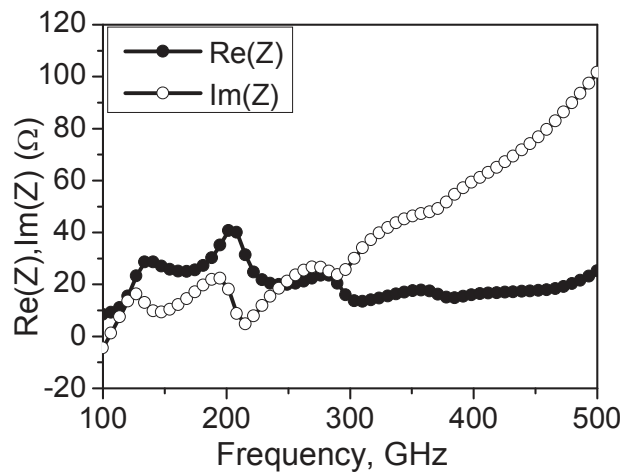


Fig. 2.15 Antenna input impedance. (after [70])

Antenna impedance is only a tens ohm (see Fig. 2.15). Small impedance of the antenna could be difficult to match with the transistor if the transistor input impedance is high.

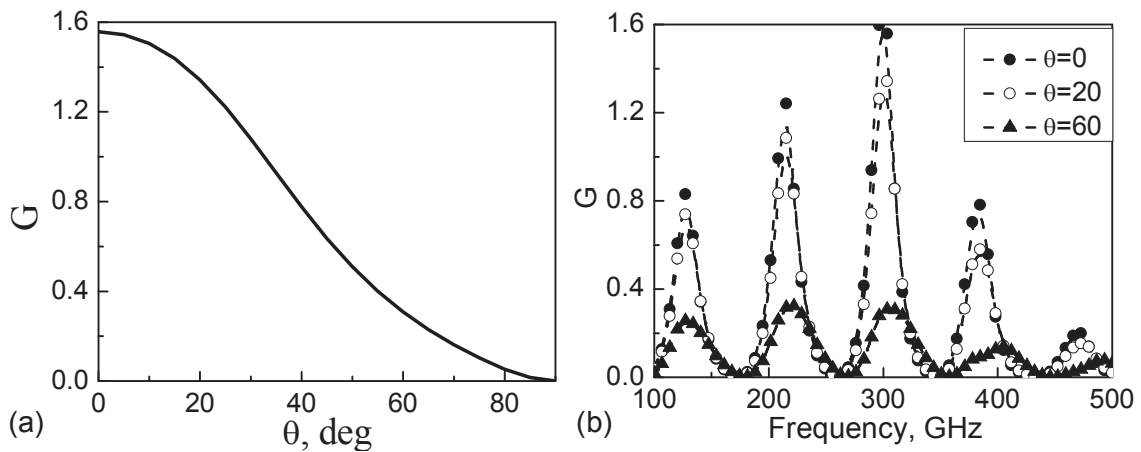


Fig. 2.16. a) Antenna gain angular dependence at 300 GHz, where  $\theta$  is the angles between the direction of radiation propagation and the normal to the sample surface; b) Antenna gain as a function of frequency at different angles.(after [70])

When the angle of incidence is increased the gain decreases (see Fig. 2.16(a)) and the maximum of gain shifts to another frequency (see Fig. 2.16(b)).

## 2.4.2 Experimental results

The response of the detectors depends on the orientation of the radiation polarization. The ideal polarization dependence of a dipole antenna should follow a  $\cos^2$  function with the rotation angle  $\varphi$  and the maximum should be obtained when the electric field vector  $E$  is parallel to the longitudinal bow-tie axis.

Our test chips with antenna devices are silicon slabs with 3 mm x 3 mm or 10 mm x 10 mm surface. Finally, slabs dimension does not influence the photoresponse.

Figure 2.17 illustrate the polarization dependence for the detector based on MOSFET with bow-tie antenna. It is close to  $\cos^2$  as a function of rotation angle.

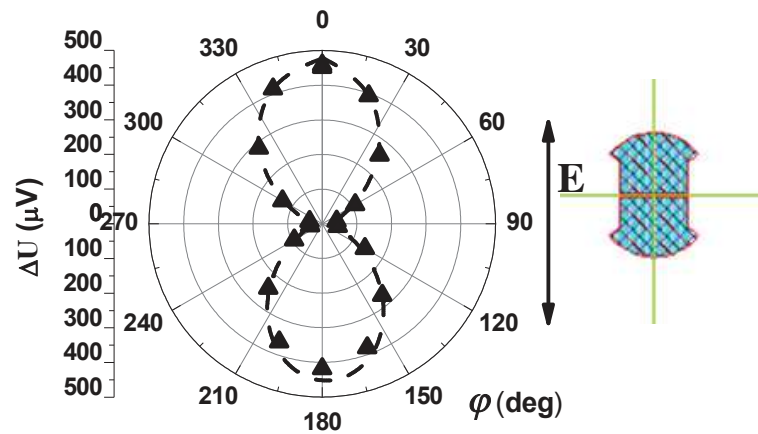


Fig. 2.17 Photoresponses to linearly polarized 300 GHz radiation as a function of sample rotation angle  $\varphi$  for different antenna designs. Triangles are experimental data; dotted line is the ideal polarization dependence.

The frequency dependence of photoresponse was also investigated. Figure 2.18 shows the comparison of measurement data and simulation. The strong frequency dependence of measurement data is not observed in this frequency range, i.e. around 300 GHz. It means that other structures on dies and/or surrounding elements change the bow-tie characteristic and contribute to the antenna coupling. The electric field vector  $E$  is locally changed. This structure could be conducting fill patterns or dielectric resonators formed by the silicon substrate slab with metallic layers.

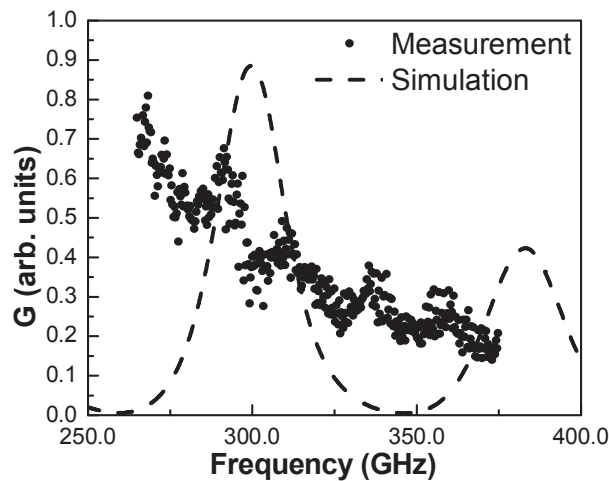


Fig. 2.18 Comparison of antenna gain shapes of simulated (see section 2.4.1) and measured data as a function of frequency.

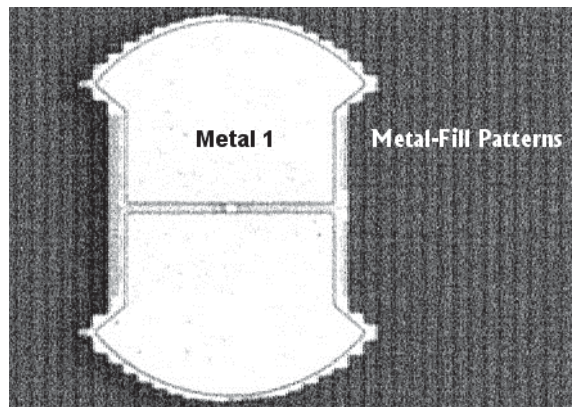


Fig. 2.19 The part of CMOS slab with the antenna device and metallic fill patterns which was formed by metallic layers of CMOS process.

Figure 2.19 shows part of the slab with the antenna and metallic fill patterns[73]. However, having conducting fill patterns close to a planar antenna has been considered undesirable; they could alter the field distribution and, therefore, the characteristics of the antennas. In order to maintain the uniformity and reproducibility of the etching and chemical mechanical polishing processes in today's deep sub-micron CMOS technology, incorporation of fill patterns in the layout, especially, on metal layers, is becoming a standard practice. Although the antenna structures have been simulated for performance optimization, analysis of the effects of fill patterns was not done [70]. Although the metal fill may have altered the electromagnetic field of the antenna in a complex way, the change of resonance frequency can be attributed mainly to the increase of the parasitic

capacitance introduced by the metal fill. For the first-order approximation, the increase of the capacitance can be correctly calculated using a simple static parallel-plate model with an accurate area estimate for the metal fill [74].

## 2.5. Measurement of electrical characteristics of transistors at different temperatures and magnetic field

Investigation of the temperature impact on FET detectors is made using a cryostat with variable temperature insert (VTI). The cryostat consists of an external vacuum chamber, a liquid nitrogen chamber, and a liquid helium chamber, as shown in Fig. 2.20.

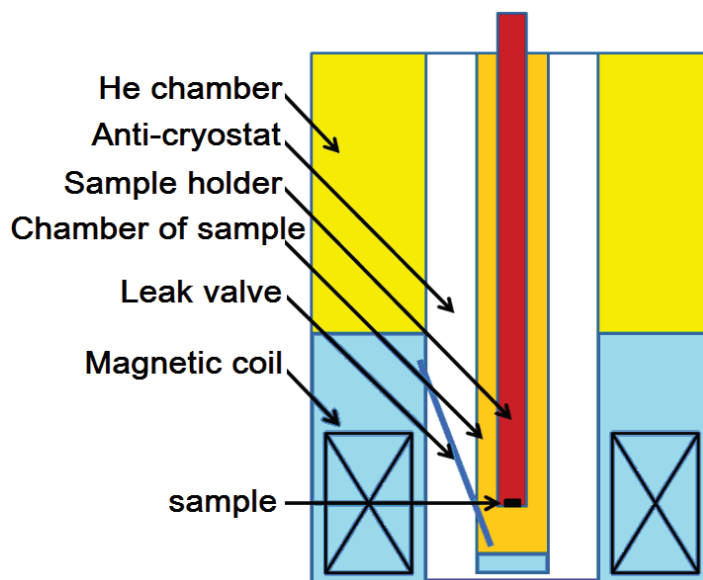


Fig.2.20 The schematic illustration of a cryostat.

The high magnetic field up to 16 T is provided by a superconducting magnetic coil working at 4 K. The magnetic coil is located inside of the helium reservoir. The anti-cryostat consists of two chambers: an outer vacuum chamber and an inner chamber of sample. The anti-cryostat structure allows to vary a temperature of a sample in the range from 4 to 300 K. The chamber with sample is connected with helium reservoir through the needle valve, providing dosing of helium in the bottom of the chamber. A heater is also located at the bottom of VTI. The pump is connected to top of the chamber. Controllable speed of pumping provides the pressure in the chamber of a sample at 10-70 mbar. The rate of helium flow, the

heater power, and the pumping speed set the pressure and the temperature inside the chamber of a sample. The feedback with the environment of the chamber is realized by using a data of a temperature sensor. The sensor is located a few centimeters from a sample and so the temperature of sensor could be different from the detector temperature. For more precise determination of temperature, a carbon resistor (Allen Bradley) was mounted directly near the detector. This type of temperature sensors has well-known dependence of resistance as a function of temperature (accuracy 0.1 K at  $T \approx 10$  K and below).

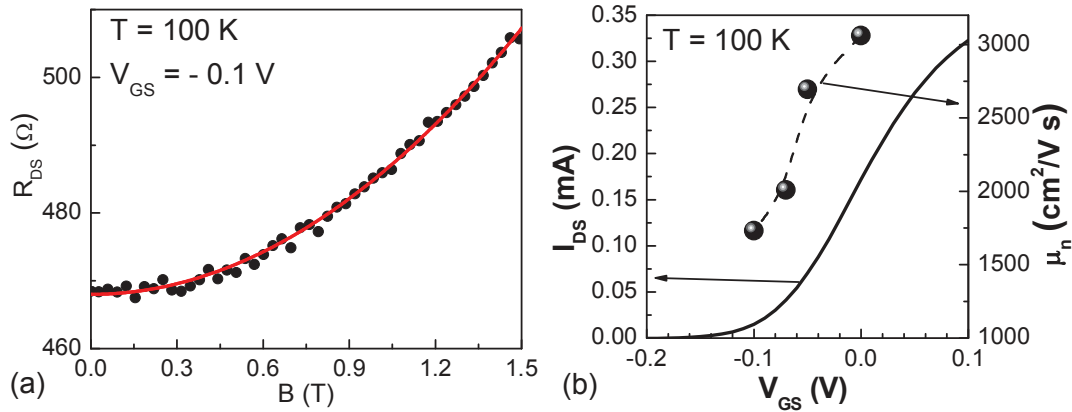


Fig.2.21 a) Channel resistance of InGaAs HEMT ( $W = 22 \mu\text{m}$ ) as a function of magnetic field, at constant current  $I_{DS} = 1 \mu\text{A}$  and  $V_{GS} = -0.1 \text{ V}$ ,  $T=100 \text{ K}$ ; Dots are experimental data, line is the fitting by Eq. (2.3) b) Left ordinate is the drain-source current as a function of gate voltage. Right ordinate is the mobility as a function of gate voltage. Mobility values were determined by magneto-resistance method.

The static parameter extraction was carried out with the digital source-meters (Keithley SourceMeter 2400 or 2410). Mobility of carriers,  $\mu_n$ , in the channel, can be determined directly from the curve of magneto-resistance at weak magnetic fields ( $\leq 2 \text{ T}$ ). In such a case, the dependence of resistance as a function a magnetic field is given by [75]:

$$R_{ch}(B, V_{GS}) = R_{ch0}(V_{GS}) \left\{ 1 + \left[ \mu_n(V_{GS}) \right]^2 B^2 \right\}, \quad (2.3)$$

where,  $R_{ch0}$  is the transistor channel resistance without a magnetic field  $B$ ,  $V_{GS}$  is the gate-source voltage.

Typical variations of the channel resistance with a typical quadratic variation are shown in Fig. 2.21(a). A contact resistance could be neglected since the majority of transistors, even in the "open state", have the channel resistance greater than  $150 \Omega$ . The magneto-resistance mobility results are with a good agreement with the effective mobility data obtained by the standard parameter extraction techniques. The applied method of mobility extraction from the magneto-resistance measurements is a promising tool for the mobility assessment in the case of nanometer FET devices, including the ultrathin silicon-on-insulator and the double gate structures [75].

## 2.6. Sources of Terahertz Radiation

To study THz FETs detectors in a wide frequency range from 0.13 THz to 3.3 THz, we used several types of monochromatic *CW* and pulsed sources operating in the wide intensity range from  $0.5 \text{ mW/cm}^2$  to  $500 \text{ kW/cm}^2$ .

### 2.6.1 Continuous-Wave Monochromatic Terahertz Radiation Sources

Continuous-wave monochromatic terahertz radiation was obtained using a industrial models of backward wave oscillator (BWO)  $\Gamma 4-141, 142, 141$  [76] (after [55, 77-80]), a *CW* methanol laser [81, 82] (after [83]), and a commercially available Schottky diode (Radiometer Physics GmbH) (after [83-85]). The operation frequencies and maximum output power levels were as follows: 129–145 GHz and middle power 15 mW (BWO  $\Gamma 4-161$ ), 292 GHz and 4.5 mW (Schottky diode source, Radiometer Physics GmbH), 2.54 THz and 20 mW (methanol laser).

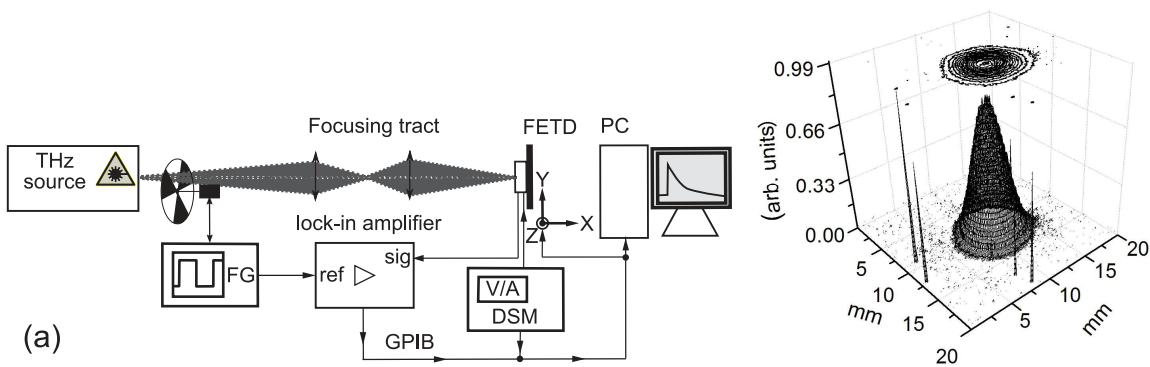


Fig. 2.22 a) Schematic drawing of the experimental setup for detector characterization. FG is a functional generator, DSM is a digital source-meter, PC is a computer, FETD is a THz FET detector. b). The 292 GHz source beam profiles at the focal point of focusing tract.

Radiation from the sources was focused by parabolic mirrors or teflon lenses. For BWO and Schottky diode, the beam spatial distribution was monitored during the experiment by a pyroelectric detector (MG-30A) and a THz FET with XY-stage at the focal point (see Fig. 2.22(a)). The beam had a Gaussian profile with 2 – 8 mm beam waist (see Fig. 2.22(b)) depending on the radiation source and wavelength. Radiation power was measured by a photo-acoustic power meter (Thomas Keating), and attenuation was controlled by changing source output power directly or by using calibrated attenuators (see section 2.7). For the methanol laser, the power and beam spatial distribution were controlled like for high-intensity lasers (see section 2.6.2). THz FET photoresponse was measured as a voltage drop over a load resistor using a lock-in amplifier or an oscilloscope.

### 2.6.2 Pulsed Terahertz Sources

We used an optically pumped molecular terahertz laser of the Regensburg Terahertz Center TerZ [86-88] and the free electron laser at Rossendorf Helmholtz Institute system FELBE [89] (after [83]). Using  $\text{NH}_3$  as the active medium for the molecular laser, we obtained linearly polarized radiation with frequencies 3.33, 2.03, and 1.07 THz. Lower frequencies of 0.78 and 0.61 THz were achieved using  $\text{D}_2\text{O}$  and  $\text{CH}_3\text{F}$ , respectively (see fig. 2.23). The molecular laser generated single

pulses with duration of about 100 ns, peak intensity  $\sim 500 \text{ kW/cm}^2$ , and a repetition rate of 1 Hz. Radiation power was controlled by the THz photon drag detector [90]. By focusing the laser beam with a parabolic mirror, we achieved an almost Gaussian profile, as recorded with a pyroelectric camera [91], and exhibiting full widths at half maximum between 1 mm (at 3.33 THz) and 3 mm (at 0.61 THz). To vary the radiation intensity, we used a set of teflon, black polyethylene, and/or pertinax calibrated attenuators (see section 2.7).

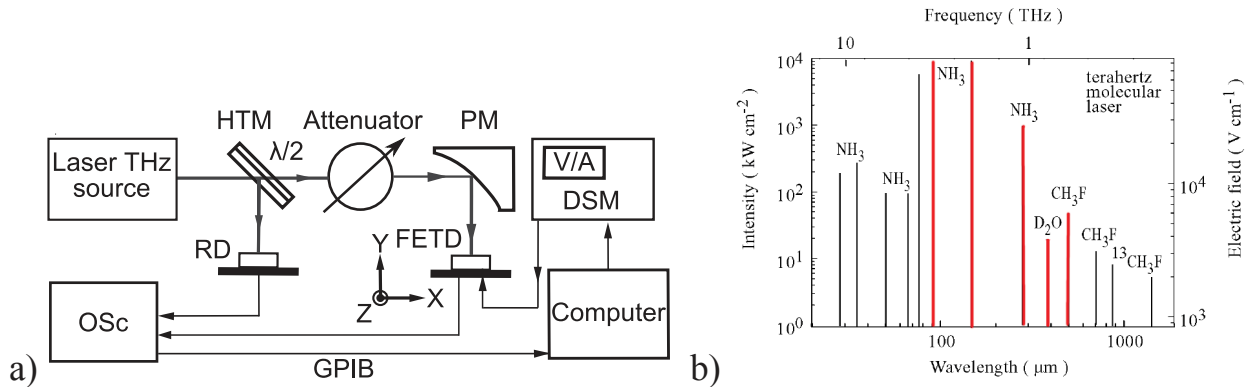


Fig. 2.23 a) Schematic illustration of the experimental setup. HTM is a semitransparent mirror, PM is a parabolic mirror, Osc is an oscilloscope, RD is a reference detector, DSM is a digital source-meter, FETD is a THz FET detector. b) Wavelength distribution of THz gas laser source, thick lines were used in experiments [83] (after Ref.[82])

The FEL provided 6.22 ps pulses at 1.55 THz and 8.4 ps pulses at 2.11 THz with a repetition rate of 13 MHz and peak intensity  $\sim 200 \text{ kW/cm}^2$ . The radiation attenuation was achieved using a series of wire grid attenuators. The beam was focused on a sample by a parabolic mirror; the resulting diameter was about 2.5 mm.

Detection signal was measured using  $50 \Omega$  or  $1 \text{ M}\Omega$  preamplifiers followed by a lock-in amplifier or an oscilloscope. The amplifier has input impedance  $50 \Omega$ , bandwidth 300 MHz and a voltage amplification of 20 dB. The peak values of the photoresponse were determined by taking into account the lock-in averaging algorithm with proper frequency and duty factors.

The experimental data obtained using high-intensity sources is described in Sec. 4.1.

## 2.7 Optical Components of the Experimental Setup

In this Section, we present the characteristics of optical components and methods most important for terahertz investigations.

Transparent solid materials are needed for various optical applications like windows for cryostats, lasers, optical cells, beam dividers, etc., and as substrates for other optical devices including gratings and polarizer's. In the terahertz range the transmission of plates of single crystals and solid polymers are widely used for rough filtering, for inspecting the spectral purity of laser radiation and for selecting single lines in multiline laser emission or for attenuation of radiation power.

Polymers are useful material for quasi-optic application in the terahertz range with the only disadvantage of not being clearly transparent in the visible spectral range. Among the large variety of available polymers, there are some of excellent terahertz transparency along with relatively low reflectivity. The best materials in this sense are polyethylene, polytetrafluor ethylene (teflon) and polystyrene. Especially the two first mentioned are therefore widely used as windows, substrates, and even for lenses in the long-wavelength part of the terahertz region. In Figs. 2.24 transmission spectra of various polymers are shown. These materials were used like attenuators of irradiation for different frequencies (see sections 2.6.1 to 2.6.2).

Polyethylene, for instance, is available in quite different modifications, especially in the low-density and in the high-density form. This makes some difference in the terahertz radiation transmissivity depending on the grade of crystallization the length of the free parts of the chains, and so on. At longer wavelengths, the transmission is structureless and flat. Going to shorter wavelengths, mainly below  $200\ \mu\text{m}$  (1.5 THz), characteristic bands of inner vibrations appear and scattering due to inhomogeneities increases. Polymers generally become increasingly opaque at shorter wavelengths. Polymers usually

have very soft cut-offs and cut-on of transmission and reflection and therefore can not be used directly as filters in the terahertz in order to cut out nearby portions of the spectrum. On the other hand, they are partly an excellent help in filtering against near-infrared radiation. Most widely used is black polyethylene which removes visible and near-infrared radiation and can be used like attenuator of radiation power.

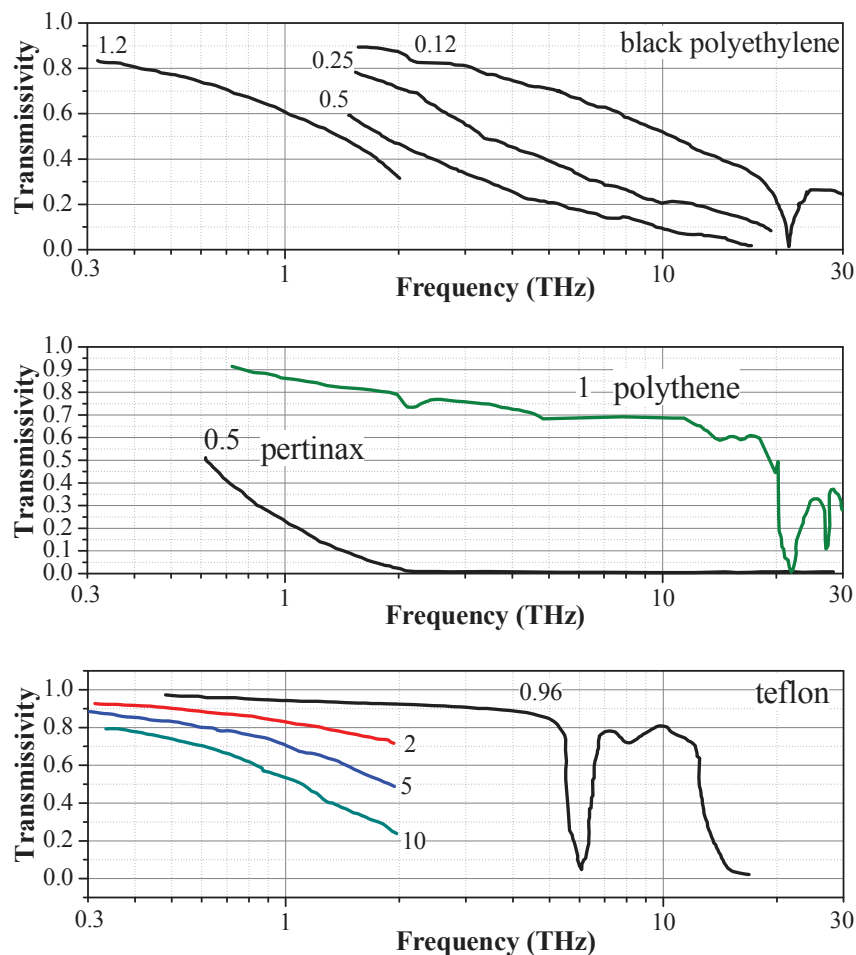


Fig. 2.24 Transmissivity of various polymers of different thicknesses at room temperature. Data are presented after [82]. Numbers give sheet thicknesses in mm.

Elaborated filter structures have been developed for the terahertz region making use of the optical properties of metallic grids and thin electroformed rectangular metallic meshes and their complementary structures or wire grids, regular arrays of cross-shaped or annular structures in thin metallic films, wave

guide array high-pass filters, thick metal gratings and combinations of these elements[82].

We used black polyethylene and pertinax as attenuators in experiments with gas lasers and electronic sources and wire grid attenuators in experiments with FELs.

## Chapter 3

# MODELS OF FIELD EFFECT TRANSISTOR TERAHERTZ DETECTION AT HIGH INTENSITIES

This chapter describes and compares the two models of FET-based THz detection. The first simple physical analytical model of the response is based on plasma density perturbation in the transistor channel by the incoming terahertz radiation and is presented in section 3.2. This analytical model of THz responses in FETs has been valid only for small input signals. Second one describes the FET from a classic electronic point of view as a distributed resistive mixer in a self-mixing configuration. This model is presented in section 3.3. We developed this analytical model for the case of large input radiation intensity and high levels of output signals. The model shows that the response becomes non-linear at large output values of responses. Section 3.4 provides the analysis of the extended model and shows that this model does not contradict to previous representations about THz FET detection. First section of this chapter presented the phenomenological model which used for description of a transistor operation at different channel inversion regimes.

### 3.1 The Phenomenological Compact Model of Field Effect Transistor

At low frequencies of operation, the electrical behaviour of field effect transistors is mathematically described according to the well-known quasi-static modeling.

Three different regimes can be defined for the operation of a FET transistor. Based on analogy of the inversion condition of the MOSFET channel, these regimes are called weak inversion, moderate inversion, and strong inversion. In general, two mechanisms are responsible for the current flow: drift and diffusion.

The weak inversion region ( $V_{GS} \ll V_{th}$ ), where the channel (drain-source) current  $I_{DS}$  has the diffusion character can be described by the following simple expression [92]:

$$I_{DS} = I_0 \times \left( 1 - e^{-\frac{V_{DS}}{\varphi_t}} \right) \times e^{\frac{V_{GS} - V_{th}}{\eta \varphi_t}} \quad (3.1)$$

where,  $I_0$  is the current factor including the ratio  $W/L$ ,  $W$  and  $L$  are the width and length of transistor channel, respectively  $V_{DS}$   $V_{GS}$  are the drain and source voltage, respectively,  $V_{th}$  is the threshold voltage,  $\varphi_t$  is the thermal voltage.

$$\varphi_t = \frac{k_B T}{q} \quad (3.2)$$

where,  $k_B$  is the Boltzmann constant,  $T$  is the temperature,  $q$  is the electron charge.

The moderate inversion region ( $V_{GS} \approx V_{th}$ ): for this region, the simple analytical expressions do not exist. Diffusion and drift components can be comparable. However, several approximate formulas exist.

In strong inversion region ( $V_{GS} \gg V_{th}$ ) the channel current has a drift character and can be described by:

$$I_{DS} = \frac{W}{L} \mu_n C' \times \left[ (V_{GS} - V_{th}) - \frac{V_{DS}}{2} \right] V_{DS} \quad (3.3)$$

$$\mu_n = \frac{\mu_0}{1 + u_a \left( \frac{V_{GS} + V_{th}}{d_{ox}} \right) + u_b \left( \frac{V_{GS} + V_{th}}{d_{ox}} \right)^2} \quad (3.4)$$

where,  $C'$  is the gate oxide capacitance per unit area,  $\mu_n$  is the electron mobility in the channel,  $\mu_0$  is the model mobility value at normal condition (example 27 C for BSIM model), and  $u_a$ ,  $u_b$  are the fitting parameters of BSIM model [93],  $d_{ox}$  is the thickness of the gate dielectric.

Following Ref. [92] we write the drain-source current  $I_{DS}(V_{DS}, V_{GS})$  as:

$$I_{DS}(V_{DS}, V_{GS}) = \frac{W}{L} \frac{\mu_0}{1 + u_a \left( \frac{V_{GS} + V_{th}}{d_{ox}} \right) + u_b \left( \frac{V_{GS} + V_{th}}{d_{ox}} \right)^2} \times C'(2\eta)\phi_t^2 \times \left[ \ln \left( 1 + \exp \left( \frac{V_{GS} - V_{th}}{2\eta\phi_t} \right) \right)^2 - \ln \left( 1 + \exp \left( \frac{V_{GS} - V_{th} - \eta V_{DS}}{2\eta\phi_t} \right) \right)^2 \right] \quad (3.5)$$

Previous THz FET models [94], [22], [62] used the expression of  $I_{DS}(V_{DS}, V_{GS})$  valid either only in the weak inversion Eq. (3.1) or only in the strong inversion regions Eq. (3.3). Equation (3.5) is a phenomenological unified equation which describes the entire range of transistor operation: strong and weak inversion ranges simultaneously.

For better matching of calculated and experimental data in the saturation region (slight current increase in Fig. 3.2(b)) we introduce in Eq. (3.5) terms containing coefficients  $\alpha$  and  $\beta$ .

$$I_{ds}(V_{ds}, V_{gs}) = \frac{W}{L} \mu_n C'(2\eta)\phi_T^2 \left\{ \left[ \ln \left( 1 + \exp \left( \frac{V_{gs} - V_{th} + \alpha\eta V_{ds}}{2\eta\phi_t} \right) \right) \right]^2 - \left[ \ln \left( 1 + \exp \left( \frac{V_{gs} - V_{th} - \beta\eta V_{ds}}{2\eta\phi_T} \right) \right) \right]^2 \right\} \quad (3.6)$$

The equation (3.5) can be obtained from (3.6) by putting  $\alpha = 0$ ,  $\beta = 1$ . The Eq.(3.5) was originally developed for silicon MOSFETs (see Fig. 3.1), but this equation describes HEMT data also sufficiently good (see Fig. 3.2). Parameters for both devices are presented in Table 3.1.

Table 3.1 Parameters of sample which shown in Fig. 3.1 and Fig. 3.2

	Материал	$L$	$W$	$V_{th}$	$\eta$	$\mu_n$	$\alpha$	$\beta$
		$\mu\text{m}$	$\mu\text{m}$	V		$\text{cm}^2/(\text{V}\cdot\text{s})$		
HEMT	InGaAs	0.13	24	-0.18	1.3	2900	0.076	0.92
MOSFET	Si	2	20	0.6	1.75	375	0.012	0.98

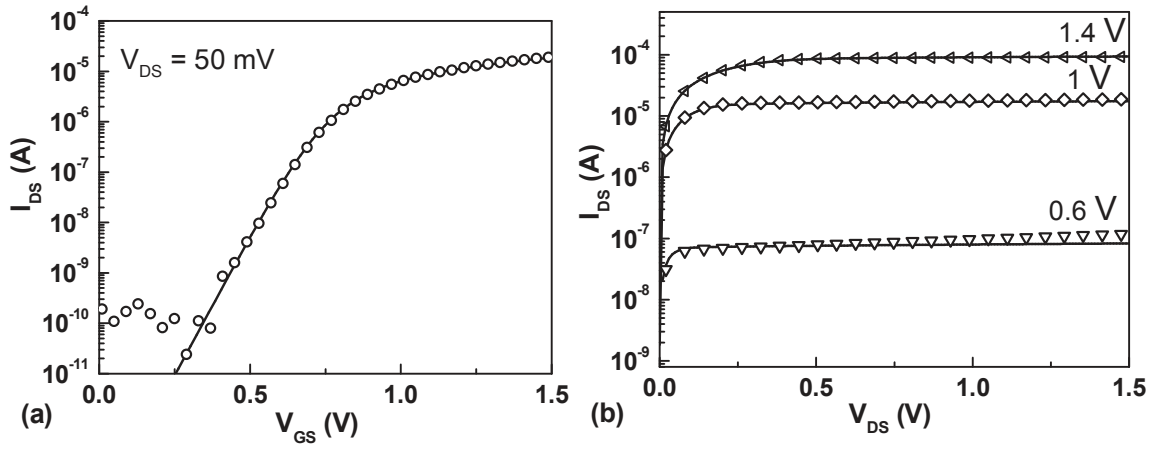


Fig. 3.1 Drain current as a function of gate bias at drain voltage 50 mV for the MOSFET. b) Output characteristic. Symbols are experimental data; lines are fit according to Eq. (3.6) using parameters of MOSFET presented in Table 3.1

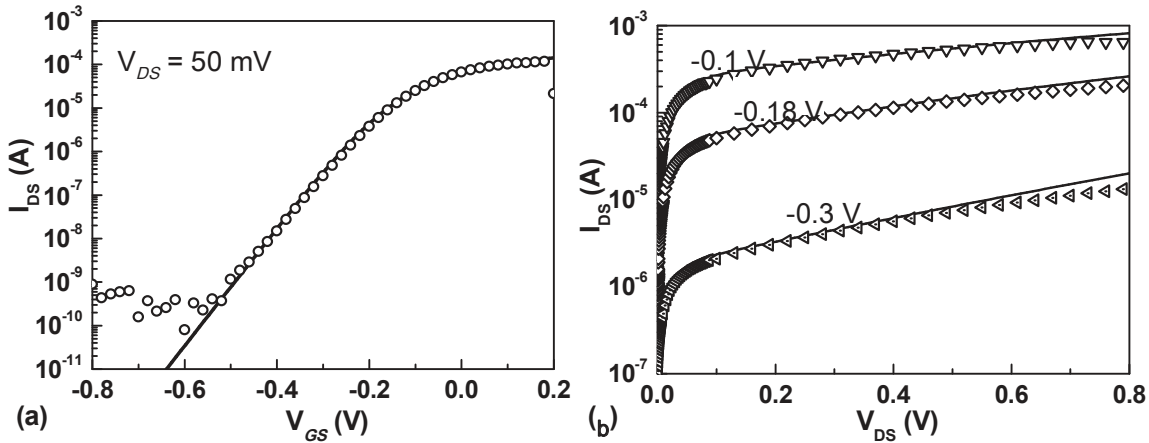


Fig. 3.2 a) Drain current as a function of gate bias at drain voltage 50 mV for the HEMT with  $W = 24 \mu\text{m}$ . b) Output characteristic. Symbols are experimental data; lines are fit according to Eq. (3.6) using parameters of HEMT presented in Table 3.1

### 3.2 Broadband Terahertz Detection Model by Lifshits-Sakowicz

The theory of broadband THz detection by FET (Ref.[50], see section 1.4) was originally developed under the assumption that the mobility in the channel does not depend on the gate to channel voltage swing  $U_0$ . However, the both the carrier density and mobility depend on the gate voltage bias in the channel [52]. Usually, it is difficult to determine precisely both carrier density and carrier

mobility in the channel as a function of the gate voltage. Fortunately, as it was shown in Ref. [95] the photoresponse of FET depends only on the product of the concentration and mobility, i.e. on the channel conductivity  $\sigma_{ch}$ . Moreover, as for the conductivity, its gate voltage dependence can be easily determined experimentally, from the transistor transfer characteristics.

Ohm's law and the continuity equation for the voltage,  $U$ , and current density,  $j$ , in the channel, are given by:

$$j = -\sigma \frac{\partial U}{\partial x}, \quad (3.7)$$

$$\frac{\partial \rho}{\partial t} + \frac{\partial j}{\partial x} = 0. \quad (3.8)$$

here,  $\sigma$  is the conductivity,  $\rho$  is the channel charge density which is proportional to the voltage  $U$ :  $\rho = C'U$ . From Equations (3.7) and (3.8) we obtain:

$$C' \frac{\partial U}{\partial t} - \frac{\partial}{\partial x} \sigma \frac{\partial U}{\partial x} = 0 \quad (3.9)$$

This equation should be solved using the boundary conditions for a long sample:

$$U|_{x=0} = U_0 + U_a \cos(\omega t), \text{ at the source, and} \quad (3.10)$$

$$U \rightarrow \text{const}, \text{ for } x \rightarrow \infty, \text{ at the drain.} \quad (3.11)$$

where,  $U_a$  is the amplitude of the radiation induced modulation of the gate-to-source voltage.

Following the method of Ref.[35] we will search for a solution of Eq. (3.9) as an expansion in powers of  $U_a$ :

$$U = V_{GS} + U_1 + U_2 + \dots \quad (3.12)$$

here,  $U_1$  is the *AC* component proportional to  $U_a$ , and  $U_2$  is the *DC* component proportional to  $U_a^2$ . For the first order of  $U_a$  we obtain

$$C' \frac{\partial U_1}{\partial t} - \sigma_0 \frac{\partial^2 U_1}{\partial x^2} = 0, \quad (3.13)$$

where  $\sigma_0 = \sigma_{ch}(V_{GS})$ . The boundary conditions follow from Eq.(3.10) and (3.11):  $U_1(0,t) = U_a \cos(\omega t)$ ,  $U_1(\infty,t) = 0$ .

The solution of Eq. (3.13) is:

$$U_1 = U_a e^{-\kappa x} \cos(\omega t - \kappa x), \quad (3.14)$$

where,  $\kappa^2 = \frac{\omega C}{2\sigma_0}$  (the above boundary condition Eq.(3.11) is valid only for a

long sample, when  $kL \gg 1$ , here  $L$  is the channel length).

For the second order of  $U_a$  after averaging Eq.(9) over time we find

$$\frac{\partial}{\partial x} \left[ \sigma_0 \frac{\partial U_2}{\partial x} + \left[ \frac{d\sigma}{dU} \right]_{U=V_{GS}} \left\langle U_1 \frac{\partial U_1}{\partial x} \right\rangle \right] = 0, \quad (3.15)$$

which means the absence of DC current. Integrating this equation with the boundary condition  $U_2(0) = 0$ , one obtains

$$U_2(x) = \frac{U_a^2}{4} \left[ \frac{1}{\sigma} \frac{d\sigma}{dU} \right]_{U=V_{GS}} (1 - \exp(-2\kappa x)). \quad (3.16)$$

Finally, the signal  $\Delta U = U_2(\infty) - U_2(0)$  is given by:

$$\Delta U = \frac{U_a^2}{4} \left[ \frac{1}{\sigma} \frac{d\sigma}{dU} \right]_{U=V_{GS}} = \frac{U_a^2}{4} \frac{d(\ln \sigma)}{dU} \Big|_{U=V_{GS}}. \quad (3.17)$$

If the mobility does not depend on the electron concentration in the channel, the conductivity is proportional to  $U$ , and Eq.(3.17) reproduces the result of Ref.[35] for the non-resonant regime ( $\omega\tau \ll 1$ ) (see Eq.(1.21). In general case, the voltage response to THz radiation,  $\Delta U$ , is proportional to the transistor transconductance ( $g_m$ ) which can be obtained from measured transfer characteristics  $I_{DS}(V_{DS}, V_{GS})$ .

A simple readout circuit is formed by a voltage divider between a THz FET detector and a load resistor. However, a real readout circuit has different parasitic circuit elements, as capacitors and inductances, which can be taken into account by introducing circuit divider coefficients (Refs.[95, 96]):

$$\eta_L = \frac{1}{1 + R_{ch} / Z_L}, \quad (3.18.1)$$

$$Z_L = R_L \parallel \frac{1}{j\omega_m C_L} . \quad (3.18.2)$$

where,  $R_{ch}$  is the channel resistance,  $Z_L$  is the complex load impedance of the setup,  $R_L$  and  $C_L$  are the resistance and the capacitance of measurement circuit,  $\omega_m$  is the modulation frequency.

Equations (3.18.1) and (3.17) binds THz FET photoresponse  $\Delta U$  with transistor transfer characteristics and parameters of readout circuit:

$$\Delta U = \frac{U_a^2}{4} \eta_L F_\sigma , \quad (3.19)$$

where,  $F_\sigma$  is the function of the channel conductivity:

$$F_\sigma = \left[ \frac{1}{\sigma_{ch}} \frac{d\sigma_{ch}}{dV_{GS}} \right]_{V_{DS} \rightarrow 0} . \quad (3.20)$$

However, Eq.(3.19) does not take into account the frequency dependence of the device antenna. This can be corrected by introduction of coefficients of power and frequency dependence. These coefficients correspond to the antenna type and antenna to channel impedance matching [97], [98], [94] (see Sec. 3.3).

### 3.3 The Extended Broadband Terahertz Detection Model

Previous THz FET broadband models [50],[99],[95] considered the case of a linear dependence of the photoresponse on the radiation power. The linear dependence at low THz radiation power is described by Eq. (3.19). However, several experimental works Ref. [100], [53], [101] showed that with a significant increase of THz radiation power this linearity is disrupted. Experimental results are presented in Sec 4.1.

The behavior of photoresponse with radiation power was investigated in Ref. [53, 102]. It was found that the response  $\Delta U$  becomes non-linear function of the power at high input power values, namely the square root function. However,

in Ref. [101] it was shown a saturation of signal in addition to sub-linear dependence with increasing power. Here we propose an extended THz FET model.

The antenna of THz FET detectors transforms incoming radiation into voltage  $V_{ant}$ . Voltage  $V_{tr}$  incoming into the detector is given by:

$$V_{tr} = \eta_{ant} V_{ant}, \quad (3.21)$$

where,  $\eta_{ant}$  is the coefficient representing losses in the parasitic elements and impedance mismatch between antenna and detector. The input impedance is defined by the impedance of the antenna transmission line.

The maximum power,  $P_{ant}$ , which is supplied to the FET channel from the antenna, is given by [60]:

$$P_{ant} = G \frac{\lambda_0^2}{4\pi} \mathfrak{I}_{ir}, \quad (3.22)$$

here,  $G$  is the antenna gain coefficient,  $\lambda_0$  is the wavelength in vacuum,  $\mathfrak{I}_{ir}$  is the radiation intensity.  $V_{ant}$  can be rewritten using Eq. (3.22):

$$V_{ant}^2 = G \frac{2}{\pi} \lambda_0^2 \mathfrak{I}_{ir} \operatorname{Re} Z_{ant}, \quad (3.23)$$

where,  $Z_{ant}$  is the antenna impedance.

Taking into account Eq. (3.23), and Eq. (3.21)  $V_{ant}$  can be rewritten as:

$$V_{tr} = k_{ant} \sqrt{\mathfrak{I}_{ir}}, \quad (3.24)$$

where,  $k_{ant}$  is the fitting parameter which depends on antenna parameters and impedance matching. This parameter is used for simplified analysis of photoresponse vs radiation intensity dependence at a constant frequency.

The function  $F_\sigma$  in Eq. (3.19) is expressed through  $\sigma_{ch}$ , which is useful for processing experimental data. When analytic expression  $I_{DS}(V_{DS}, V_{GS})$  for FET device is known,  $F_\sigma$  in Eq (3.20) can be written as:

$$F_\sigma = \left( \frac{\partial I_{DS}}{\partial V_{DS}} \right)^{-1} \frac{\partial^2 I_{DS}}{\partial V_{DS} \partial V_{GS}}, \quad (3.25)$$

The radiation-induced carrier density oscillations decay exponentially along the channel with characteristic length  $L_{eff}$  (see Fig. 1.2). The  $L_{eff}$  value can be approximately estimated using Eq. (1.18).

Our model is based on the assumption that FETs can be divided into two parts: the first with length  $L_{eff}$  where the rectification takes place (see Fig. 1.2): and the second with length  $(L - L_{eff})$  connected in series (see Fig. 3.3). THz voltage and are present only in the first part, and the second is considered as a load. To model such behavior we add elements  $L_1, L_2, C_1$  to the equivalent circuit. Inductance  $L_1$  models that THz current does not flow through the load. Inductance  $L_2$  models the absence of THz voltage on the gate of the load part with the length  $(L - L_{eff})$ . Capacitance  $C_1$  is the gate-to-channel capacitance of the load part, and  $i_c$  represents the AC THz current through the gate.  $C_g$  models two sources ( $V_{GS0}, V_{tr}$ ) decoupling. The  $v_{GS1}$  and  $v_{GS2}$  are the gate voltage at  $L_{eff}$  and  $L - L_{eff}$ , respectively.

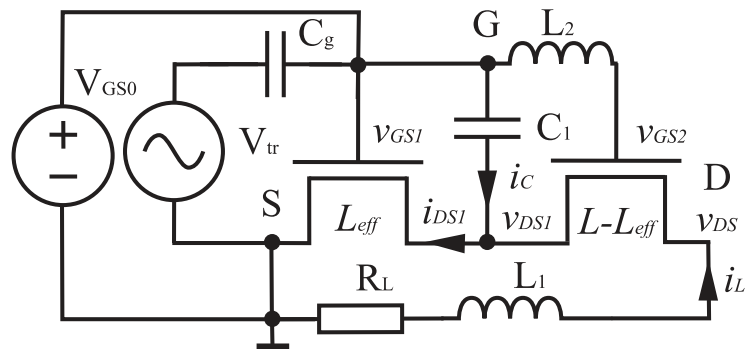


Fig. 3.3 The scheme of THz detection by FET with load and parasitic elements.  $S$ ,  $D$ ,  $G$  are the source, drain and gate terminals of FET THz detector, respectively;  $R_L$  is the load resistance of readout circuit,  $L$  and  $L_{eff}$  are length and effective detection length of transistor channel, respectively,  $i_L$  is signal current,  $V_{tr}$  is the amplitude of the external THz AC voltage,  $V_{GS0}$  is the external DC bias voltage on gate.

Let us assume that the signal current flows in the circuit formed by the detector and an external load  $R_L$ . The  $v_{DS}$  is the voltage between source and drain. The  $v_{DS1}$  is the voltage drop over characteristic length  $L_{eff}$ , and  $v_{DS2}$  is the voltage

drop on the length  $(L - L_{eff})$ . Current through part  $L_{eff}$  is given by Eq. (3.6) with corresponding values:

$$i_{DS1} = I_{DS} \left( v_{DS1}, v_{GS1}, L_{eff} \right), \quad (3.26)$$

where,

$$v_{DS1} = -v_{DS2} - R_L i_L + V_{tr} \cos(\omega t), \quad (3.27.1)$$

$$v_{GS1} = V_{GS0} + V_{tr} \cos(\omega t), \quad (3.27.2)$$

The current through part  $(L - L_{eff})$  is given by

$$i_{DS2} = I_{DS} \left( v_{DS2}, v_{GS2}, L - L_{eff} \right), \quad (3.28.1)$$

$$v_{GS2} = V_{GS0}, \quad (3.28.2)$$

$$i_L = i_{DS2}, \quad (3.28.3)$$

$$i_{DS1} = i_{DS2} + i_C, \quad (3.28.4)$$

The value of  $v_{DS2}$  is found numerically from equation  $I_{DS}(v_{DS2}, V_{GS0}, L - L_{eff}) = i_L$ .

After averaging Eq. (3.26) over the period  $\tau$  and taking into account Eqs. (3.28.1), (3.28.2), (3.28.3), (3.28.4) and  $\langle i_C \rangle = 0$  we obtain the equation for  $i_L$  current in the readout circuit:

$$i_L = \frac{1}{\tau} \int_0^\tau I_{DS} \left[ -v_{DS2} - R_L i_L + V_{tr} \cos(\omega t), V_{GS0} + V_{tr} \cos(\omega t), L_{eff} \right] dt, \quad (3.29)$$

The photoresponse  $\Delta U$  is determined as

$$\Delta U = R_L i_L \quad (3.30)$$

This model takes into account the nonlinear behavior of the channel current in a whole transistor operating range, which is especially important at high THz radiation intensities. Experimental data were successfully interpreted in the frame of the generalized model of THz FET detection, see Sec 4.1.

### 3.4 Models Comparison

This section presents a comparison of the extended model proposed in Sec. 3.3 with the model which was described in Sec. 3.2 for the case of small signals ( $(V_{tr} / k_B T) \ll 1$ ).

The potential along the gate can be considered as constant. Since, the gate impedance is much smaller than the resistance of the channel. The potential difference between the gate and the channel decreases exponentially along the channel. Thus, an alternating voltage exists only near the source on a rectification length  $L_{eff}$ . Then, a constant voltage is built at a short distance  $L_{eff}$  near the source. The internal response of detector is written as

$$i_L \approx \left. \frac{\partial I_{DS}}{\partial V_{DS}} \right|_{V_{GS}=V_{GS0}, V_{DS}=0, L=L-L_{eff}} v_{DS2} \quad (3.31)$$

$$v_{DS2} = i_L \frac{1}{\left. \frac{\partial I_{DS}}{\partial V_{DS}} \right|_{V_{GS}=V_{GS0}, V_{DS}=0, L=L-L_{eff}}} \quad (3.32)$$

Let us expand the integrand from Eq. (3.29) in Taylor series :

$$\begin{aligned} i_L = & \left. \frac{\partial I_{DS}}{\partial V_{DS}} \right|_{V_{GS}=V_{GS0}, V_{DS}=0, L=L_{eff}} \langle \delta V_{DS} \rangle + \left. \frac{\partial I_{DS}}{\partial V_{GS}} \right|_{V_{GS}=V_{GS0}, V_{DS}=0, L=L_{eff}} \langle \delta V_{GS} \rangle + \\ & \frac{1}{2} \left. \frac{\partial^2 I_{DS}}{\partial V_{DS}^2} \right|_{V_{GS}=V_{GS0}, V_{DS}=0, L=L_{eff}} \langle \delta V_{DS}^2 \rangle + \\ & \frac{1}{2} \left. \frac{\partial^2 I_{DS}}{\partial V_{DS} \partial V_{GS}} \right|_{V_{GS}=V_{GS0}, V_{DS}=0, L=L_{eff}} \langle \delta V_{DS} \delta V_{GS} \rangle + \frac{1}{2} \left. \frac{\partial^2 I_{DS}}{\partial V_{GS}^2} \right|_{V_{GS}=V_{GS0}, V_{DS}=0, L=L_{eff}} \langle \delta V_{GS}^2 \rangle \end{aligned} \quad (3.33)$$

where,

$$\delta V_{DS} = -v_{DS2} - R_L i_L + V_{tr} \cos(\omega t + \Delta\varphi) \quad (3.34)$$

$$\delta V_{GS} = V_{tr} \cos(\omega t) \quad (3.35)$$

$$\langle \delta V_{DS} \rangle = -v_{DS2} - R_L i_L \quad (3.36)$$

$$\langle \delta V_{GS} \rangle = 0 \quad (3.37)$$

$$\langle \delta V_{DS}^2 \rangle = (v_{DS2} + R_L i_L)^2 + \frac{(\Delta V_{tr})^2}{2} \quad (3.38)$$

$$\langle \delta V_{DS} \delta V_{GS} \rangle = \frac{(V_{tr})^2}{2} \quad (3.39)$$

$$\langle \delta V_{GS}^2 \rangle = \frac{(V_{tr})^2}{2} \quad (3.40)$$

where  $\Delta\phi$  is the phase shift,  $\omega=2\pi\nu$ ,  $\nu$  is the radiation frequency

We take into account the assumptions of the model in Sec. 3.2, namely that the *DC* drain bias is  $V_{DS} \rightarrow 0$ . Then we obtain two coefficients of Taylor series (3.33) equal to zero:

$$\left. \frac{\partial^2 I_{DS}}{\partial V_{GS}^2} \right|_{V_{DS}=0} = 0 \quad (3.41)$$

$$\left. \frac{\partial^2 I_{DS}}{\partial V_{DS}^2} \right|_{V_{GS}=V_{GS0}} = 0 \quad (3.42)$$

Then, Eq. (3.33) is transformed to the following form:

$$i_L = \left. \frac{\partial I_{DS}}{\partial V_{DS}} \right|_{V_{GS}=V_{GS0}, V_{DS}=0, L=L_{eff}} + \left. \frac{\partial^2 I_{DS}}{\partial V_{DS} \partial V_{GS}} \right|_{V_{GS}=V_{GS0}, V_{DS}=0, L=L_{eff}} \frac{(\Delta V_{tr})^2}{2} \quad (3.43)$$

There will make a notation

$$\alpha = \left. \frac{1}{2} \frac{\partial^2 I_{DS}}{\partial V_{DS} \partial V_{GS}} \right|_{V_{GS}=V_{GS0}, V_{DS}=0, L=L_{eff}} \quad (3.44)$$

At  $V_{DS} = 0$ , in a linear regime, a differential resistance is equal to a normal resistance

$$\left. \frac{\partial I_{DS}}{\partial V_{DS}} \right|_{V_{DS}=0} \approx \left. \frac{I_{DS}}{V_{DS}} \right|_{V_{DS} \rightarrow 0} = \sigma_{CH} = \frac{1}{R_{ch}} \quad (3.45)$$

Thus, we can present the photoresponse current in the following form and then simplify it:

$$i_L = \frac{1}{R_{ch}} \frac{L}{L_{eff}} \left\{ -i_L \frac{1}{[1/R_{ch}][L/(L-L_{eff})]} - Ri_L \right\} + \alpha \frac{L}{L_{eff}} (V_{tr})^2 \quad (3.46)$$

$$i_L = -\frac{1}{R_{ch}} \frac{L}{L_{eff}} i_L \left( R_{ch} \frac{L-L_{eff}}{L} + R_L \right) + \alpha \frac{L}{L_{eff}} (V_{tr})^2 \quad (3.47)$$

$$i_L \left( \frac{L}{L_{eff}} + \frac{1}{R_{ch}} \frac{L}{L_{eff}} R_L \right) = \alpha \frac{L}{L_{eff}} (V_{tr})^2 \quad (3.48)$$

$$i_L = \frac{\alpha (V_{tr})^2}{1 + R_L / R_{ch}} = \frac{R_{ch} \alpha (V_{tr})^2}{R_{ch} + R_L} \quad (3.49)$$

Finally, the photoresponse voltage is given by :

$$\Delta U = R_L i_L = R_{ch} \alpha (V_{tr})^2 \frac{R_L}{R_{ch} + R_L} \quad (3.50)$$

Let us rewrite previous expression supposing that  $R_{ch} \ll R_L$  as in previous theories where the voltage photoresponse was looked as:

$$\Delta U = \frac{1}{2} \frac{1}{\sigma_{ch}} \frac{d\sigma_{ch}}{dV_{GS}} V_{tr}^2 \quad (3.51)$$

The similar equation was obtained earlier in Refs. [20, 30, 37, 51, 99]. However, there the numerical coefficient was  $1/4$ . This difference in results arises because here the derivative (see Eq. 3.44) is taken as a mixed derivative with respect to  $V_{GS}$  and  $V_{DS}$ , and in the papers mentioned above the derivative actually was taken with respect to  $V_{GS}$ . In the Refs. [22, 103] the analysis was carried out for the case of strong inversion only, and this analysis was applied for all  $V_{GS}$  values [83]. It should be denoted that  $V_{tr}^2$  is frequently treated as a fitting parameter [95].

### 3.5 Summary

This chapter focuses on the mathematical models that describe behaviors of field effect transistors and detectors based on them. The present extended model is a generalization for the case of high intensities of previous models.

The new extended model of broadband field-effect transistor detectors is based on the phenomenological knowledge of the transistor static transfer characteristic. The model takes into account the nonlinear behavior of the channel current in a whole transistor operating. Another improvement of the model is that the feedback of a photoresponse is taken into account by the model.

Simulations close to the real behavior of THz FET detector and the model put limits on output signals based on transistor characteristics. Using an approach developed in this chapter, our model can also be generalized for transistors with arbitrary transfer characteristics and used to estimate loading impedances and parasitic circuit elements. This model has good agreement with experimental data, as would be shown in the next chapter.

## Chapter 4

# NONLINEAR PHOTORESPONSE OF FIELD EFFECT TRANSISTORS TERAHERTZ DETECTORS AT HIGH IRRADIATION INTENSITIES

Terahertz power dependence of the photoresponse of field effect transistors, operating at frequencies from 0.1 to 3 THz for incident radiation power density up to  $100 \text{ kW/cm}^2$  was studied for Si metal–oxide–semiconductor field-effect transistors and InGaAs high electron mobility transistors and is presented in section 4.1. Section 4.2 shows frequency dependences of the broadband detector sensitivity at frequencies from 0.6 THz to 3.3 THz. Temperature dependence of THz detection by field effect transistors was investigated in a wide range of temperatures from 275 K down to 5 K. Result of these measurements are described in section 4.3. Addition, in section 4.4 presents the case of a minor heating of detectors and additional coefficients which could take into account this impact

### 4.1 Dynamic range of Terahertz Field-Effect Transistor

The parameter  $NEP$  is a measure of a detector or detector system sensitivity. It is defined as the signal power that gives a signal-to-noise ratio of unity in a one-hertz output bandwidth. A smaller  $NEP$  corresponds to a more sensitive detector. The  $NEP$  determines the lower limit of detector sensitivity. Another important parameter of a detector, the dynamic range, is the ratio between the largest and smallest possible values of detector signals. Therefore, an important task is to determine the upper limit of the signal and also its behavior in this area.

According to the theory [50], the photoresponse of a THz FET detector should be proportional to a THz irradiation power. Linear range of a THz detector is the range of power (or intensity) of the radiation incident at the detector over which the sensitivity of the detector is constant within a specified variation, usually  $\pm 5$  percent.

The first experiments on photoresponse at high-intensity radiation were reported in Ref. [100]. It was shown that for GaAs high electron mobility transistors (HEMTs), the linearity of the photoresponse holds up to  $8 \pm 4 \text{ kW/cm}^2$  (the total power equal 11 W) of beam intensity at 240 GHz and the linear region is followed by the sub-linear one. For moderate intensity, the broadband detection by FETs versus the radiation power was studied in Ref. [53] (for infinite load resistance), who observed linear region, followed by square root dependence for higher radiation intensities. The experimental results in Ref. [53] were obtained by using the source with radiation frequency 1.63 THz and power level varying from  $9.5 \text{ W/cm}^2$  to  $510 \text{ W/cm}^2$ . The photoresponse of HEMT showed non-linear (square root) behavior at high power radiation in agreement with the theory.

We observed (Ref. [101, 104]) the photoresponse linear dependence at radiation frequency 1.07 THz (pulsed gas laser was described in Sec. 2.6.2) up to intensities of  $\sim 6.5 \text{ kW/cm}^2$ . However, our results (dots in Fig. 4.1) show a clear saturation of the photoresponse at higher intensities and cannot be described by the square root dependence (the solid line in Fig. 4.1) that was proposed by the model in Ref. [53]. This model describes signal vs. intensity dependence only partly – a deviation from the linear law and does not predict the signal saturation.

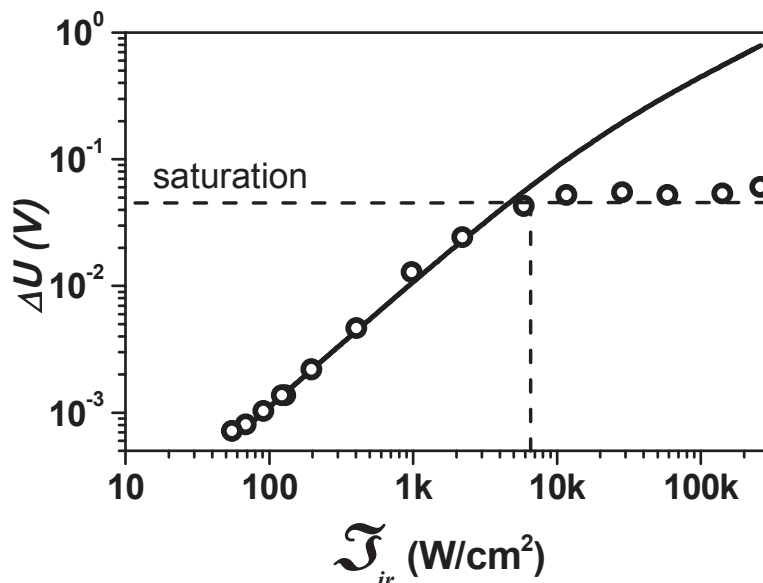


Fig. 4.1 Photoresponce  $\Delta U$  of HEMT sample ( $W = 22 \mu\text{m}$ ) as a function of radiation intensity at frequency 1.07 THz. Dots are the experimental data at gate voltage - 0.1 V; the solid line is a fit using theoretical prediction in Ref. [53]. (after [83])

We proposed the extended model of THz detection by FET in Ref. [83] to explain our experimental results on the photoresponse of detectors exposed to high-intensity radiation [101, 104]. Observed non-linearity of the signal vs. incoming power is well described by the model which is described in section 3.3. The measured and simulated photocurrent is closely related to the static characteristics of FET.

Figure 4.1 shows our typical results on the photoresponse in a wide range of radiation intensity: at low intensity we observe the linear dependence which is followed by the saturation region at high radiation intensity. The experimental points could be fitted by the phenomenological formula:

$$R_{VI}(\mathfrak{I}_{ir}) = R_{VI0} \frac{1}{1 + \mathfrak{I}_{ir} / \mathfrak{I}_{ir,sat}}, \quad (4.1)$$

where,  $R_{VI0}(\mathfrak{I}_{ir}) = \text{const}$  is the constant responsivity in the linear region ( $\mathfrak{I}_{ir} < \mathfrak{I}_{ir,sat}$ ),  $\mathfrak{I}_{ir,sat}$  is the characteristic intensity at which the signal saturates. Equation (4.1) allows to evaluate the saturation onset of signals easily.

Figure 4.2 shows the compilation of experimental results for different HEMT samples and different types of THz sources. The responsivity  $R_{VI}$  is defined as the ratio of detector photoresponse,  $\Delta U$ , to radiation intensity,  $\mathfrak{I}_{ir}$ , at the focal point of the parabolic mirror, and is plotted as a function of incident power density. To present the responsivity versus radiation intensity in a way independent of experimental conditions (pulsed, *CW* sources) we consistently used the peak signals and radiation intensity values. The left panel shows  $R_{VI}$  for *CW* sources (see. section 2.6.1) with low output intensity (less than a few mW). The right panel shows  $R_{VI}$  for high intensity pulsed sources (see. section 2.6.2).

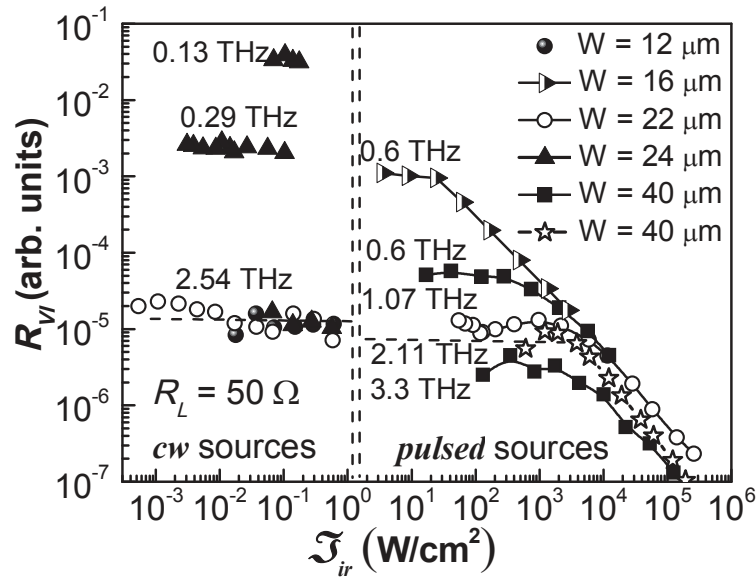


Fig. 4.2 The responsivity  $R_{VI}$  as function of THz radiation intensity  $\mathfrak{S}_{ir}$ , for several GaAs HEMTs with different gate widths ( $W=12, 16, 22, 24, 40 \mu\text{m}$ ) and frequencies. All curves were measured at  $V_{GS} = -0.1 \text{ V}$  and  $R_L = 50 \Omega$ . Results obtained using continue wave (*cw*) sources (frequencies 0.13 THz, 0.29 THz, 2.54 THz) are on the left of the vertical dotted line. Results for laser pulsed sources with frequencies 0.6 THz, 1.07 THz, 3.3 THz and FEL FEBL at 2.11 THz (stars) are shown on the right side. Only high intensity pulsed lasers permitted to observe the non-linear photoresponses of THz FETs (on the right panel). (after [83])

Figure 4.3 (left ordinate) shows normalized photoresponse (triangles) of the HEMT based detector ( $W = 22 \mu\text{m}$ ) and fitting lines as a function of gate bias  $V_{GS}$  at different loading resistances in the linear region of responsivity. Measurements were performed using a *CW* THz radiation source at frequency 292 GHz.

As one can see in Figure 4.3, the dependencies  $\Delta U(V_{GS})$  have the same shape for experiments in pulsed (triangles) and *CW* (circles) modes at load resistance of  $50 \Omega$ . This dependence,  $\Delta U(V_{GS})$  can be described by the detector models from sections 3.2 or 3.3 (at constant frequency and constant radiation intensity).

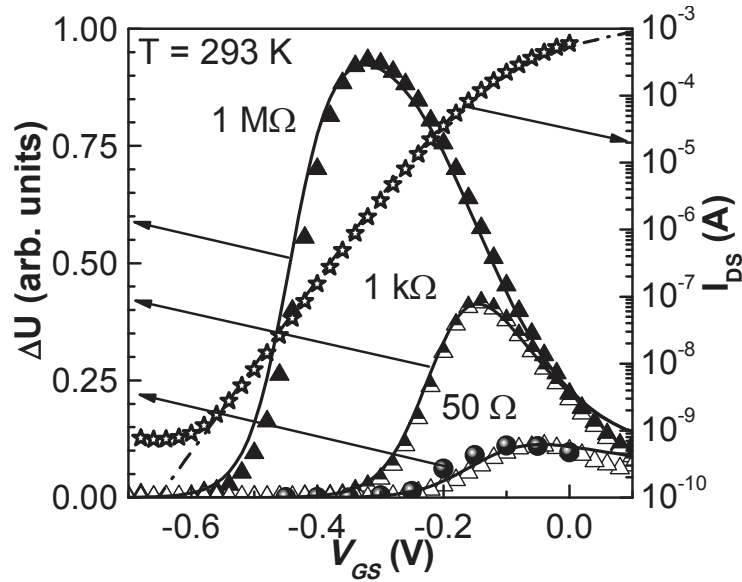


Fig. 4.3 Left ordinate: photoresponse of HEMT ( $W = 22 \mu\text{m}$ ) as a function of gate bias  $V_{GS}$  in a linear region of photoresponse at 0.29 THz. Triangles are photoresponses to CW THz radiation measured at  $R_L$  1 M $\Omega$ , 1 k $\Omega$  and 50  $\Omega$ . Full circles are photoresponse to pulsed radiation measured across 50  $\Omega$  in a linear region of photoresponse at 1.07 THz. Right ordinate: dark drain current as a function of gate bias at drain voltage 50 mV for the HEMT with  $W = 22 \mu\text{m}$ . Stars are experimental data; dash-dot line is fit according to Eq. (3.6) using parameters of HEMT presented in Table 4.1. (after [83])

This comparison of  $\Delta U(V_{GS})$  dependencies permitted us to determine correct elements of the readout circuit for pulse measurements. Since by using the load resistance 50  $\Omega$  we have the same photoresponse for pulse mode as for continuous one, we have no significant losses in the fast readout circuit and the photoresponse signal is the correct one. So we can compare our results for both modes with confidence.

Table 4.1 Parameters of samples that presented in Figures. 4.3 and 4.4

Sample	$L$ $\mu\text{m}$	$W$ $\mu\text{m}$	$V_{th}$ B	$\eta$	$\mu_n$ $\text{cm}^2/(\text{V}\cdot\text{s})$	$\alpha$	$\beta$	$L_{eff}$ nm	$k_{ant}$ $\text{cm}\cdot\text{V}/\text{W}^{1/2}$
HEMT	0.13	40	-0.18	1.3	2900	0.03	0.9	65	212
MOSFET	2	20	0.6	1.75	375	0.012	0.9	31	298

Photoresponses of InGaAs HEMT and Si MOSFET to pulsed radiation are shown in Fig. 4.4(a). Although the photoresponse magnitude between transistors differs significantly, the dependence of  $\Delta U$  on the  $\mathfrak{I}_{ir}$  is qualitatively the same: at first it is linear followed by saturation.

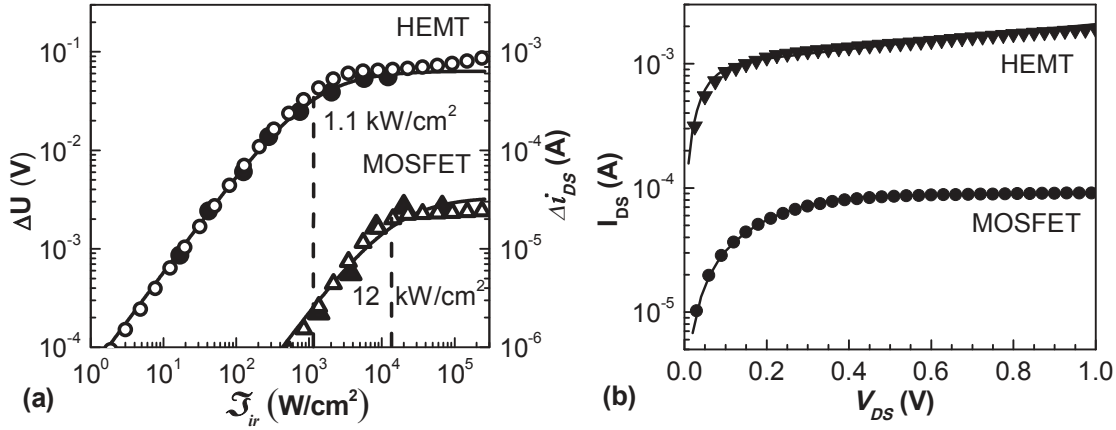


Fig. 4.4 a) Photoresponses of HEMT ( $W = 40 \mu\text{m}$ ) and MOSFET (parameters are present in Table 4.1) as a function of radiation intensity at frequency 0.6 THz. The gate voltages are  $V_{GS} = -0.1 \text{ V}$  for HEMT and  $V_{GS} = 1.4 \text{ V}$  for MOSFET. Full circles and triangles are experimental data of HEMT and MOSFET, respectively. Solid lines are fit according to phenomenological Eq. (4.1). Full circles and triangles are fitting data points according to the extended broadband model (section 3.3) using parameters of Table 4.1. b) Output characteristic of HEMT and MOSFET samples. Dots and triangles are experimental for gate voltage  $V_{GS} = -0.1 \text{ V}$  for HEMT and  $V_{GS} = 1.4 \text{ V}$  for MOSFET, respectively. Lines are fit according to Eq. (3.6) using parameters of Table 4.1.

To calculate the photoresponse the following steps are performed: i) transistor parameters are extracted from *DC* measurements data, ii) Eq. (3.29) is numerically solved to get  $i_L$  versus incoming irradiation, iii)  $\Delta U$  is found using Eq. (3.30), iv) comparing experimental and model data in the linear region, the constant  $k_{ant}$  is determined and introduced into Eq. (3.24). The model takes into account the non-linear behavior of the current in the transistor channel. The final fitting results of our model are compared with experimental data in Fig. 4.4 (a).

The saturation values of photoresponse,  $\Delta U_{sat}$ , in Fig. 4.4(a) are 70 mV for HEMT and 3 mV for MOSFET. We convert  $\Delta U_{sat}$  into the current  $\Delta i_{DS,sat}$  in the measured circuit as  $\Delta i_{DS,sat} = \Delta U_{sat} / (R_L + R_{ch})$ , where  $R_L$  and  $R_{ch}$  are the load and the transistor channel resistance, respectively, and obtain 0.7 mA and 30  $\mu$ A (as shown in the right ordinate axis in Fig. 4.4 (a)). It is important to note that these values are close to saturation currents of non-irradiated devices at the same gate bias as seen in Fig. 4.4(b). The fitting results of the extended broadband model are compared with experimental data in Fig. 4.4 (a). One can see that the model shows good agreement with the experimental data for the MOSFET in all ranges; for HEMT there is a slight deviation from experiment at high intensities. Therefore, we can with certainty state that the channel current saturation (similar to one observed in standard *DC* characteristics) is the dominating effect responsible for THz photoresponse saturation at high radiation intensities.

## 4.2 Frequency dependence of the detector sensitivity

As can be seen in Fig. 4.2, the responsivity values of THz FETs using pulsed lasers sources are slightly lower than responsivity values using *CW* sources at approximately the same frequency (2.11 THz and 2.54 THz). This difference can be explained by the systematical error of pulsed measurements, most probably related to time resolution limitations of the oscilloscope used in pulsed experiments. This systematical error leads to a slight underestimation of  $R_{VIO}$ . However, we do not perform any normalization between data obtained using two experimental set-ups because the only important fitting result is  $\mathfrak{I}_{ir,sat}$  that is independent of any multiplicative factor on  $R_{VIO}$ .

Figure 4.2 shows the decreasing dependence of  $R_{VIO}$  on the radiation frequency  $\omega$  (for *pulsed* and *CW* sources). Frequency increase also leads to a shift of the characteristic saturation intensity to higher intensity values. Frequency dependence

of photoresponse in the linear region originates from device properties and antenna coupling [6, 24, 97].  $R_{VI0}$  for the linear region can be written as:

$$R_{VI0}(\omega) = R_{VI0}(\omega_0) \left( \frac{\omega_0}{\omega} \right)^\gamma, \quad (4.2)$$

where  $\omega$  is the frequency of incoming radiation,  $\gamma$  is the power of matching.

The influence of FETs parameters and antenna-detector matching on responsivity for low input powers has been analyzed in Ref. [97]. In that work, it was assumed that power  $\gamma=2$  for matching with lenses and/or wide aperture antennas and  $\gamma=4$  for other cases.

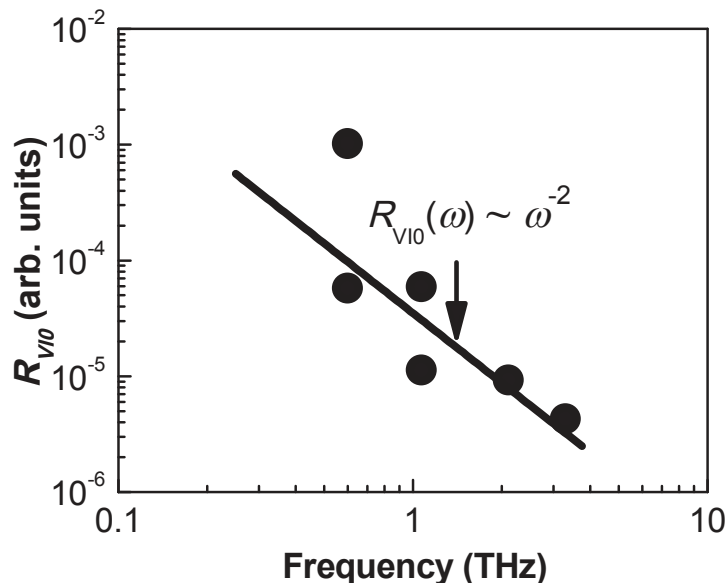


Fig. 4.5 Responsivity  $R_{VI0}$  as a function of a radiation frequency in the linear region for pulsed detection measurement for HEMT. Dots are experimental data of FET detectors (sample HEMT) at  $\mathfrak{F}_{ir} = 10 \text{ W/cm}^2$  (after Fig. 4.2). Line is fitting of Eq.(4.2) with  $\gamma=2$ . (after [83])

Figure 4.5 shows the frequency dependence of  $R_{VI0}$ . Measurement data were obtained in the linear region of detector response of pulsed lasers experiments at  $10 \text{ W/cm}^2$  (after Fig. 4.2). The line shows calculations according to Eq. (4.2) with  $\gamma=2$ . This fitting shows close agreement with the responsivity behavior which was proposed in Ref.[97] and verifies experimentally that indeed for matching with lenses and/or wide aperture antennas  $\gamma=2$ . This result is also close to the experimental data behavior obtained in Ref.[94].

### 4.3 Summary

This chapter demonstrates that a photoresponse can be linear with respect to a radiation intensity in a wide range of intensities, up to several kW/cm<sup>2</sup>. In all cases, we observed that the linear region is followed by the nonlinear part and saturation. The observed photoresponse nonlinearity is explained by nonlinearity and saturation of the transistor channel current. Along the way, we have obtained a result that confirmed the assumption about the coefficient of frequency dependence of responsivity for broadband detection by THz FET detector in linear region at frequency range from 1 THz to 3.3 THz ( $\gamma = 2$  or  $\sim \omega^{-4}$ ). This result is an estimate of the lower threshold of responsivity and can be improved by the use of a narrow-band antenna for the specific frequency band. Experimental data were successfully interpreted in the frame of the extended model of THz FET detection. Both experiments data and theoretical model show that dynamic range of field effect transistors based terahertz detectors extends over many orders of magnitude of intensity of incoming THz radiation.

## CONCLUSION AND FUTURE WORK

This thesis is devoted to study of terahertz detectors based on field-effect transistors. Emphasis was placed on the transistors fabricated on low-cost silicon CMOS technology. However, part of the work was also devoted to studies of transistors that were fabricated in III-V technology.

In this research, we were the first to investigate the photoresponse of field effect transistors to THz radiation in a extremely wide range of intensities: from  $0.5 \text{ mW/cm}^2$  up to  $500 \text{ kW/cm}^2$  and for frequencies from 0.13 THz to 3.3 THz. THz FETs detectors demonstrated linear photoresponse with respect to radiation intensity in a wide range of intensities, up to several  $\text{kW/cm}^2$ . For higher intensities, in all cases, we observed that the linear region is followed by the nonlinear and saturation regions. This experimental observation has led to the development of the new theoretical model of THz FET based detectors.

The new extend model of broadband field-effect transistor detectors is based on the phenomenological knowledge of the transistor static transfer characteristic. The model takes into account the nonlinear behaviour of the channel current in a whole transistor operating range and explains consistently experimental data both in linear and nonlinear regions of terahertz detection. Although the model uses of the MOSFET approach, it can be easily generalized to describe also THz detection by III-V HEMT's.

Future works and some suggestions of possible improvements are given in Appendixes

# **Appendix A**

## **TEMPERATURE DEPENDENCE OF TERAHERTZ PHOTORESPONSE**

Temperature is one of the main parameters that influence transistor characteristics. A temperature modifies transistor transfer characteristics, this factor need to take into account at a detector design process. For example, cooling of FETs can improve characteristics: increase the slope of the transfer characteristics, reduction of the current noise. [105, 106]. The nitrogen or lower temperatures increase photoresponse value by several times, as reported in the Ref. [55, 99].

Photoresponse behaviours from room temperatures down to 4.5 K was studied systematically in Ref. [84] and represent in Sec. A.1. Section A.2 presents the photoresponse behaviours for temperatures higher than 300 K at 1.07 THz. This part of the work, as a possible influence of high intensity THz radiation onto detectors, was studied in Ref.[83].

### **A.1 Low Temperature Measurements**

The broadband THz photoresponse of different GaInAs/GaAs, GaN/AlGaIn HEMT and Si MOSFETs in temperature range from 4 K to 300 K was studied in Ref. [84]. A 292 GHz *CW* electronic source for detection measurements was used (see Sec. 2.6.1). The studied transistor was placed into a liquid helium cooled continuous flow cryostat (see Sec. 2.5) allowing setting any sample temperature between 5 K and 300 K with  $\sim 0.1$  K precision. The four parabolic mirrors based optical system was used to focus the incident radiation to  $\sim 4$  mm diameter of the spot. The system enabled also precise adjustment of the spot position, the way to provide maximal asymmetry of the transistor channel excitation (between the source side and the drain side) and hence leading to a maximal photoresponse signal. The incident radiation was modulated by a chopper, and the photoresponse was measured by a lock-in technique. Examples of photoresponse shapes as a

function of the gate voltage at different temperature are shown in Fig.A.1(a) and Fig.A.1(b) for InGaAs HEMT and Si-MOSFET, respectively.

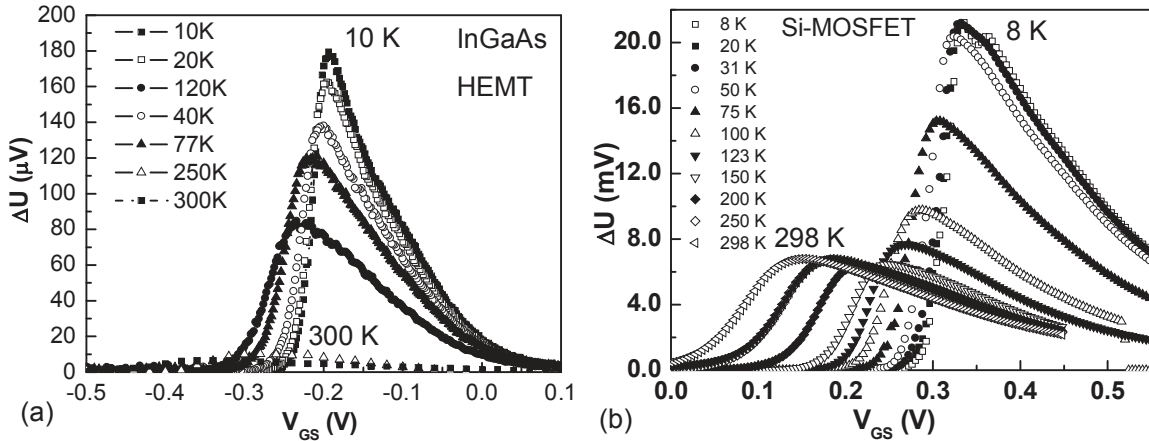


Fig. A.1 Photoresponse as a function of gate voltage at different temperatures. a) InGaAs HEMT, b) Si-MOSFET.

Our results clearly after Ref. [84] show that THz detectors based on GaAs, GaN, or Si field effect transistors can be improved by lowering temperature down. However, the photoresponse values were saturated at temperature lower than nitrogen temperature as shown in Fig. A.2.

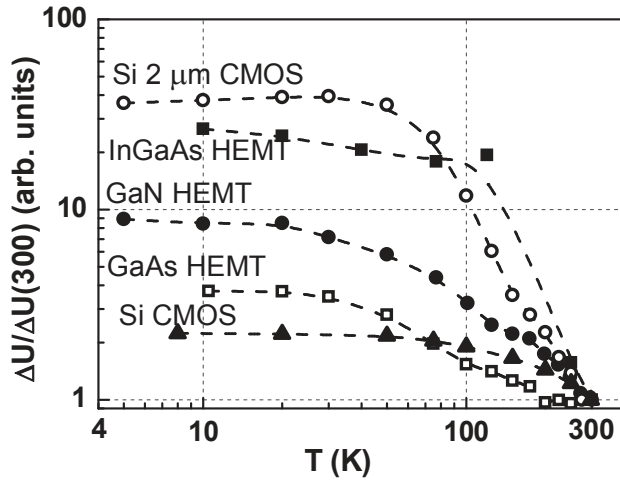


Fig. A.2 Evaluation of the maximal photoresponse value with the temperature for all studied transistors (after [84] with additional curves: Si 0.35 MOSFET and InGaAs HEMT).

Photoresponse at different temperatures (see Fig. A.1) was analyzed using a recent theoretical model (see Sec. 3.3) and it was shown that the shape of the photoresponse as a function of the gate voltage is defined by the transfer

characteristics at all temperatures down to 5 K [83, 95]. The mechanism of this saturation does not perfectly clear and stays open. However, the practical significance of this work lies in the fact that the cooling of detectors to nitrogen temperatures or lower makes sense only for reducing of a noise of readout electronics.

## A.2 Temperature above 300 K

The high-intensity radiation can result in carriers heating and heating of the transistor itself. Here we consider the photoresponse behavior for temperatures higher than 300 K. A 1.07 THz pulsed source for detection measurements was used (see Sec. 2.6.2) at radiation intensity below 1 kW/cm<sup>2</sup>.

In strong-inversion regime (see section 3.1), the channel mobility in FET devices can be written as [92]:

$$\mu_n(T) = \mu_n(T_r) \left( \frac{T}{T_r} \right)^{-k_\mu}, \quad (\text{A.1})$$

where  $T_r$  is the temperature at which parameters were extracted and  $k_\mu$  is the constant temperature coefficient, which varies between 1.2 and 2 [92, 107].

The threshold voltage decreases linearly with temperature [92, 108]

$$V_{th}(T) = V_{th}(T_r) - k_{th}(T - T_r), \quad (\text{A.2})$$

where,  $k_{th}$  for Si-MOSFET is between 0.5 and 3 mV/K [92], for HEMT device  $k_{th}$  is smaller for e.g. 0.3 mV/K [109]. Results of fitting in the frame of the extended broadband model (Eq. (A.1) and Eq. (A.2)) are presented in Fig. A.3. One can see good agreement between calculations and experimental data.

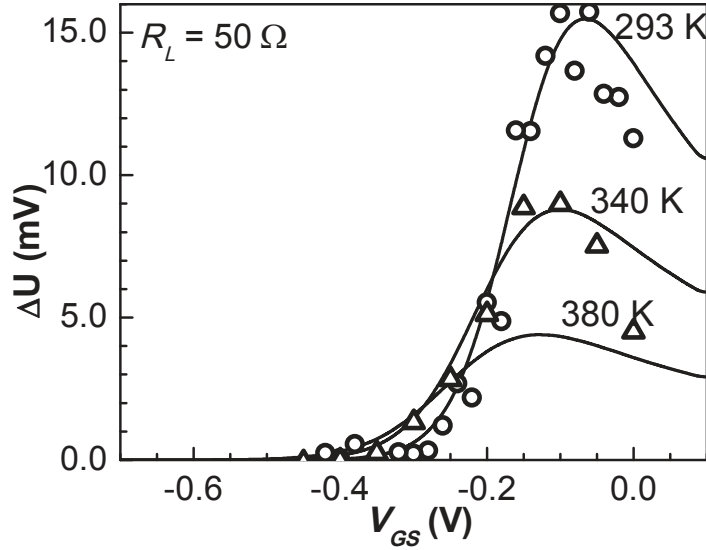


Fig. A.3 Comparison of HEMT ( $W = 22 \mu\text{m}$ ) photoresponses vs gate bias at different temperatures in linear region at frequency 1.07 THz ( $169 \text{ W/cm}^2$ ): circles and triangles are experimental data at  $T = 293 \text{ K}$  and  $T = 340 \text{ K}$ , respectively; solid lines show fitting results using Eq. (4.29) and taking into account the temperature parameters  $k_{th}$ ,  $k_{\mu}$  (see Table 2.3). (after [83])

Figure A.3 shows photoresponse as a function of gate voltage and decreasing response due to temperature  $T$  increase for HEMT ( $W = 24 \mu\text{m}$ ) in the linear region of photoresponse. Solid lines in Fig. 4(b) present  $\Delta U$  fitting using the model from Eq. (4.29), taking into account heating of samples (Eq. (A.1) and Eq. (A.2)). The maximum photoresponse shifts to more negative gate voltage ( $V_{GS,max} = -0.19 \text{ V}$  at  $T = 293 \text{ K}$  and  $V_{GS,max} = -0.225 \text{ V}$  at  $T = 340 \text{ K}$ ) with increasing temperature, and the shape becomes flatter with the maximum value decreasing with temperature rise.

### A.3 Summary

The appendix presents studies of broadband THz detection by different GaInAs/GaAs, GaN/AlGaN, and Si FETs in temperature range 5–380 K. We have analyzed the results using a theoretical model and shown that the shape of the photoresponse on the gate voltage dependence is defined by the transfer characteristics at all temperatures. The photoresponse increased by about one order of magnitude with decreasing of the transistor temperature. For lower temperatures, the photoresponse value was saturated, probably due to the change of the dominant electron transport mechanism. Our results clearly show that THz detectors based on GaAs, GaN, InGaAs or Si field effect transistors can be improved by lowering temperature. They also show that below nitrogen temperature the further improvement is hindered by the physics of the detection process itself. For the case of a temperature above 300K we proposed to take into account temperature dependence of transistor parameters that made it possible to fit the experimental results of the THz FET detection.

## Appendix B

# UTILIZATION OF TERAHERTZ FIELD EFFECT TRANSISTOR DETECTORS

Beyond the sensitivity and other characterizations described before, samples of field effect transistor are tested in real imaging and communication applications. This section demonstrates performances of detectors in these applications

### B.1 Imaging Setup

Detectors based on FETs can be used in THz imaging and spectroscopy systems, as evidenced by the growing number of research papers [30, 110, 111]. Nowadays, THz FET detectors do not exhibit the required sensitivity for passive imaging systems at room temperature. That is due to the *NEP* levels of the detectors that are not low enough to detect the natural radiation of objects at ambient temperature [97]. Therefore, we are dealing with “active imaging/vision” requiring active illumination of the test objects by one or many THz sources as described in Section. 2.6. As opposed to passive vision techniques, active imaging could be conveyed either in “reflection mode”, where the THz signals reflected by an object-under-test are detected by the THz-detectors, or in transmission mode”, where the THz-radiation that pass through an object-under-test are detected. [1, 112].

Imaging by single-pixel systems is probably the easiest and most straightforward (direct) in terms of system complexity. Figure B.1 shows the basic optical and electrical setups for single-pixel scanned-imaging in transmission-mode. The main electrical components are a THz source, a THz detector, an AM modulator and a data acquisitions and processing computer system. An example of a terahertz source is the Schottky diode based multiplier chains provided by Radiometer Physics GmbH (see Sec. 2.6.1). The typical total radiated power is in the range of 4-5 mW for narrow-band source at frequency 292 GHz. The diagonal horn is fed by waveguides and normally delivers nice Gaussian beams.

The THz source is fixed at one end of the setup and is used to illuminate the object in free-space. The detector should be aligned with the source, and both source/detector antennas should be aligned properly along the boresight for maximum radiation coupling (including antenna polarization). Accordingly, imaging system requires the proper source/object/detector alignment that produces the best images possible. The radiation from the THz-source should be guided properly towards the imaging-plane. Then the radiation is projected onto the detectors' collecting aperture with the highest optical and electromagnetic efficiency. The polarization of the sources' and detectors' antennas is needed to be taken into account.

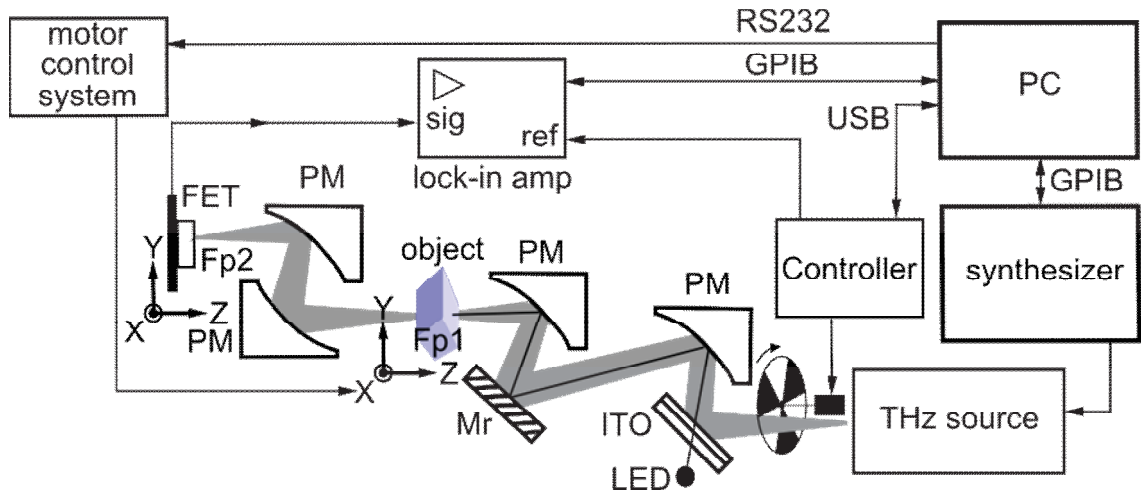


Fig. B.1 Experimental set-up for detector characterization and transmission mode imaging of objects. FET is a THz FET detector, PM is a parabolic mirror, Mr is the mirror, PC is a computer, ITO is the visible transparent mirror. Fp1 and Fp2 are focal points of the system

The THz source creates a diverging Gaussian beam. The parabolic mirrors are used to collect the radiated power and to focus it onto a diffraction limited spot as shown in Figure B.1. This spot is the exact location where the object will be placed to be imaged. The THz-beam diverges from that point on, and another set of mirrors are used to re-collect the radiation and project it on the aperture of the detector antenna. An object is placed at the focal-spot and is scanned by a motorized XY-stage. The focal-spot is the point where the radiated power is

squeezed onto the diffraction limit, and imaging at this spot provides with the highest possible dynamic-range. A miniature LED in combination with an indium tin oxide (ITO) mirror helps with the alignment of the source.

Using a lock-in amplifier technique, the output voltage from the detector is digitized and processed while the object is being scanned in the XY directions. As the output voltage level is proportional to the radiation power level transmitted through the imaged object (linear detection regime), the THz-image will be produced correctly.

For transmission imaging of objects, the detector stays immobile in Fp2, while the object is moved through the focal point Fp1. For responsivity measurements and imaging of the source beam, the detector is moved through the focal point F2 with a motorized XY-translation stage.

The example of the challenging area that is ideally suited for terahertz imaging is the identification of defects or inhomogeneities in different dielectric materials.

An example is shown in Fig B.2. In the figure, one can see a picture of a composite synthetic material. The honeycomb structure is placed between two covering-layers.



Fig. B.2 The photo shows a composite synthetic material, the black square marks a scanning area.

A coating damage could lead to an accumulation of moisture in a cell of the honeycomb structure and to material degradation. Since the air voids in the sample are comparable in size to the terahertz wavelength, they can induce moderate scattering losses when filled with water. This effect could be used as an amplitude contrast mechanism for cell structure control. Thus, THz imaging is an excellent

solution for the damage and moisture presence identification, since water is a good absorber of THz radiation.

The result of the scan in transmission mode is shown in Fig. B.3(a). The scanning was carried out in XY-plane with increments of 100  $\mu\text{m}$ . Water was injected into some of cells of the composite material. The signal level is greatly reduced in the presence of water that is clearly seen in Fig. B.3(b).

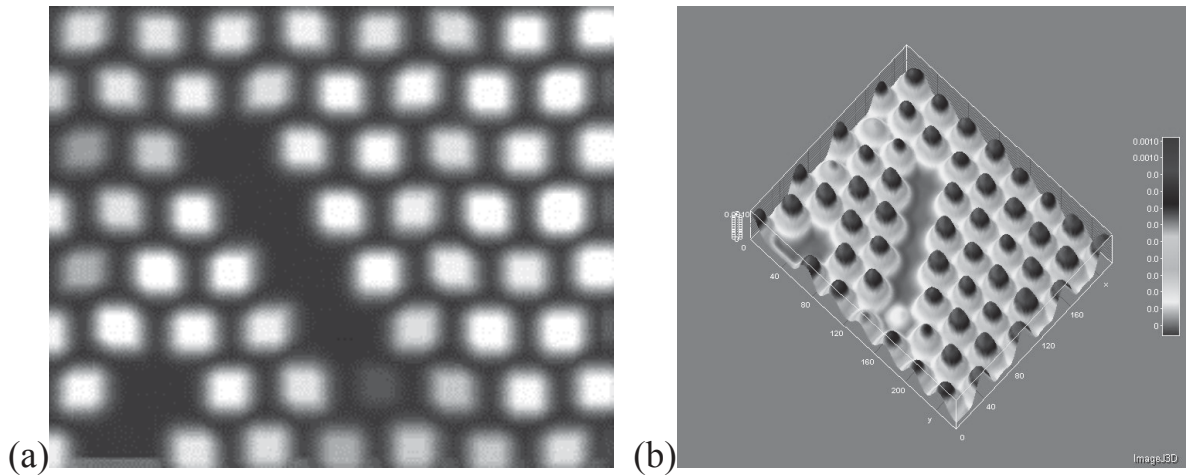


Fig B.3 a) Two-dimensional images obtained using THz radiation in transmission mode; b) Three-dimensional image, where the Z-axis displays the signal level.

As discussed above, the second method of the THz active imaging is a reflection mode. The reflection mode reduces the resolution of the scan, but it allows to investigate surfaces and non-deep defects of thick materials. Since reflection coefficients of the tension zone and homogeneous material are different, the THz radiation can detect stress areas of materials. Fig. B.4 shows the sample of polymer material used in a engineering industry with a designation of a structural defect.

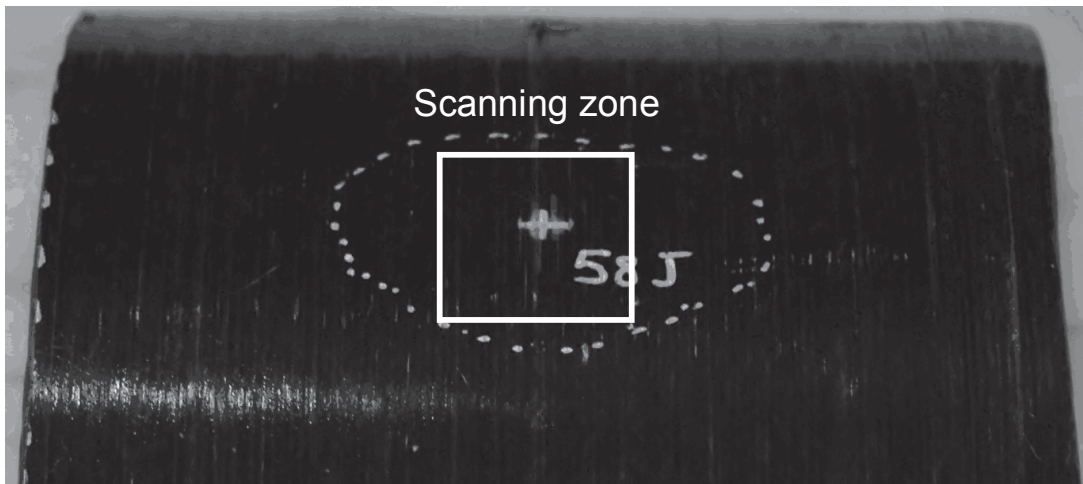


Fig B.4 Picture of a polymer material with the designation of the structural strain.

Image obtained by two-dimensional scanning in reflection mode is shown in Fig. B.5(a). Scanning was carried out with steps of  $300\ \mu\text{m}$ , the scanned area was  $3 \times 3\ \text{cm}$ . The strain region has more high density and a reflection coefficient in this region is much less, as shown in Fig B.3(b).

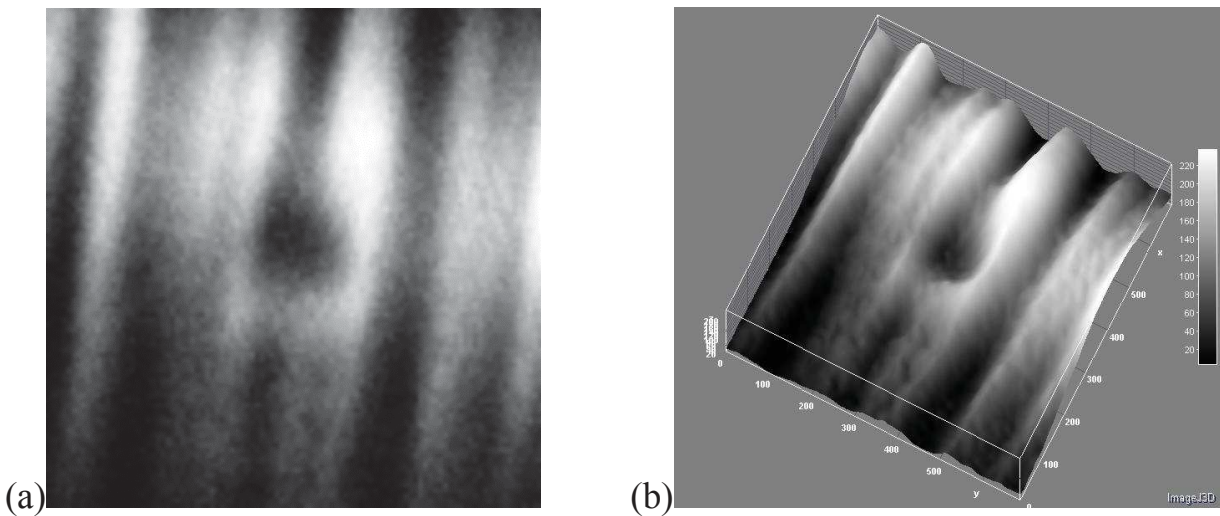


Fig B.5 a) Two-dimensional images obtained by using THz radiation in a reflection mode. b) The image shows the total terahertz power at each pixel (the Z-axis) as a function of the two-dimension positions.

The aim of this chapter was to give an idea on how the THz detectors discussed in the previous chapters can be utilized to produce THz images and characterize integrity and homogeneity of polymer materials. Thus, the chapter has presented techniques that were used in our laboratory for single pixel raster-scanned imaging.

## B.2 Communication setup

Due to continuous increase in the demand of the fast transmission, there is an urgent need in high data rate communication systems. There are two possible ways in which the data rate can be enhanced. First, by increasing the bandwidth of the communication system but the system is inherited with the narrow bandwidth and in most of the cases the device bandwidth is only about 10% of its operating frequency. The next solution to this problem is to increase the operating frequency to such an extent that even with a narrow bandwidth communication systems may fetch a high data rate to the customers. The best solution to this problem would be to move the operating frequency to the terahertz band. However, with an increase in the operating frequency, the device characteristic also changes, and there is a need in the analysis of the various THz wireless communication system components [3, 113].

Recently, in Ref. [114], an application of a Schottky diode for data transfer at 0.3 THz was demonstrated. Detectors based on field-effect transistors also allow to implement such communication systems, as demonstrated in the Refs [115, 116].

As noted previously, THz FET detectors show fast response time (below 1 ns (Ref. [32, 101]) and 30 ps (Ref. [33])).

Figure B.6 shows a comparison of detector response times. One of them is based on FET (Si MOSFET, see Sec. 2.1.1), another is a calibrated photon drag detector which response time is 1 ns [90] at the frequency 0.6 THz (gas laser, see Sec. 2.6.2). It is clear seen that the FET detector completely reproduces the signal profile which is obtained by using the calibrated detector.

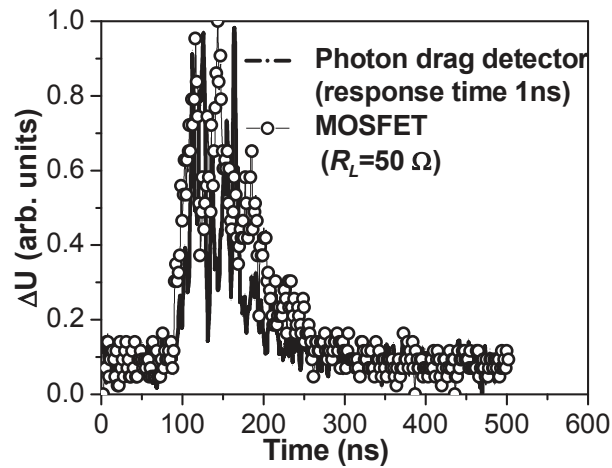


Fig B.6 Comparison of the signal shapes of detectors at radiation frequency of 0.6 THz. Dots are a photoresponse of the THz FET detector and Line is a signal of the photon drag detector.

Figure. B.7 shows response of THz detector (InGaAs HEMT, see Sec. 2.2) to  $\sim 120$  ps pulse at frequency 1.5 THz which was provided by RIKEN high-power tunable THz-wave parametric generator (RIKEN high-power tunable THz-wave parametric generator)[117]. Typical pulse width of THz wave was less than 120 ps. However, the experimental setup imposes restrictions on the possibility to measure pulse signals.

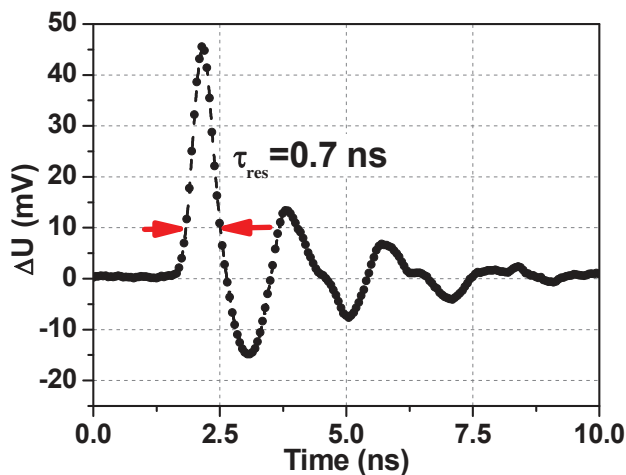


Fig. B.7 THz FET (InGaAs HEMT) photoresponse waveform at 1.5 THz (pulse time < 120 ps).

The THz photoresponse time is  $\tau_{\text{res}} = 0.7$  ns (3 dB fall/rise time  $\tau_{3\text{dB}} = 0.35$  ns). The radiation pulse duration is shorter than the oscilloscope rise time. Capacity of

the  $RC$  delay line is 14 pF (at  $R_L=50 \Omega$ ) and is comparable to the oscilloscope specification capacitance  $12 \pm 2$  pF. If the oscilloscope has time constant more than pulse time, it can measure only the integrated signal. Figure B.7 shows the THz FET signal and a smaller echo of the THz response with opposite sign. This echo is due to a radio frequency signal reflection from the coaxial connection of the oscilloscope to the FETs wiring. This feature varies from sample to sample and depends on matching transmission line and internal parameters of FETs.

Besides quite well-known methods for measuring quality of transmitted analog signals using oscillograms, spectral analysis, etc. The digital telecommunication systems are very often characterized by eye pattern. In telecommunication, an eye pattern, also known as an eye-diagram, is an oscilloscope display in which a digital data from a receiver are repetitively sampled and feed to the vertical input, while the data rate is used to trigger the horizontal sweep. These diagrams are used for an analysis of simple binary digital signals and complex signals of modern digital telecommunication systems like modulated signals of RF transmission systems [118].

The experimental setup is presented in figure B.8. THz communication setup uses the THz FET detector based on GaAs HEMT, and pseudo-random bit sequence (PRBS).

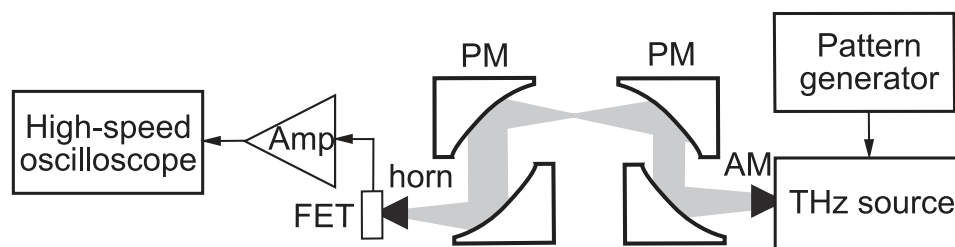


Fig B.8 Experimental set-up for eye-pattern analysis. The 0.2 THz electronic source is modulated (amplitude modulation (AM)) by a PRBS pattern generator. PM is the parabolic mirror, Amp is the amplifier (after [116])

The amplitude of 0.2 THz electronic source is modulated using a PRBS pattern generator. The radiation beam after propagation of 20 cm is collimated and focused by off-axis parabolic mirrors and detected by the FET detector with a horn.

The total output source power is around 2 mW (measured with calibrated pyroelectric sensor, see Sec. 2.6.1). The detected photoresponse is amplified and observed on a high-speed oscilloscope. The amplifier with 200 MHz bandwidth, 40 dB gain and  $50 \Omega$ , was used in the system.

Data transmitted at different data-rate frequencies are shown in Fig. B.9. Fig B.9(c) shows that the increase of transfer speed pseudorandom sequence of bits up to 1.5 Gb/s (Gbps) (which corresponds to 18 GHz) increases noise. The gaps of diagram start to close.

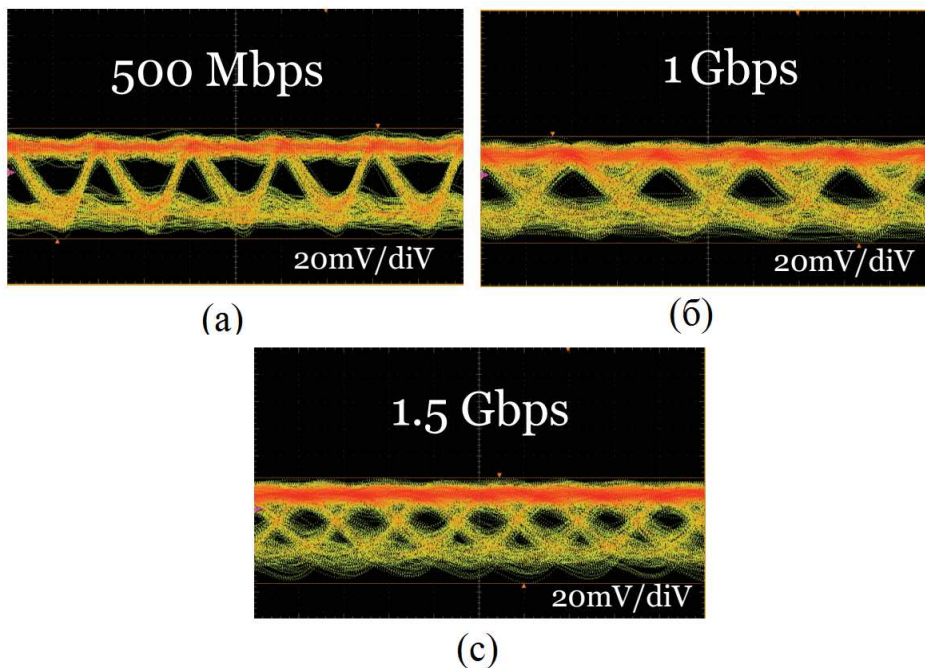


Fig B.9 Wide and high eye openings for three different data-rate frequencies of pseudo-random bit sequence: (a) 500 Mbps. (b) 1 Gbps. (c) 1.5 Gbps. (after [116])

The possibility of using FETs detectors in communication systems at a frequency of 0.324 THz with a bandwidth of over 10 GHz was experimentally demonstrated in Ref. [116]. However, the use of FETs detectors in wireless communication systems requires the development of integrated amplifier for noise reducing and improvement of responsivity and the development of special bandwidth integrated antennas.

## BIBLIOGRAPHY

- [1] A. Rogalski and F. Sizov, "Terahertz detectors and focal plane arrays," *Opto-Electronics Review*, vol. 19, pp. 346-404, 2011.
- [2] D. L. Woolard, E. R. Brown, M. Pepper, and M. Kemp, "Terahertz Frequency Sensing and Imaging: A Time of Reckoning Future Applications? ", *Proceedings of the IEEE*, vol. 93, pp. 1722-1743, 2005.
- [3] K. R. Jha and G. Singh, "Terahertz planar antennas for future wireless communication: A technical review," *Infrared Physics & Technology*, vol. 60, pp. 71-80, 2013.
- [4] J. Federici and L. Moeller, "Review of terahertz and subterahertz wireless communications," *Journal of Applied Physics*, vol. 107, p. 111101, 2010.
- [5] A. Rogalski, *Infrared detectors*: CRC Press, 2010.
- [6] A. J. M. Kreisler, "Submillimeter Wave Applications Of Submicron Schottky Diodes", in *Proc. SPIE 0666, Far-Infrared Science and Technology*, Quebec, Canada pp. 51-63, 1986
- [7] S. Cibella, R. Casini, A. Di Gaspare, and M. Ortolani, "Air bridge improves terahertz detector response time", *Laser Focus World*, vol. 47, pp. 51-55, 2011.
- [8] F. Friederich, W. Von Spiegel, M. Bauer, F. Meng, M. D. Thomson, S. Boppel, A. Lisauskas, B. Hils, V. Krozer, and A. Keil, "THz active imaging systems with real-time capabilities", *Terahertz Science and Technology, IEEE*, vol. 1, pp. 183-200, 2011. DOI: 10.1109/TTHZ.2011.2159559
- [9] R. Han, Y. Zhang, D. Coquillat, H. Videlier, W. Knap, E. Brown, and K. K. O, "A 280-GHz Schottky Diode Detector in 130-nm Digital CMOS", *IEEE Journal of Solid-State Circuits*, vol. 46, pp. 2602-2612, 2011.
- [10] A. Rogalski, "HgCdTe infrared detector material: history, status and outlook", *Reports on Progress in Physics*, vol. 68, p. 2267, 2005.
- [11] J.-H. Dai, J.-H. Lee, Y.-L. Lin, and S.-C. Lee, "In(Ga)As quantum rings for terahertz detectors," *Japanese Journal of Applied Physics*, vol. 47, pp. 2924, 2008.
- [12] S. Bhowmick, G. Huang, W. Guo, C. S. Lee, P. Bhattacharya, G. Ariyawansa, and A. G. U. Perera, " High-performance quantum ring detector for the 1–3 terahertz range", *Applied Physics Letters*, vol. 96, pp. 231103, 2010.
- [13] Y. Kawano, T. Fuse, S. Toyokawa, T. Uchida, and K. Ishibashi, "Terahertz photon-assisted tunneling in carbon nanotube quantum dots", *Journal of Applied Physics*, vol. 103, pp. 034307, 2008.
- [14] E. N. Grossman and A. J. Miller, "Active millimeter-wave imaging for concealed weapons detection," in *SPIE AeroSense 2003 symposium*, Orlando, United States, pp. 62-70, 2003.
- [15] I. Kasalynas, A. J. Adam, T. O. Klaassen, J. N. Hovenier, G. Pandraud, V. P. Iordanov, and P. M. Sarro, "Design and performance of a room-temperature terahertz detection array for real-time imaging", *IEEE Journal of Selected Topics in Quantum Electronics*, vol. 14, pp. 363-369, 2008.
- [16] A. W. Lee, B. S. Williams, S. Kumar, Q. Hu, and J. L. Reno, "Real-time imaging using a 4.3-THz quantum cascade laser and a 320/spl times/240

- microbolometer focal-plane array", *Photonics Technology Letters, IEEE*, vol. 18, pp. 1415-1417, 2006.
- [17] L. Liu, J. L. Hesler, H. Xu, A. W. Lichtenberger, and R. M. Weikle, "A broadband quasi-optical terahertz detector utilizing a zero bias Schottky diode," *Microwave and Wireless Components Letters, IEEE*, vol. 20, pp. 504-506, 2010.
- [18] E. R. Brown, A. C. Young, J. Zimmerman, H. Kazemi, and A. C. Gossard, "Advances in Schottky rectifier performance", *Microwave Magazine, IEEE*, vol. 8, pp. 54-59, 2007.
- [19] A. Semenov, O. Cojocari, H.-W. Hubers, F. Song, A. Klushin, and A.-S. Muller, "Application of zero-bias quasi-optical Schottky-diode detectors for monitoring short-pulse and weak terahertz radiation", *Electron Device Letters, IEEE*, vol. 31, pp. 674-676, 2010.
- [20] F. Schuster, D. Coquillat, H. Videlier, M. Sakowicz, F. Teppe, L. Dussopt, B. Giffard, T. Skotnicki, and W. Knap, "Broadband terahertz imaging with highly sensitive silicon CMOS detectors", *Opt. Express*, vol. 19, pp. 7827-7832, Apr 11 2011.
- [21] R. Al Hadi, H. Sherry, J. Grzyb, N. Baktash, Y. Zhao, E. Ojefors, A. Kaiser, A. Cathelin, and U. Pfeiffer, "A broadband 0.6 to 1 THz CMOS imaging detector with an integrated lens," in *Microwave Symposium Digest (MTT), 2011 IEEE MTT-S International*, pp. 1-4, 2011
- [22] E. Ojefors, U. R. Pfeiffer, A. Lisauskas, and H. G. Roskos, "A 0.65 THz Focal-Plane Array in a Quarter-Micron CMOS Process Technology", *IEEE Journal of Solid-State Circuits*, vol. 44, pp. 1968-1976, 2009.
- [23] A. Pleteršek and J. Trontelj, "A Self-Mixing NMOS Channel-Detector Optimized for mm-Wave and THz Signals", *Journal of Infrared, Millimeter, and Terahertz Waves*, vol. 33, pp. 615-626, 2012.
- [24] S. Boppel, A. Lisauskas, M. Mundt, D. Seliuta, L. Minkevicius, I. Kasalynas, G. Valusis, M. Mittendorff, S. Winnerl, V. Krozer, and H. G. Roskos, "CMOS Integrated Antenna-Coupled Field-Effect Transistors for the Detection of Radiation From 0.2 to 4.3 THz," *Microwave Theory and Techniques, IEEE Transactions on*, vol. 60, pp. 3834-3843, 2012.
- [25] F. Sizov, V. Petriakov, V. Zabudsky, D. Krasilnikov, M. Smolij, and S. Dvoretzki, "Millimeter-wave hybrid un-cooled narrow-gap hot-carrier and Schottky diodes direct detectors", *Applied Physics Letters*, vol. 101, p. 082108, 2012.
- [26] M. Dyakonov and M. Shur, "Shallow water analogy for a ballistic field effect transistor: New mechanism of plasma wave generation by dc current", *Physical Review Letters*, vol. 71, p. 2465, 1993.
- [27] W. Knap, Y. Deng, S. Romyantsev, and M. S. Shur, "Resonant detection of subterahertz and terahertz radiation by plasma waves in submicron field-effect transistors", *Applied Physics Letters*, vol. 81, pp. 4637-4639, 2002.
- [28] S. Boubanga-Tombet, F. Teppe, D. Coquillat, S. Nadar, N. Dyakonova, H. Videlier, W. Knap, A. Shchepetov, C. Gardes, Y. Roelens, S. Bollaert, D. Seliuta, R. Vadoklis, and G. Valusis, "Current driven resonant plasma wave

- detection of terahertz radiation: Toward the Dyakonov-Shur instability", *Applied Physics Letters*, vol. 92, pp. 212101-3, 2008.
- [29] M. I. Dyakonov, "Generation and detection of Terahertz radiation by field effect transistors", *Comptes Rendus Physique*, vol. 11, pp. 413-420, 2010.
- [30] A. Lisauskas, U. Pfeiffer, E. Ojefors, P. H. Bolivar, D. Glaab, and H. G. Roskos, "Rational design of high-responsivity detectors of terahertz radiation based on distributed self-mixing in silicon field-effect transistors," *Journal of Applied Physics*, vol. 105, pp. 114511-7, 2009.
- [31] D. Perenzoni, M. Perenzoni, L. Gonzo, A. D. Capobianco, and F. Sacchetto, "Analysis and design of a CMOS-based terahertz sensor and readout," in *Optical Sensing and Detection*, Brussels, Belgium, pp. 772618-12, 2010.
- [32] C. Drexler, N. Dyakonova, P. Olbrich, J. Karch, M. Schafberger, K. Karpierz, Y. Mityagin, M. B. Lifshits, F. Teppe, O. Klimenko, Y. M. Meziani, W. Knap, and S. D. Ganichev, "Helicity sensitive terahertz radiation detection by field effect transistors," *Journal of Applied Physics*, vol. 111, pp. 124504-6, 2012.
- [33] S. Preu, M. Mittendorff, S. Winnerl, H. Lu, A. C. Gossard, and H. B. Weber, "Ultra-fast transistor-based detectors for precise timing of near infrared and THz signals," *Optics Express*, vol. 21, pp. 17941-17950, 2013/07/29 2013.
- [34] K. S. Romanov and M. I. Dyakonov, "Theory of helicity-sensitive terahertz radiation detection by field effect transistors," *Applied Physics Letters*, vol. 102, p. 153502, 2013.
- [35] W. Knap, F. Teppe, Y. Meziani, N. Dyakonova, J. Lusakowski, F. Boeuf, T. Skotnicki, D. Maude, S. Romyantsev, and M. S. Shur, "Plasma wave detection of sub-terahertz and terahertz radiation by silicon field-effect transistors," *Applied Physics Letters*, vol. 85, pp. 675-677, 2004.
- [36] R. Tauk, F. Teppe, S. Boubanga, D. Coquillat, W. Knap, Y. M. Meziani, C. Gallon, F. Boeuf, T. Skotnicki, C. Fenouillet-Beranger, D. K. Maude, S. Romyantsev, and M. S. Shur, "Plasma wave detection of terahertz radiation by silicon field effects transistors: Responsivity and noise equivalent power," *Applied Physics Letters*, vol. 89, pp. 253511-3, 2006.
- [37] A. Lisauskas, D. Glaab, H. G. Roskos, E. Ojefors, and U. R. Pfeiffer, "Terahertz imaging with Si MOSFET focal-plane arrays," in *Proc. SPIE 7215, International Society for Optics and Photonics*, San Jose, United State, pp. 72150J-11, 2009.  
DOI: 10.1117/12.809552
- [38] S. Boppel, A. Lisauskas, V. Krozer, and H. G. Roskos, "Performance and performance variations of sub-1 THz detectors fabricated with 0.15  $\mu\text{m}$  CMOS foundry process," *Electronics Letters*, vol. 47, p. 661, 2011.
- [39] H. Sherry, J. Grzyb, Z. Yan, R. Al Hadi, A. Cathelin, A. Kaiser, and U. Pfeiffer, "A 1kpixel CMOS camera chip for 25fps real-time terahertz imaging applications," in *IEEE International Solid-State Circuits Conference Digest of Technical Papers (ISSCC 2012)*, pp. 252-254, 2012.
- [40] D. Glaab, S. Boppel, A. Lisauskas, U. Pfeiffer, E. Ojefors, and H. G. Roskos, "Terahertz heterodyne detection with silicon field-effect transistors," *Applied Physics Letters*, vol. 96, pp. 042106-3, 2010.

- [41] M. S. Vitiello, D. Coquillat, L. Viti, D. Ercolani, F. Teppe, A. Pitanti, F. Beltram, L. Sorba, W. Knap, and A. Tredicucci, "Room-Temperature Terahertz Detectors Based on Semiconductor Nanowire Field-Effect Transistors," *Nano Letters*, vol. 12, pp. 96-101, 2011.
- [42] D. Coquillat, N. Dyakonova, M. Goiran, M. S. Vitiello, L. Vicarelli, J. M. Pomirol, W. Escoffier, B. Raquet, D. But, F. Teppe, V. Pellegrini, A. Tredicucci, and W. Knap, "Terahertz rectification by graphene field effect transistors," in *37th International Conference on Infrared, Millimeter, and Terahertz Waves (IRMMW-THz 2012)*, 2012  
DOI: 10.1109/IRMMW-THz.2012.6380119
- [43] V. V. Popov, D. M. Ermolaev, K. V. Maremyanin, N. A. Maleev, V. E. Zemlyakov, V. I. Gavrilenko, and S. Y. Shapoval, "High-responsivity terahertz detection by on-chip InGaAs/GaAs field-effect-transistor array," *Applied Physics Letters*, vol. 98, pp. 153504-3, 2011.
- [44] V. V. Popov, D. V. Fateev, T. Otsuji, Y. M. Meziani, D. Coquillat, and W. Knap, "Plasmonic terahertz detection by a double-grating-gate field-effect transistor structure with an asymmetric unit cell," *Applied Physics Letters*, vol. 99, pp. 243504-243504-4, 2011.
- [45] T. Watanabe, S. B. Tombet, Y. Tanimoto, Y. Wang, H. Minamide, H. Ito, D. Fateev, V. Popov, D. Coquillat, W. Knap, Y. Meziani, and T. Otsuji, "Ultrahigh sensitive plasmonic terahertz detector based on an asymmetric dual-grating gate HEMT structure," *Solid-State Electronics*, vol. 78, pp. 109-114, 2012.
- [46] T. Watanabe, S. A. Boubanga-Tombet, Y. Tanimoto, D. Fateev, V. Popov, D. Coquillat, W. Knap, Y. M. Meziani, W. Yuye, H. Minamide, H. Ito, and T. Otsuji, "InP- and GaAs-Based Plasmonic High-Electron-Mobility Transistors for Room-Temperature Ultrahigh-Sensitive Terahertz Sensing and Imaging," *Sensors Journal, IEEE*, vol. 13, pp. 89-99, 2013.
- [47] A. V. Chaplik, "Possible crystallization of charge carriers in the inversion layer of low density," *Sov. Phys. JETP*, vol. 35, p. 395, 1972.
- [48] M. Nakayama, "Theory of Surface Waves Coupled to Surface Carriers," *Journal of the Physical Society of Japan*, vol. 36, pp. 393-398, 1974 1974.
- [49] A. Eguiluz, T. K. Lee, J. J. Quinn, and K. W. Chiu, "Interface excitations in metal-insulator-semiconductor structures," *Physical Review B*, vol. 11, pp. 4989-4993, 1975.
- [50] M. Dyakonov and M. Shur, "Detection, mixing, and frequency multiplication of terahertz radiation by two-dimensional electronic fluid", *IEEE Transactions on Electron Devices*, vol. 43, pp. 380-387, 1996.
- [51] M. I. Dyakonov and M. S. Shur, "Plasma wave electronics: novel terahertz devices using two dimensional electron fluid", *IEEE Transactions on Electron Devices*, vol. 43, pp. 1640-1645, 1996.
- [52] M. Shur, *Introduction to electronic devices*: J. Wiley, 1996.
- [53] A. Gutin, V. Kachorovskii, A. Muraviev, and M. Shur, "Plasmonic terahertz detector response at high intensities", *Journal of Applied Physics*, vol. 112, pp. 014508-5, 2012.

- [54] F. Schwierz, "The frequency limits of field-effect transistors: MOSFET vs. HEMT," in *9th International Conference on Solid-State and Integrated-Circuit Technology, ICSICT 2008*, pp. 1433-1436, 2008.
- [55] D. B. But and O. G. Golenkov, "Sensitivity of silicon field-effect transistors for radiation of submillimeter range," presented at the Conference of Young Scientists "Lashkaryov's readings 2010", Kiev, Ukraine, 2010.
- [56] A. T. Ping, W. Liebl, G. Mahoney, S. Mahon, and O. Berger, "A High-Performance 0.13- $\mu\text{m}$  AlGaAs/InGaAs pHEMT Process Using Sidewall Spacer Technology", presented at *International Conference on Compound Semiconductor Manufacturing (GaAs MANTECH 2005)*, New Orleans, Louisiana, United State, 2005.
- [57] M. Sakowicz, J. Lusakowski, K. Karpierz, M. Grynberg, W. Knap, and W. Gwarek, "Polarization sensitive detection of 100 GHz radiation by high mobility field-effect transistors," *Journal of Applied Physics*, vol. 104, pp. 024519-5, 2008.
- [58] Y. S. Jin, G. J. Kim, and S. G. Jeon, "Terahertz dielectric properties of polymers", *Journal of the Korean Physical Society*, vol. 49, pp. 513-517, 2006.
- [59] M. C. Teich and B. E. A. Saleh, *Fundamentals of photonics*. Canada: Wiley Interscience, 1991.
- [60] C. A. Balanis, *Antenna theory: analysis and design*, 3rd Edition ed. New Jersey: John Wiley & Sons, 2005.
- [61] A. A. Oliner, D. R. Jackson, and J. Volakis, "Antenna Engineering Handbook", *McGraw Hill*, 2007.
- [62] D. But, O. Golenkov, N. Sakhno, F. Sizov, S. Korinets, J. Gumenjuk-Sichevska, V. Reva, and S. Bunchuk, "Silicon field-effect transistors as radiation detectors for the Sub-THz range", *Semiconductors*, vol. 46, pp. 678-683, 2012.
- [63] D. R. Schmidt, K. W. Lehnert, A. M. Clark, W. D. Duncan, K. D. Irwin, N. Miller, and J. N. Ullom, "A superconductor-insulator-normal metal bolometer with microwave readout suitable for large-format arrays", *Applied Physics Letters*, vol. 86, pp. 053505, 2005.
- [64] D. Rutledge, S. Schwarz, and A. Adams, "Infrared and submillimetre antennas," *Infrared Physics*, vol. 18, pp. 713-729, 1978.
- [65] D. B. Rutledge and M. S. Muha, "Imaging antenna arrays," *IEEE Transactions on Antennas and Propagation*, vol. 30, pp. 535-540, 1982.
- [66] F. Sizov, A. Golenkov, D. But, M. Sakhno, and V. Reva, "Sub-THz radiation room temperature sensitivity of long-channel silicon field effect transistors," *Opto-Electronics Review*, vol. 20, pp. 194-199, 2012.
- [67] W. Knap, F. Schuster, D. Coquillat, F. Teppe, B. Giffard, D. B. But, O. G. Golenkov, and F. F. Sizov, "Terahertz Detectors Based on Silicon Technology Field Effect Transistors", in *MRS Proceedings* vol. 1437, pp. 107-04, 2012.
- [68] D. B. But, N. V. Dyakonova, D. Coquillat, W. Knap, T. Watanabe, Y. Tanimoto, S. Boubanga-Tombet, and T. Otsuji, "Research on THz detectors based with InGaP/InGaAs/GaAs Double -Grating Gate Transistor in high magnetic fields," presented at the Jaszowiec, 41st International School and Conference on Physics of Semiconductors", Krynica-Zdroj, Poland, 2012.

- [69] F. Schuster, W. Knap, and V. Nguyen, "Terahertz imaging achieved with low-cost CMOS detectors," *Laser Focus World*, vol. 47(7), pp. 37–41, 2011.
- [70] M. Sakhno, J. Gumenjuk-Sichevska, and F. Sizov, "Simulated properties of printed antennas on silicon substrates for THz/sub-THz arrays," *Semiconductor Physics, Quantum Electronics & Optoelectronics*, vol. 14, pp. 55-58, 2011.
- [71] K. J. Willis, S. C. Hagness, and I. Knezevic, "A generalized Drude model for doped silicon at terahertz frequencies derived from microscopic transport simulation", *Applied Physics Letters*, vol. 102, pp. 122113, 2013.
- [72] D. M. Hailu, I. A. Ehtezazi, M. Neshat, G. S. A. Shaker, and S. Safavi-Naeini, "Hybrid Spectral-Domain Ray Tracing Method for Fast Analysis of Millimeter-Wave and Terahertz-Integrated Antennas," *IEEE Transactions on Terahertz Science and Technology*, vol. 1, pp. 425-434, 2011.
- [73] B. E. Stine, D. S. Boning, J. E. Chung, L. Camilletti, F. Kruppa, E. R. Equi, W. Loh, S. Prasad, M. Muthukrishnan, D. Towery, M. Berman, and A. Kapoor, "The physical and electrical effects of metal-fill patterning practices for oxide chemical-mechanical polishing processes," *Electron Devices, IEEE Transactions on*, vol. 45, pp. 665-679, 1998.
- [74] C.-L. Chen, "Effects of CMOS process fill patterns on spiral inductors", *Microwave and Optical Technology Letters*, vol. 36, pp. 462-465, 2003.
- [75] Y. Meziani, J. Łusakowski, W. Knap, N. Dyakonova, F. Teppe, K. Romanjek, M. Ferrier, R. Clerc, G. Ghibaudo, and F. Boeuf, "Magnetoresistance characterization of nanometer Si metal-oxide-semiconductor transistors", *Journal of Applied Physics*, vol. 96, pp. 5761-5765, 2004.
- [76] R. A. Valitov and S. F. Dyubko, *Technique submillimeter waves*, Soviet Radio, 1969.  
P. A. Валитов and С. Ф. Дюбко, *Техника субмиллиметровых волн*: Издательство "Советское Радио", 1969.
- [77] D. B. But and O. G. Golenkov, "Current sensivity of Si MOSFET to terahertz irradiation," in *International Kharkov Symposium on Physics and Engineering of Microwaves, Millimeter and Submillimeter Waves (MSMW 2010)*, Kharkiv, Ukraine, 2010. DOI: 10.1109/MSMW.2010.5546073
- [78] F. F. Sizov, O. G. Golenkov, V. P. Reva, and D. B. But, "Electrical parameters of Si n-MOSFET THz-detector: matching with external amplifier," presented at the *International Symposium «Terahertz radiation: Generation and Applications»*, Novosibirsk, Russia, 2010.
- [79] D. B. But, "Registration of radiation of submillimeter spectrum by silicon field-effect transistors," presented at the Conference of Young Scientists "Lashkarovski reading 2011" Kiev, Ukraine, 2011.
- [80] D. B. But, F. F. Sizov, O. G. Golenkov, and V. P. Reva, "Direct detection of the sub-THz incident radiation by silicon field-effect transistors," presented at *3rd International Workshop on THz Radiation: Basic Research and Applications (the TERA 2011)*, Kharkov, Ukraine, 2011.
- [81] Z.-D. Kvon, S. N. Danilov, N. N. Mikhailov, S. A. Dvoretzky, W. Prettl, and S. D. Ganichev, "Cyclotron resonance photoconductivity of a two-dimensional electron gas in HgTe quantum wells," *Physica E: Low-dimensional Systems and Nanostructures*, vol. 40, pp. 1885-1887, 2008.

- [82] S. D. Ganichev and W. Prettl, *Intense Terahertz Excitation of Semiconductors*. UK: OUP Oxford, 2006.
- [83] D. B. But, C. Drexler, M. V. Sakhno, N. Dyakonova, O. Drachenko, F. F. Sizov, A. Gutin, S. D. Ganichev, and W. Knap, "Nonlinear photoresponse of field effect transistors terahertz detectors at high irradiation intensities," *Journal of Applied Physics*, vol. 115, p. 164514, 2014.
- [84] O. A. Klimenko, W. Knap, B. Iniguez, D. Coquillat, Y. A. Mityagin, F. Teppe, N. Dyakonova, H. Videlier, D. But, F. Lime, J. Marczewski, and K. Kucharski, "Temperature enhancement of terahertz responsivity of plasma field effect transistors," *Journal of Applied Physics*, vol. 112, pp. 014506-5, 2012.
- [85] D. But, N. Dyakonova, D. Coquillat, F. Teppe, W. Knap, T. Watanabe, Y. Tanimoto, S. Boubanga Tombet, and T. Otsuji, "THz Double-Grating Gate Transistor Detectors in High Magnetic Fields," *Acta Physica Polonica A*, vol. 122, pp. 1080-1082, December 2012 2012.
- [86] J. Karch, P. Olbrich, M. Schmalzbauer, C. Zoth, C. Brinsteiner, M. Fehrenbacher, U. Wurstbauer, M. Glazov, S. Tarasenko, and E. Ivchenko, "Dynamic Hall effect driven by circularly polarized light in a graphene layer," *Physical Review Letters*, vol. 105, p. 227402, 2010.
- [87] S. D. Ganichev, S. A. Emel'yanov, and I. D. Yaroshetskii, "Spectral sign inversion of photon drag at far-IR wavelengths " *Pisma Zh. Eksp. Teor. Fiz.*, vol. 35, p. 297, 1982.
- [88] S. Ganichev, I. Yassievich, W. Prettl, J. Diener, B. Meyer, and K. Benz, "Tunneling Ionization of Autolocalized DX-Centers in Terahertz Fields," *Physical Review Letters*, vol. 75, p. 1590, 1995.
- [89] W. Seidel, E. Cizmar, O. Drachenko, M. Helm, M. Justus, U. Lehnert, P. Michel, M. Ozerov, H. Schneider, R. Schurig, D. Stehr, M. Wagner, S. Winnerl, D. Wohlfarth, and S. Zvyagin, "Three years of cw-operation at FELBE - Experiences and applications," presented at the *30th International Free Electron Laser Conference (FEL 2008)*, Gyeongju, Korea, 2008.
- [90] S. D. Ganichev, Y. V. Terent'ev, and I. D. Yaroshetskii, "Photon-drag photodetectors for the far-IR and submillimeter regions," *Pisma Zh. Tekh. Fiz.*, vol. 11, 1985.
- [91] E. Ziemann, S. Ganichev, W. Prettl, I. Yassievich, and V. Perel, "Characterization of deep impurities in semiconductors by terahertz tunneling ionization," *Journal of Applied Physics*, vol. 87, pp. 3843-3849, 2000.
- [92] Y. Tsididis and C. McAndrew, *Operation and Modeling of the MOS Transistor* vol. 2: Oxford University Press New York, 1999.
- [93] W. Liu, *MOSFET Models for SPICE Simulation including BSIM3v3 and BSIM4*: Wiley-Interscience Publication, 2001.
- [94] S. Boppel, A. Lisauskas, D. Seliuta, L. Minkevicius, L. Kasalynas, G. Valusis, V. Krozer, and H. Roskos, "CMOS integrated antenna-coupled field-effect-transistors for the detection of 0.2 to 4.3 THz", in *Proc. IEEE Transactions on Microwave Theory and Techniques*, pp. 77-80, 2012.  
DOI: 10.1109/SiRF.2012.6160142
- [95] M. Sakowicz, M. B. Lifshits, O. A. Klimenko, F. Schuster, D. Coquillat, F. Teppe, and W. Knap, "Terahertz responsivity of field effect transistors versus

- their static channel conductivity and loading effects," *Journal of Applied Physics*, vol. 110, pp. 054512-6, 2011.
- [96] W. Stillman, M. S. Shur, D. Veksler, S. Romyantsev, and F. Guarin, "Device loading effects on nonresonant detection of terahertz radiation by silicon MOSFETs," *Electronics Letters*, vol. 43, pp. 422-423, 2007.
- [97] M. Sakhno, F. Sizov, and A. Golenkov, "Uncooled THz/sub-THz Rectifying Detectors: FET vs. SBD", *Journal of Infrared, Millimeter, and Terahertz Waves*, vol. 34, pp. 798-814, 2013.
- [98] M. Sakhno, J. Gumenjuk-Sichevska, D. But, and F. Sizov, "Antenna matching influence on the operation of THz silicon FET with the different channel width," presented at the VI Ukrainian scientific conference on physics of semiconductors (USCPS-6), Chernivtsi, Ukraine, 2013.
- [99] W. Knap, V. Kachorovskii, Y. Deng, S. Romyantsev, J. Q. Lu, R. Gaska, M. S. Shur, G. Simin, X. Hu, M. A. Khan, C. A. Saylor, and L. C. Brunel, "Nonresonant detection of terahertz radiation in field effect transistors," *Journal of Applied Physics*, vol. 91, pp. 9346-9353, 2002.
- [100] S. Preu, H. Lu, M. S. Sherwin, and A. C. Gossard, "Detection of nanosecond-scale, high power THz pulses with a field effect transistor," *Review of Scientific Instruments*, vol. 83, pp. 053101-6, 2012.
- [101] D. B. But, N. Dyakonova, C. Drexler, O. Drachenko, K. Romanov, O. G. Golenkov, F. F. Sizov, A. Gutin, M. S. Shur, S. D. Ganichev, and W. Knap, "The dynamic range of THz broadband FET detectors " in *SPIE Optical Engineering + Applications*., San Diego, United States, pp. 884612-7, 2013
- [102] V. Y. Kachorovskii, S. L. Romyantsev, W. Knap, and M. Shur, "Performance limits for field effect transistors as terahertz detectors," *Applied Physics Letters*, vol. 102, pp. 223505-4, 2013.
- [103] S. Preu, S. Kim, R. Verma, P. G. Burke, M. S. Sherwin, and A. C. Gossard, "An improved model for non-resonant terahertz detection in field-effect transistors," *Journal of Applied Physics*, vol. 111, pp. 024502-9, 2012.
- [104] D. B. But, O. Drachenko, N. Dyakonova, D. Coquillat, K. Romanov, O. G. Golenkov, F. F. Sizov, A. Gutin, M. Shur, C. Drexler, S. D. Ganichev, and W. Knap, "Nonlinear Terahertz Photoresponse of Field Effect Transistors," presented at the *International Workshop on Optical Terahertz Science and Technology 2013 (OTST 2013)*, Kyoto, Japan, 2013.
- [105] E. A. Gutierrez-D, J. Deen, and C. Claeys, *Low temperature electronics: physics, devices, circuits, and applications*: Academic Press, 2000.
- [106] E. Simoen, C. Claeys, and J. A. Martino, "Parameter extraction of MOSFETs operated at low temperature", *Le Journal de Physique IV*, vol. 6, pp. C3-29-C3-42, 1996.
- [107] S. Vitanov, V. Palankovski, S. Maroldt, and R. Quay, "High-temperature modeling of AlGaIn/GaN HEMTs," *Solid-State Electronics*, vol. 54, pp. 1105-1112, 2010.
- [108] S. M. Sze and K. K. Ng, *Physics of Semiconductor Devices*: John Wiley & Sons, 2006.

- [109] M. Ni, P. Fay, and N. Pan, "Temperature Dependence of InGaP/InGaAs/GaAs pHEMTs," presented at the CS MANTECH Conference, Vancouver, British Columbia, Canada, 2006.
- [110] B. Hu and M. Nuss, "Imaging with terahertz waves," *Opt. Lett.*, vol. 20, pp. 1716-1718, 1995.
- [111] N. C. Van der Valk, W. A. van der Marel, and P. Planken, "Terahertz polarization imaging," *Opt Lett*, vol. 30, pp. 2802-2804, 2005.
- [112] W. L. Chan, J. Deibel, and D. M. Mittleman, "Imaging with terahertz radiation," *Reports on Progress in Physics*, vol. 70, p. 1325, 2007.
- [113] S. Ho-Jin and T. Nagatsuma, "Present and Future of Terahertz Communications", *IEEE Transactions on Terahertz Science and Technology*, vol. 1, pp. 256-263, 2011. DOI: 10.1109/TTHZ.2011.2159552
- [114] C. Jastrow, K. Münter, R. Piesiewicz, T. Kürner, M. Koch, and T. Kleine-Ostmann, "300 GHz transmission system," *Electronics Letters*, vol. 44, pp. 213-214, 2008.
- [115] S. Blin, F. Teppe, L. Tohme, S. Hisatake, K. Arakawa, P. Nouvel, D. Coquillat, A. Penarier, J. Torres, L. Varani, W. Knap, and T. Nagatsuma, "Plasma-Wave Detectors for Terahertz Wireless Communication," *IEEE Electron Device Letters*, vol. 33, pp. 1354-1356, 2012.
- [116] L. Tohme, S. Blin, P. Nouvel, A. Penarier, J. Torres, L. Varani, G. Ducournau, P. Artillan, S. Bollaert, Y. Roelens, D. Coquillat, D. But, W. Knap, and F. Teppe, "Signal-to-noise ratio in terahertz wireless communication using field-effect-transistors as detectors," presented at the *22nd International Conference on Noise and Fluctuations (ICNF 2013)*, Montpellier, France, 2013. DOI: 10.1109/icnf.2013.6578992
- [117] S. i. Hayashi, K. Nawata, H. Sakai, T. Taira, H. Minamide, and K. Kawase, "High-power, single-longitudinal-mode terahertz-wave generation pumped by a microchip Nd:YAG laser", *Opt. Express*, vol. 20, pp. 2881-2886, 2012.
- [118] O. P. Tkalich, A. A. Diatlov, R. A. Mamaev, D. Y. Nechay, "Apply eye patterns for research of digital signals", ISSN1990-5548, vol. 2, pp. 32-41, 2009  
О. Ткалич, А. Дятлов, Р. Мамаев, and Д. Нечай, "Применение глазковых диаграмм для исследования цифровых сигналов," *Електроніка та системи управління*, vol. 2, pp. 32-41, 2009.

## PUBLICATIONS OF THE AUTHOR

### *Journal Article*

- D. B. But**, C. Drexler, M. V. Sakhno, N. Dyakonova, O. Drachenko, F. F. Sizov, A. Gutin, S. D. Ganichev, and W. Knap, "Nonlinear photoresponse of field effect transistors terahertz detectors at high irradiation intensities," *Journal of Applied Physics*, vol. 115(6), pp. 164514 (2014), DOI: 10.1063/1.4872031
- D. But**, O. Golenkov, N. Sakhno, F. Sizov, S. Korinets, J. Gumenjuk-Sichevska, V. Reva, S. Bunchuk, *Silicon field-effect transistors as radiation detectors for the Sub-THz range*, *Semiconductors* 46(5), pp. 678-683 (2012), DOI: 10.1134/s1063782612050107
- D. But**, N. Dyakonova, D. Coquillat, F. Teppe, W. Knap, T. Watanabe, Y. Tanimoto, S. Boubanga Tombet and T. Otsuji, *THz Double-Grating Gate Transistor Detectors in High Magnetic Fields*. *Acta Physica Polonica A* 122, pp. 1080-1082 (2012)
- O.A. Klimenko, W. Knap, B. Iniguez, D. Coquillat, Y.A. Mityagin, F. Teppe, N. Dyakonova, H. Videlier, **D. But**, F. Lime, J. Marczewski, K. Kucharski, *Temperature enhancement of terahertz responsivity of plasma field effect transistors*, *Journal of Applied Physics* 112(1), pp. 014506-014505 (2012), DOI: 10.1063/1.4733465
- F. Sizov, A. Golenkov, **D. But**, M. Sakhno, V. Reva, *Sub-THz radiation room temperature sensitivity of long-channel silicon field effect transistors*, *Opto-Electronics Review* 20, pp. 194-199 (2012)

### *Conference Proceedings*

- D. B. But**, N. Dyakonova, C. Drexler, O. Drachenko, K. Romanov, O. G. Golenkov, F. F. Sizov, A. Gutin, M. S. Shur, S. D. Ganichev, and W. Knap, "The dynamic range of THz broadband FET detectors " in *SPIE Optical Engineering + Applications*., San Diego, United States, pp. 884612-884612-7 (2013), DOI: 10.1117/12.2024226
- W. Knap, N. V. Dyakonova, F. Schuster, D. Coquillat, F. Teppe, B. Giffard, **D. B. But**, O. G. Golenkov, F. F. Sizov, et al., *Terahertz detection and emission by field-effect transistors*. *Proc. SPIE* 8496 (2012), DOI: 10.1117/12.930091
- W. Knap, F. Schuster, D. Coquillat, F. Teppe, B. Giffard, **D.B. But**, O.G. Golenkov, F.F. Sizov, *Terahertz Detectors Based on Silicon Technology Field Effect Transistors*, *MRS Proceedings* 1437 (2012), DOI: 10.1557/opl.2012.1187
- F.F. Sizov, O.G. Golenkov, V.P. Reva, **D.B. But**, *Electrical parameters of Si n-MOSFET THz-detector: matching with external amplifier*, *Vestnik Novosibirsk State University. Series: Physic* , pp. 68-71 (2010)

*Book Chapters*

- W. Knap, D. Coquillat, N. Dyakonova, **D. But**, T. Otsuji and F. Teppe, “Terahertz Plasma Field Effect Transistors” in Springer Series in Optical Sciences: *Physics and Applications of Terahertz Radiation*, edited by M. Perenzoni and D. J. Paul, (Springer, Dordrecht, Netherlands, 2014), pp. 77 - 102, DOI: 10.1007/978-94-007-3837-9
- W. Knap, **D. B. But**, N. Dyakonova, D. Coquillat, A. Gutin, O. Klimenko, S. Blin, F. Teppe, M.S. Shur, T. Nagatsuma, S.D. Ganichev, and T. Otsuji, “*Recent Results on Broadband Nanotransistor Based THz Detectors*” in NATO Science for Peace and Security Series B, Physics and Biophysics: *THz and Security Applications*, edited by C. Corsi, F. Sizov, (Springer, Dordrecht, Netherlands, 2014) pp.189 – 210, DOI: 10.1007/978-94-017-8828-1